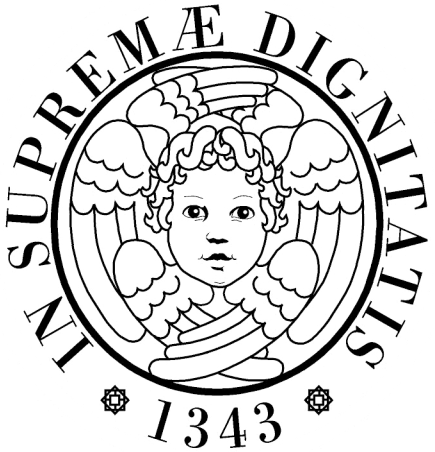

Università di Pisa

Corso di Laurea Magistrale in Ingegneria Energetica

Aerodynamic Performance of a Periodically Oscillating Vertical Axis Wind Turbine

Tesi di Laurea Magistrale

Relatori:
Stefania Zanforlin
Takafumi Nishino
Maurizio Collu

Candidato:
Edoardo Cicirello

Anno Accademico 2015/2016

Abstract

To ensure successful modeling of a floating wind turbine, its aerodynamic behaviour has to be investigated. At the time of writing, the only relevant studies on the topic are about vertical axis wind turbines (VAWTs) in skewed flow. There is lack of experimental, numerical or theorical studies about floating turbines.

In the following thesis, the aerodynamic performance of a periodically oscillating VAWT is investigated through computational and theorical means. The complex dynamics of a floating turbine was simplified to a sinusoidal pitch motion, assuring simplicity without losing meaningfullness.

A theory is given to predict the aerodynamic torque of an oscillating VAWT, obtaining it from the one of the same fixed axis turbine. A blade-element model was developed to achieve this result, taking into account the effect of oscillation on key parameters affecting the torque, that is angles of attack and relative wind speed. The core idea of the method, is to use blade element theory not as a prediction itself, but as a mean to correct the aerodynamic torque of the fixed axis turbine. The latter may be the result of both experiments, or numerical simulations.

Theorical predictions were compared against data from CFD URANS simulations, for two different oscillation frequencies. These were chosen in the typical range of wave energy spectrum, in order to test representative conditions for floating applications. CFD simulations were also performed to obtain the torque of the fixed axis turbine, which was validated against experimental data from the 17m Darrieus-type rotor studied by SANDIA laboratories.

Numerical simulations showed aerodynamic forces are deeply affected by oscillation. As intuition suggests, torque increases when the turbine pitches in the opposite

direction of the wind, and decreases when it pitches in the same direction. This periodic oscillation causes significant ripple and maximum torque increase. For the higher oscillation frequency, which represents the most extreme condition, maximum torque was more than 2 times the one of the fixed turbine. Mean torque was found to be almost unaffected or slightly increased. For the higher oscillation frequency a 4.4% increase was observed.

The theorical model was able to reproduce the behaviour of the oscillating turbine with satisfactory accuracy. To quantify the matching, absolute error was divided by the peak torque of the fixed axis turbine. For the lower oscillation frequency worst accuracy is 13.8%, while mean accuracy is 5.3%. As the frequency grows the hypothesis which the model is based on become less valid, so for the higher oscillation frequency precision decreases, in fact worst accuracy is 29.0% while mean is 9.1%.

The theory proved to attain reasonably accurate results notwithstanding its simplicity, making it a cost-effective tool for quick analysis or optimization. Moreover, the theory could insight the way in which oscillation affects the torque. Considering relative wind speed separately showed that it has little influence, so it can be concluded that torque is affected by oscillation mainly by the change in the angles of attack. By comparing theorical and computational results, it was possible to show the dynamic effect on the downwind blade created by the wake of the upwind passage, a phenomenon which momentum models tailored for floating turbines should take into account. Finally some conclusions are drawn on the advantages and disadvantages of the aerodynamic features of Darrieus type VAWTs.

Contents

Introduction **10**

1 Offshore wind energy **12**

1.1 Present and future diffusion 12

1.2 The limits of fixed foundation technology 14

1.3 State of the art of floating offshore wind 15

1.3.1 Foundations 15

1.3.2 Technology readiness 16

1.4 VAWT versus HAWT for floating applications 18

1.5 Technical challenges 19

2 VAWT aerodynamics **21**

2.1 Flow description 21

2.1.1 Dynamic stall 22

2.2 BEM models 24

2.3 CFD simulations 25

3 Computational model setting **27**

3.1 SANDIA turbine 27

3.2 Domain 28

3.3 Turbine geometry 30

3.4 Sliding interface 30

3.5 Mesh 32

3.5.1 y_+ estimation . . . 33
3.5.2 Mesh characteristics . . . 34
3.5.3 Mesh quality . . . 36
3.6 Simulation settings . . . 36
3.6.1 Turbulence model . . . 36
3.6.2 Boundary conditions . . . 37
3.6.3 Numerical methods . . . 37
3.6.4 Convergence criteria . . . 38
3.6.5 Time step . . . 39

4 Fixed axis turbine validation 40
4.1 Experimental data . . . 40
4.1.1 Accuracy . . . 40
4.1.2 Operating conditions . . . 42
4.2 CFD simulations . . . 44
4.2.1 Uniform wind profile . . . 44
4.2.2 Power law wind profile . . . 44
4.3 Validation . . . 46

5 Periodically oscillating turbine analysis 50
5.1 Dynamics of a floating VAWT . . . 50
5.2 Law of motion . . . 52
5.3 Dynamic mesh . . . 53
5.3.1 Discretization errors . . . 55
5.4 Sensitivity analysis on the timestep . . . 56
5.5 Results . . . 58
5.6 Mean torque convergence . . . 61

6 Theorical analysis 63
6.1 General idea . . . 63
6.2 Aerodynamical torque model . . . 64

6.3 Relative wind speed and angle of attack 66
6.4 Relative wind speed correction 70
6.5 Angle of attack correction 71
6.6 Combined correction 72
6.7 Freestream velocity correction 73
6.8 Multiple sections correction 75
6.9 Comparison against CFD data 76
6.10 Discussion 79

7 Conclusions **82**
7.1 Overview 82
7.2 Computational analysis 82
7.3 Theorical analysis 83
7.4 The Darrieus turbine for floating applications 84
7.5 Suggestions for future work 84

A FLUENT UDFs code **85**

B Relative wind speed **87**

C Multiple sections correction **91**

Bibliography **93**

List of Figures

1-1 Annual and cumulative offshore wind capacity, EWEA 2016 [1]. . . . 13
1-2 Water depths around Europe. 13
1-3 Average water depth and distance to shore of online, under construction and consented wind farms, EWEA [21]. 14
1-4 LCOE versus water depth for various foundation designs. 15
1-5 Floating wind foundation typologies (DNV-GL, 2014). 16
1-6 TRL definitions and milestones. 17
1-7 2014 floating offshore wind projects divided by TRL. 17
1-8 The aerogenerator X, an example of new VAWT design for floating applications. 19

2-1 Typical dynamic stall behaviour of a NACA 0012 airfoil at Mach=0.3 (Leishman [26]). 22
2-2 A flow visualization of dynamic stall. 23
2-3 Schematics of a DMST model (Keinan [25]). 24
2-4 Keinan (left) and Wakui (right) DMST model. 25
2-5 Contours of velocity, an example of the present CFD analysis on a floating VAWT. 26

3-1 SANDIA 17m Darrieus type wind turbine (Johnston, 1982). 28
3-2 Size of the domain; the red sphere represents the location and size of the turbine. 29
3-3 Turbine geometry for the CFD simulation. 29
3-4 A comparison between the rounded profile and the original one. . . . 30

3-5 Spherical sliding interface. 31
3-6 A view of the mesh around the blade. 34
3-7 Mesh and blocking around the rotor. 35
3-8 Mesh and blocking of the outer domain. 35
3-9 Mesh quality evaluation through the "determinant 3x3x3" and "angle" criteria. 36
3-10 Names of the boundaries. 37

4-1 Definition of the rotor position angle θ 41
4-2 Experimental torque vs. rotor position angle. 43
4-3 Torque versus rotor position for all the revolutions performed. 44
4-4 Torque versus rotor position for all the revolutions performed. 45
4-5 Torque comparison between the simulations with uniform and power law wind profile. 46
4-6 Overall torque comparison against experimental and Cranfield University data for TSR=2.02. 47
4-7 Overall torque comparison against experimental and Cranfield University data for TSR=4.6. 48
4-8 Blade torque comparison against Cranfield University data. 48
4-9 Comparison against experimental and Cranfield University data for TSR=2.02. 49

5-1 6 DOFs. 51
5-2 Borg [12] ASDs for the 5MW DeepWind floating VAWT. 52
5-3 Comparison between two different interface motions: left rotation and translation, right translation only. 54
5-4 Discretization error on the position of a point moving of uniform circular motion. 55
5-5 Sensitivity analysis on the timestep for $\omega_o = 0.6\ rad/s$. 57
5-6 Overall torque of the oscillating and fixed turbine. 58
5-7 Blade torque of the fixed and oscillating turbine 59

5-8 Overall torque and oscillation angular velocity for $\omega_o = 0.6\ rad/s$. . . 60
5-9 Torque moving means for $\omega_o = 1.2\ rad/s$ (up) and $\omega_o = 0.6\ rad/s$ (down). 62

6-1 Lift component generating torque. 66
6-2 Reference system for the relative wind velocity. 68
6-3 A comparison between the angle of attack of a fixed and an oscillating turbine. 69
6-4 A comparison between the relative wind speed of a fixed and an oscillating turbine. 70
6-5 The effect of the correction based on the relative wind speed for $\beta_{max} = 10^\circ$ and $\omega = 0.6\ rad/s$. 71
6-6 Torque prediction based on the angle of attack correction for $\beta_{max} = 10^\circ$ and two different oscillation frequencies. 72
6-7 A comparison between the angle of attack and the combined correction for $\beta_{max} = 10^\circ$ and two different oscillation frequency. 73
6-8 Correlation between the predicted torque of the oscillating turbine and the relative freestream speed. 74
6-9 Predicted torque based on the multiple section correction versus the equatorial section one for $\beta_{max} = 10^\circ$ and $\omega = 1.2\ rad/s$. 75
6-10 Comparison between the predicted overall torque and the one obtained from the CFD analysis. 77
6-11 Comparison between the predicted blade torque and the one obtained from the CFD analysis. 78
6-12 The mechanism of energy extraction in a periodically oscillating wind turbine 81

B-1 Freestream velocity decomposition. 88
B-2 Velocity due to oscillation decomposition. 89

List of Tables

3.1 SANDIA turbine geometrical characteristics. 27

3.2 Discretization schemes adopted. 38

3.3 Convergence criteria for every quantity. 38

4.1 Reference values for the two operating conditions. 43

5.1 Coulling [17] data on pitch for a 1/50 scaled model of the 5MW DeepWind turbine. 51

5.2 Working conditions for the aerodynamic simulation. 53

5.3 Maximum and mean torque for fixed and oscillating axis simulations. 60

5.4 The effect of the rotational angular speed roundoff on N and M. . . . 61

6.1 Mean and maximum relative error of the model for the overall torque. 76

Introduction

The energy coming from offshore wind farms has considerably grown in recent years, and more is expected to be gathered in the future. Just in 2015, 3 GW of grid connected capacity were installed reaching a total power of 11 GW, which it will rise up to 66 GW by 2030[1].

The current technology for offshore installations consists in the well known horizontal axis wind turbines with fixed foundations, which are suitable for water depths of no more than 40÷50 m.

Unlocking deeper sea bottoms requires the development of floating wind turbines, which could provide access to high quality wind resources in convenient locations. The technology readiness of floating offshore wind is not enough advanced yet for commercial development [2], as no full scale turbine or array of scaled turbines have been tested.

The major technical challenges are the development of modelling and analysis tools to design specific solutions for this technology, and the optimization of wind turbines specifically for floating support structures.

Modelling tools in particular should be able to perform coupled analyses, joining aerodynamics models, hydrodynamics models for offshore structures, control and electrical system dynamics models, and structural-elastic dynamics models.

This work focuses on establishing a better understanding of the aerodynamic performance of a floating wind turbine, filling a gap in the existing literature. A vertical axis wind turbine (VAWT) was chosen for the study, as it has been shown

[1] [21] European Wind Energy Agency - Wind energy scenario for 2030, 2015.
[2] [23] Carbon Trust - Floating Offshore Wind: Market and Technology Review, 2015.

to possess benefits over horizontal axis wind turbines (HAWTs) in reducing the costs of the floating structure[3], as well as other advantages. The analysis was carried on using two different methodologies, that is CFD and an original blade-element model tailored for floating VAWTs.

The computational model was validated for the fixed turbine against an independent analysis and experimental data, creating the background on which the moving axis simulations were performed. The motion was simplified from 6 degrees of freedom (DOFs) to just pitching, and the aerodynamic torque acting on the blades was tested for two different oscillation frequencies.

The aforementioned theorical model gives a corrective function for the torque of a fixed turbine, which turns it into the torque of an oscillating one. Several corrective functions were tested, taking into account the key parameters which affect the torque according to the blade element theory. The model proved to be a cost effective tool for quick analyses thanks to reasonable accuracy and simplicity.

Both of the methodologies followed could insight the effect of the turbine motion on the aerodynamic torque and conclusions were drawn on using Darrieus type turbines for floating applications.

[3]Borg and Collu [11, 13].

Chapter 1

Offshore wind energy

In this chapter an overview on offshore wind energy is given to show its present and future growth and how floating technology fits into the picture. The role of VAWTs will be explained as well as other technological aspects, such as moorings and anchoring systems.

1.1 Present and future diffusion

There is a rising interest of industry in investing in offshore wind energy, especially in Europe which is a leader in this field. The advantages of going offshore are the increased wind intensity, low landscape impact, components transport which is significantly easier for ships than for trucks or trains and less planning constraints. The main drawbacks are the high construction cost, as the turbines have to withstand rough weather conditions, difficult maintenance and grid connection, and environmental impact issues which inevitably bring the levelised cost of energy (LCOE) higher than for onshore wind (60÷105 €/MWh versus 105÷150 €/MWh[1]).

Notwithstanding this the capacity installed in Europe is growing year after year (figure 1-1), reaching 11 GW of grid connected power in 2015. Right in this year 3 GW were installed, more than doubling what had been done in 2014.

As regards the spatial distribution of offshore wind plants they are concentrated

[1] [4] Ecofys - Subsidies and costs of EU energy, 2014.

in the North (69.4%), Irish (17.6%) and Baltic Sea (12.9%). The most involved

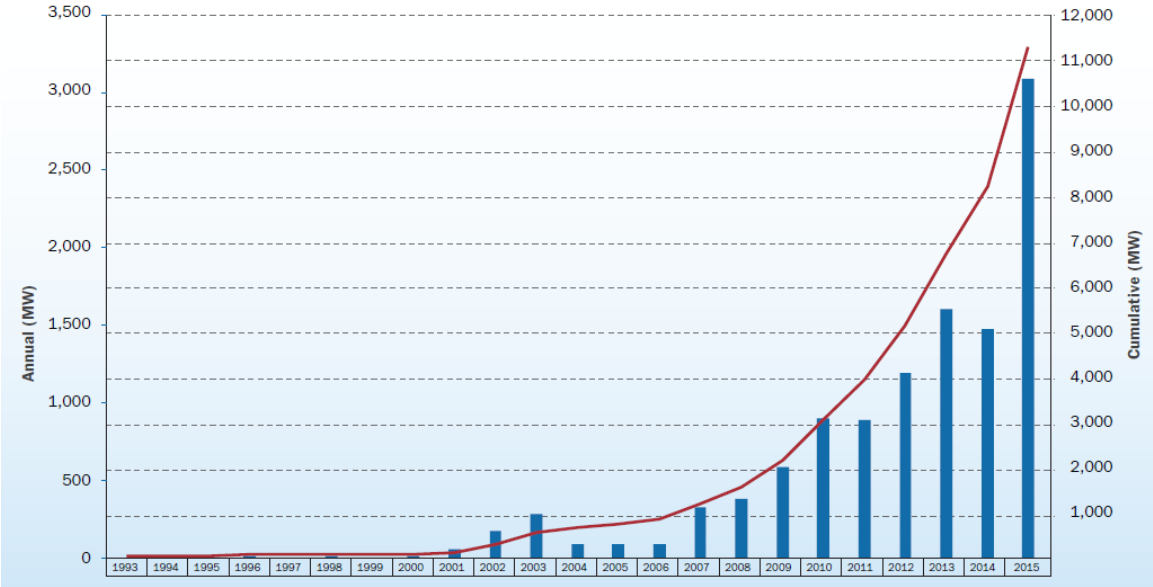

Figure 1-1: Annual and cumulative offshore wind capacity, EWEA 2016 [1].

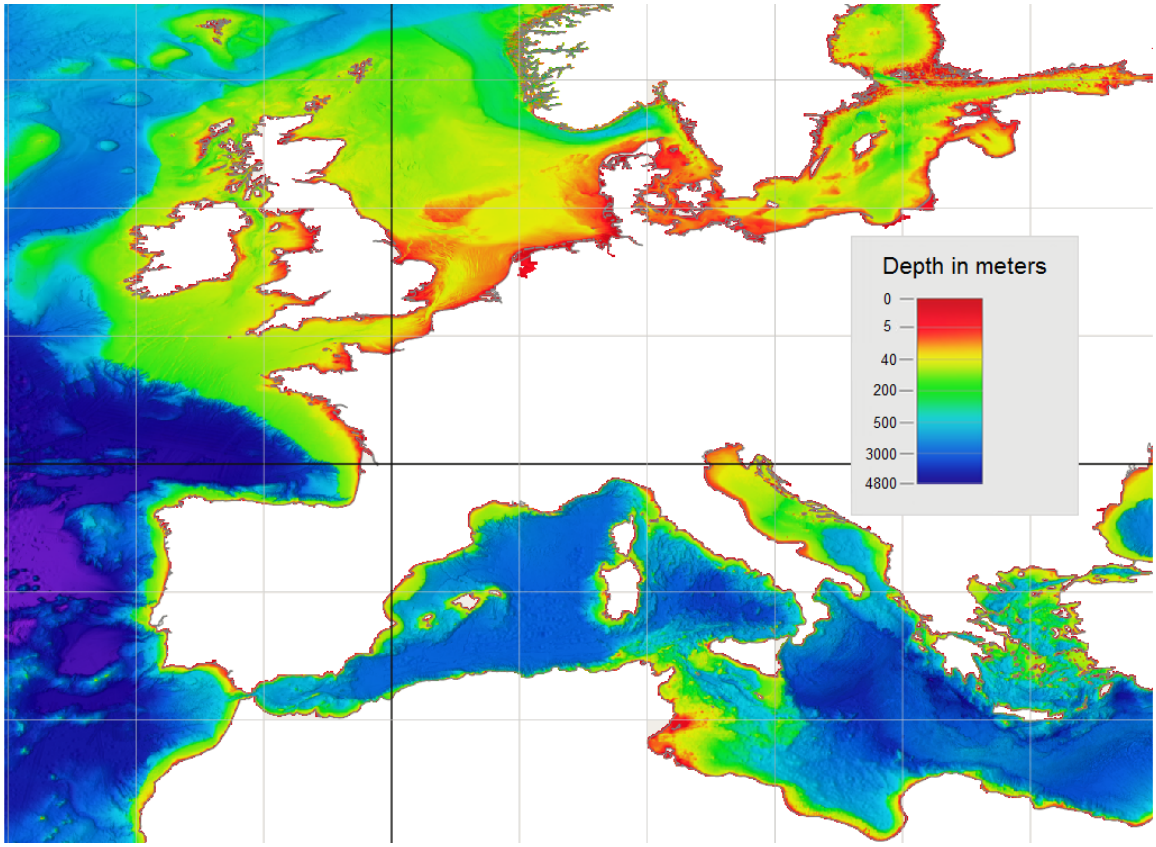

Figure 1-2: Water depths around Europe.

countries in fact all face the aforementioned seas, with UK, Germany and Denmark alone having the 87.3% of the total capacity installed.

For the year 2030 66 GW of offshore wind power are forecasted by EWEA, which will supply 245 TWh of energy covering 7.7% of EU electricity demand.

1.2 The limits of fixed foundation technology

Floating offshore wind is missing from the scenario at the moment because the technology is still not ready for commercial deployment, even though it has the potential to unlock the access to good quality wind resources where water depths exceed 40÷50 m, especially in the Mediterranean Sea and in the Atlantic Ocean (figure 1-2). The

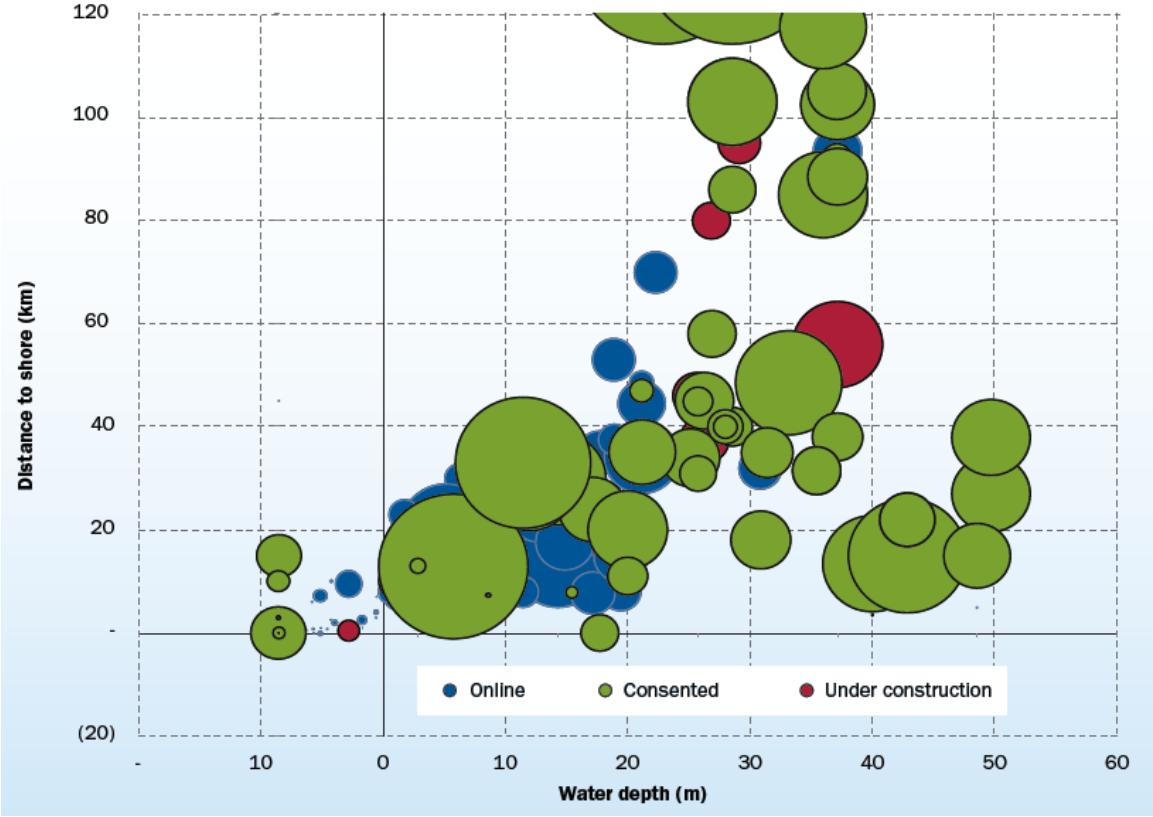

Figure 1-3: Average water depth and distance to shore of online, under construction and consented wind farms, EWEA [21].

map of online, consented and under construction offshore wind farms (figure 1-3) outlines the limits of fixed foundation turbines, confined in water depths shallower than

60 m.

The reason of such a restriction is economical as the LCOE grows rapidly with the water depth [31](figure 1-4), making fixed foundations inconvenient after a certain value.

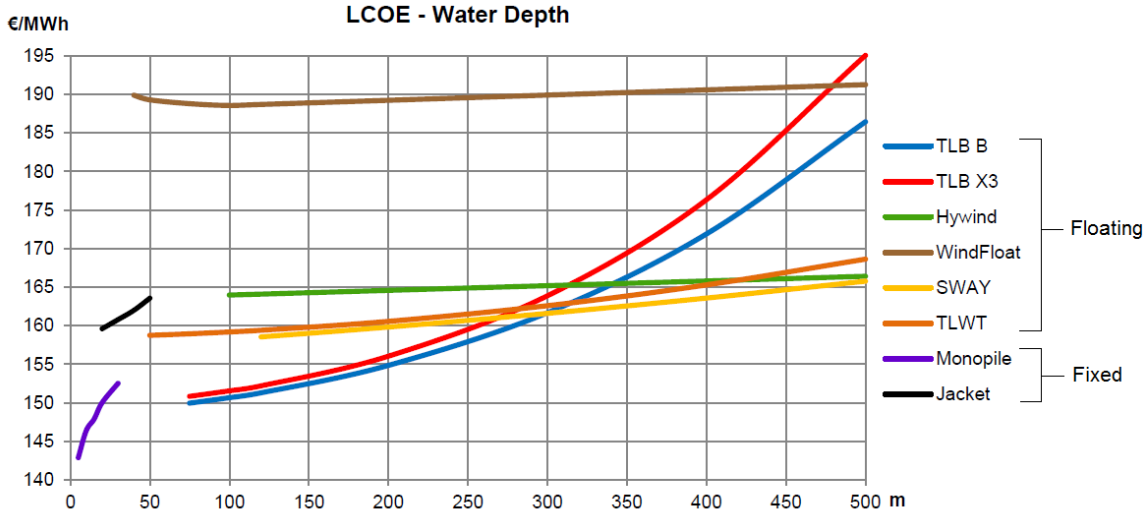

Figure 1-4: LCOE versus water depth for various foundation designs.

1.3 State of the art of floating offshore wind

Floating wind turbine exist as a concept since the early 70s but the first test device was installed only in 2008 off the Italian coast. In the following paragraphs the most common types of foundation will be explored and the readiness of the technology will be assessed on the basis of the existing projects.

1.3.1 Foundations

The dominant types of deep offshore foundations are three (figure 1-5), each of them adapted from the offshore oil and gas industry:

- **Spar-buoy**: A cylindrical buoy stabilizes the structure with the help of a ballast, thank to the fact that the centre of gravity is lower in the water than the

centre of buoyancy. This is achieved by making the upper parts lighter and hollow, while the majority of the weight is concentrated down.

- **Semi-submersible platform**: A buoyancy stabilised platform which floats partially below the sea level whilst anchored to the bottom with catenary mooring lines.

- **Tension leg platform (TLP)**: A semi-submerged buoyant structure like the previous system, this time anchored to the seabed with tensioned mooring lines rather than catenary lines.

Figure 1-5: Floating wind foundation typologies (DNV-GL, 2014).

1.3.2 Technology readiness

Any technology have to go through a series of progresses before being commercially ready and start being deployed, so to evaluate the current state of floating offshore

TRL Level	Milestone
0. Unproven concept	Idea / preliminary study / patent
1. Proven concept	Desk-based basic design assessment / proof of concept
2. Validated concept	Detailed numerical modelling / structural assessment
3. Prototype tested	Scaled testing (e.g. tank testing, <1 MW demonstration)
4. Environment tested	Offshore demonstration with 1-5 MW turbine
5. System tested	Full-scale offshore demonstration/array with >5 MW turbine
6. System installed	Full-scale demonstration/array with >5 MW turbine with >1 year operation
7. Field proven	Commercial project

Figure 1-6: TRL definitions and milestones.

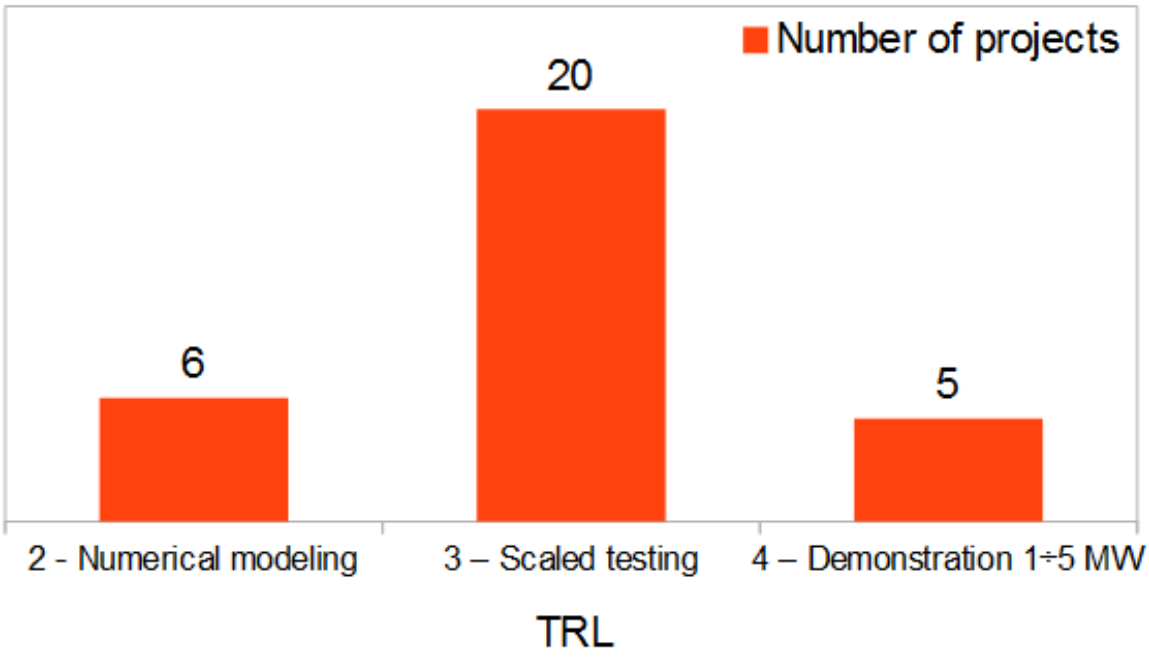

Figure 1-7: 2014 floating offshore wind projects divided by TRL.

wind the Carbon Trust [23] defined seven technology readiness levels (TRLs) (figure 1-6).

Of the existing projects in 2014 25 of them have gone beyond the numerical modelling reaching the 3rd level of scaled prototype testing (figure 1-7). The project which

have undergone the 4th phase, that is an offshore multi megawatt demonstration, are just 5 instead.

1.4 VAWT versus HAWT for floating applications

Of the 31 projects examined by the Carbon Trust [23] the ones including a HAWT outnumber the ones with a VAWT 26 to 5. This is probably due to the long history of these machines which are very well known for onshore applications, and to the possibility of adapting existing designs for new applications like it has been done for the offshore wind sector. The possible disadvantages of HAWTs for floating applications are:

- **High centre of mass**: The drive train and electrical motor as well as other components are placed inside the nacelle.
- **Lower performances in skewed flow**: Because of the aerodynamic thrust on the rotor blades the turbine will be in skewed flow conditions, which mean reduced performances for this kind of turbine, caused by the reduction of the frontal area in the direction of the wind.
- **Advanced yaw control system**: The yaw control system must handle the platform motion, so the existing solutions need to be improved.

On the contrary VAWTs have the following advantages:

- **Low centre of mass**: All the components are located in the platform.
- **Low centre of aerodynamic pressure**: Due to the different location of the aerodynamic trust centre the inclining moment is lower than for HAWTs.
- **Better performances in skew**: H-Darrieus turbines proved to have increased performances in skewed flows (Orlandi [32, 33], Mertens [29]).
- **No yaw control system**: The VAWT works independently from the wind direction.

The first two characteristic mentioned were shown by Borg and Collu [11] to be determinant factors in the higher static stability of a floating VAWT, which means a less costly floating support platform.

1.5 Technical challenges

The technical challenges to face for the development of floating offshore wind can be divided into three areas: modelling and numerical tools, development of optimised turbine designs for floating support structures (figure 1-8) and connection to the grid.

Figure 1-8: The aerogenerator X, an example of new VAWT design for floating applications.

As regards the modelling tools, they should be able to perform coupled analyses, joining aerodynamics models, hydrodynamics models for offshore structures, control and electrical system dynamics models, and structural-elastic dynamics models. Such models are currently being researched and validated, such as NREL's FAST [34] or

FloVAWT [16], but there are still no aerodynamic models to reproduce the behaviour of a floating turbine.

Chapter 2

VAWT aerodynamics

The characteristics of the flow around the blades of VAWTs make it particularly challenging to model, first of all because of its intrinsic unsteadiness which make it really different from HAWTs. In this chapter the working principle and the physical phenomena peculiar of VAWTs will be analysed, as well as a review on blade-element momentum models (BEM models) and CFD possibilities.

2.1 Flow description

As anticipated the flow around the blades of a VAWT is inherently unsteady, as a result of the angle of attack (AoA) varying in a revolution approximately in a sinusoidal way. Considering the relative velocity of the wind as a composition of the freestream and rotational velocity it is possible to obtain a theorical behaviour of the AoA with the azimuthal angle:

$$\tan\alpha \;=\; \frac{\sin\theta}{\cos\theta+\lambda}\,, \tag{2.1}$$

where $\lambda = \omega R/U_\infty$, called tip-speed ratio (TSR), is the ratio between the rotational speed of the blade and the freestream speed. This range in which the AoA oscillates increases as the TSR gets smaller, until the critical condition of stall is reached for some azimuthal position. The dynamic stall though is a completely different phe-

nomenon from static stall and the following paragraph is dedicated to its description. Its understanding is fundamental for the performances of a VAWT.

Another unique characteristic of VAWTs is the strong difference between the upwind and downwind part of the rotor. The wake and vortexes shed upwind in fact are transported downstream, where they interact again with a blade influencing it.

To conclude it is worth mentioning the curvature effects which the blades undergo as a result of the curvilinear flow they experience. Migliore [30] showed that the performances of Darrieus turbines are significantly affected especially for blades of large chord, and more recently Bianchini [10] developed a model to account for the virtual camber effect.

2.1.1 Dynamic stall

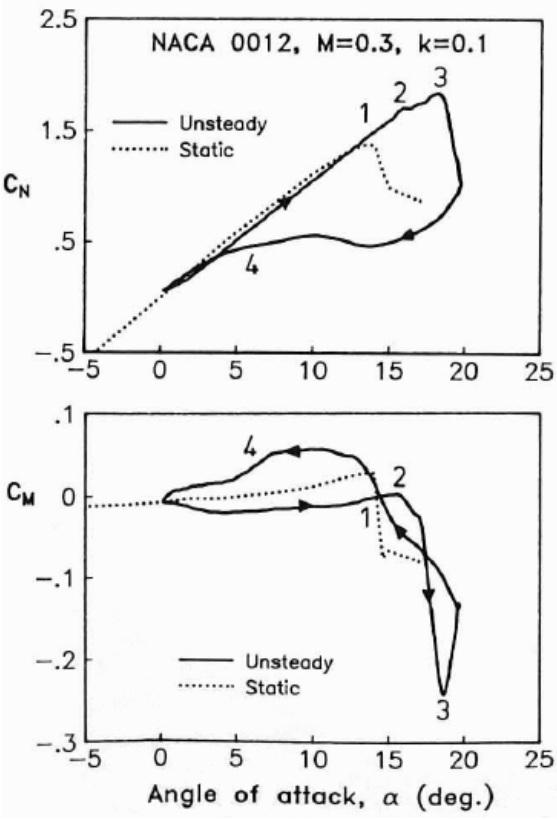

	FLOW STRUCTURE
1	FLOW REVERSALS WITHIN BOUNDARY LAYER, FORMATION OF VORTEX
2	VORTEX DETACHES AND MOVES OVER AIRFOIL SURFACE
3	VORTEX PASSES TRAILING EDGE, FULL STALL DEVELOPS
4	REATTACHMENT OF FLOW

	FORCES AND MOMENTS
1	EXCEEDS STATIC MAXIMUM LIFT, EXTRAPOLATE LINEAR RANGE
2	PITCHING MOMENT DIVERGENCE, VORTEX LIFT PRESENT
3	MAXIMUM LIFT, RAPID DECAY, MINIMUM PITCHING MOMENT, MAXIMUM DRAG
4	READJUST TO LINEAR RANGE

Figure 2-1: Typical dynamic stall behaviour of a NACA 0012 airfoil at Mach=0.3 (Leishman [26]).

A thorough qualitative description of the phenomenon was given by Beddoes [8] and McCroskey [28], who did experimental studies on cyclically pitching airfoils. The phases outlined are four:

1. The static stall angle of attack is exceeded but the flow is still attached on the majority of the airfoil, with the exception of some reversals within the boundary layer close to the trailing edge. No gross changes in the flow are observed and the aerodynamic forces appear as an extrapolation of the attached flow conditions.

2. A concentrated vortex develops from the leading edge and moves over the airfoil surface. The suction created by the vortex creates lift which is increased further over the static limit, and a strong rise of the pitching moment is observed.

3. As the vortex passes the trailing edge full stall develops. Lift decays rapidly as well as the lift induced pitching moment.

4. If the angle of attack decreases beyond the static stall value the flow reattaches gradually starting from the leading edge.

Figure 2-2 helps visualizing phases 1 to 3.

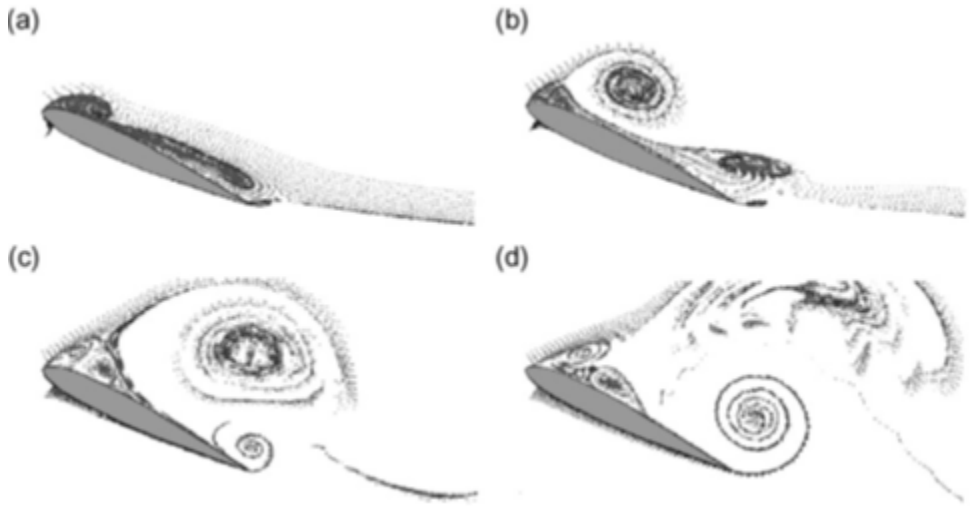

Figure 2-2: A flow visualization of dynamic stall.

2.2 BEM models

In all BEM models the flow velocity across the rotor is calculated by equating the streamwise aerodynamic force on the blade, calculated using the aerodynamical force coefficients, with the momentum rate of change of the air:

$$F_a \;=\; C_a \frac{1}{2} \rho c s W^2 \;= \dot{m} \Delta V \tag{2.2}$$

In double-multiple streamtube (DMST) models the blade inflow velocity is calculated for a set of azimuthal positions both upwind and downwind, making possible to account for the shading effect which the downwind part undergoes and to consider the differences between the leeward and the windward sides (figure 2-3).

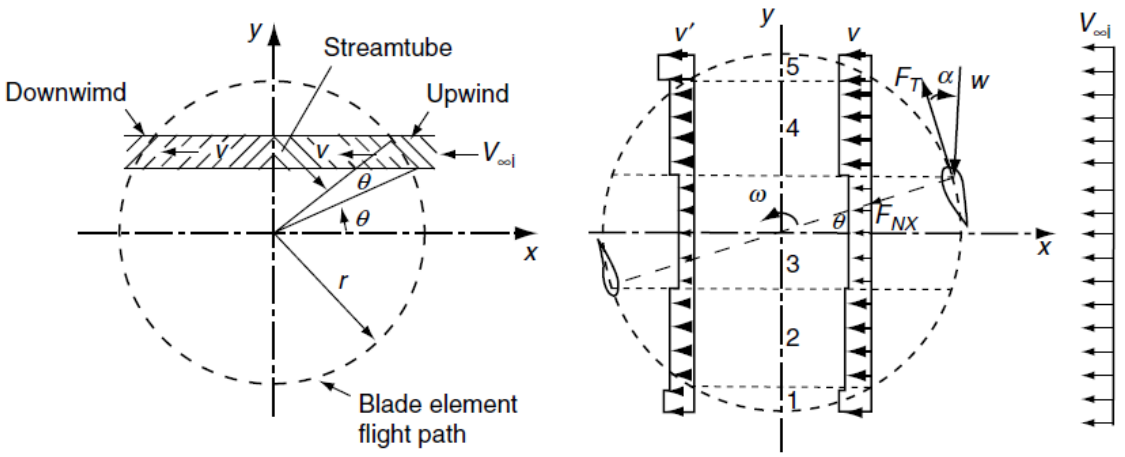

Figure 2-3: Schematics of a DMST model (Keinan [25]).

The model is attractive as it allows the prediction of the instant torque and power of a VAWT with a very low computational cost compared to CFD simulations. There have been continuous updates trying to improve its accuracy, every time taking into account more determining factors, such as tip losses. Keinan [25] for example considered both the streamwise and perpendicular component in the momentum equation (figure 2-4), and Wakui [35] created a similar model for skewed flows. Still on skewed flows Bianchini [9] developed another interesting model, but there are still no models tailored for floating applications.

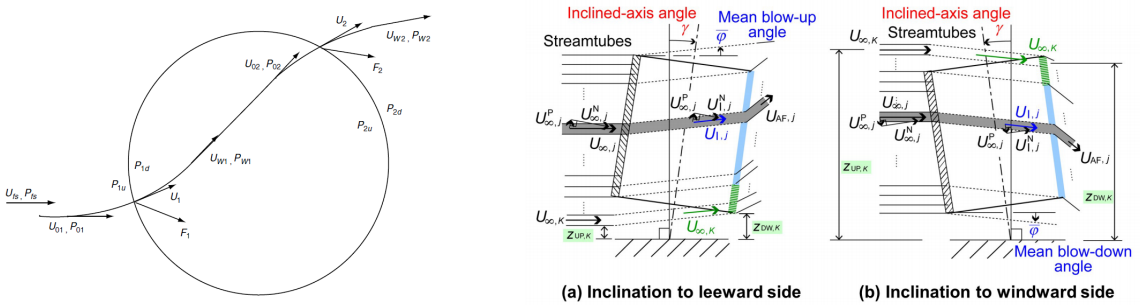

Figure 2-4: Keinan (left) and Wakui (right) DMST model.

2.3 CFD simulations

CFD simulations rely on the numerical solution of the Navier-Stokes equation in a spatially and temporally discretized domain. Their accuracy depends on the spatial and temporal resolution, on the turbulence model and boundary conditions validity. Because of the complexity of such models and the many parameter which need tuning it is fundamental to perform sensitivity analyses and to compare the results of these models against experiments or other independent simulations in similar conditions. The challenges faced when simulating a VAWT are many:

- The simulation is necessarily unsteady.
- It is not possible to take advantage of flow symmetries.
- The big amount of shed vorticity make the computational model sensible to numerical diffusivity.
- All the rotor area has to be resolved accurately, as the vortexes and wake shed in the upwind half interact with the downwind blade

Ferreira [20] investigated the possibilities of numerical methods in predicting dynamic stall in VAWTsm comparing URANS, LES and DES 2D simulations with particle image velocimetry (PIV) data. He concludes that while DES and LES allow a good representation of the vortex shedding and convection URANS models proved insufficient, with significant errors in the forces acting on the downwind passage of

the blade. Orlandi [32, 32] URANS simulations at low TSR, at which dynamic stall occurs, confirm the limits of this kind of analysis.

As regards the sensitivity of the simulation to the free parameters mentioned before, useful information was given by Balduzzi [7], Daróczy [18] and Maître [27].

Talking about the application of CFD simulations, it is worth mentioning Orlandi [32,33] who studied a Darrieus turbine in skew and Vernola [38], who for the first time investigated a periodically oscillating VAWT. This work tries to go further analysing the effect of the oscillation frequency both numerically (figure 2-5) and through an original theorical approach.

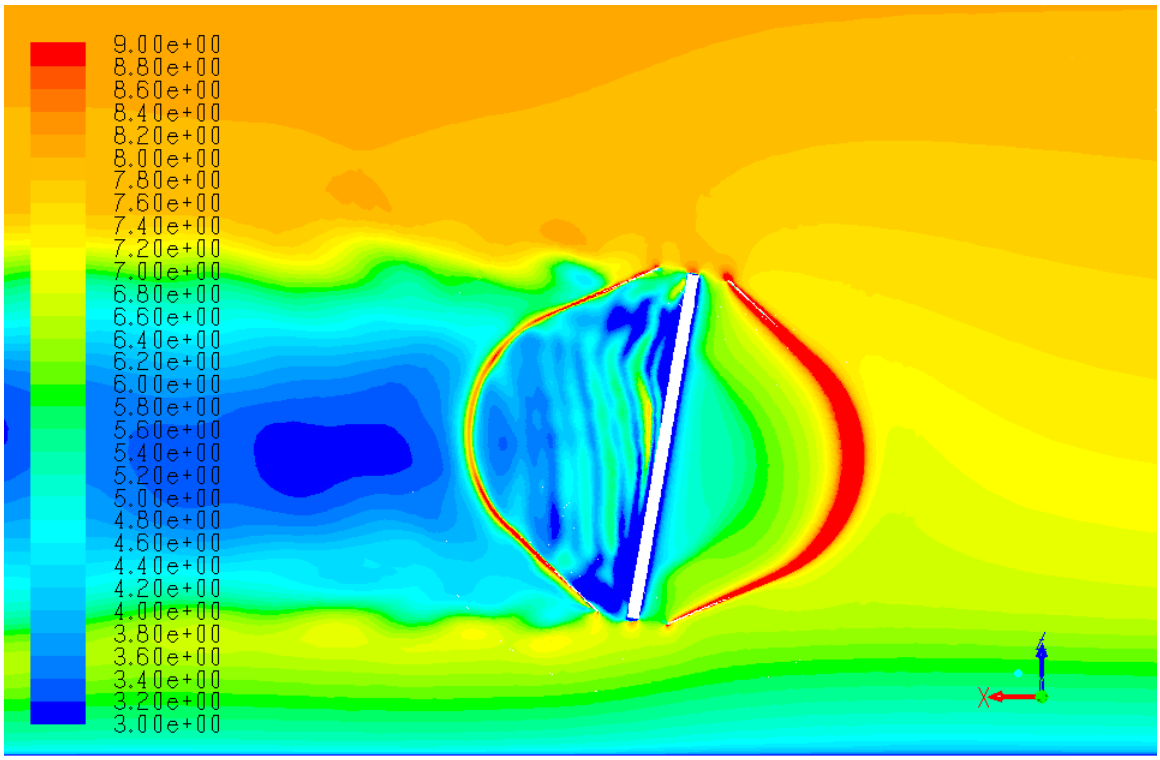

Figure 2-5: Contours of velocity, an example of the present CFD analysis on a floating VAWT.

Chapter 3

Computational model setting

This chapter will go through all the steps followed to build the computational model. In particular, the criteria followed to create the mesh are explained thoroughly, and its quality is reported through the most common evaluation parameters.

3.1 SANDIA turbine

The 17m SANDIA turbine (figure 3-1) was chosen for the detailed reports of its operation in open field and for the characteristic Reynolds of about 10^6, higher than the typical one of wind tunnel tests.

The shape of the blades approximates the Troposkien configuration trough a central part which is a circular arc and straight extremities. The other relevant geometrical specifications are summarized in table 3.1.

Diameter	16.7 m
Height	17 m
Swept area	187 m^2
Ground clearance	4.88 m
Number of blades	2
Airfoil section	NACA-0015
Chord	0.61 m

Table 3.1: SANDIA turbine geometrical characteristics.

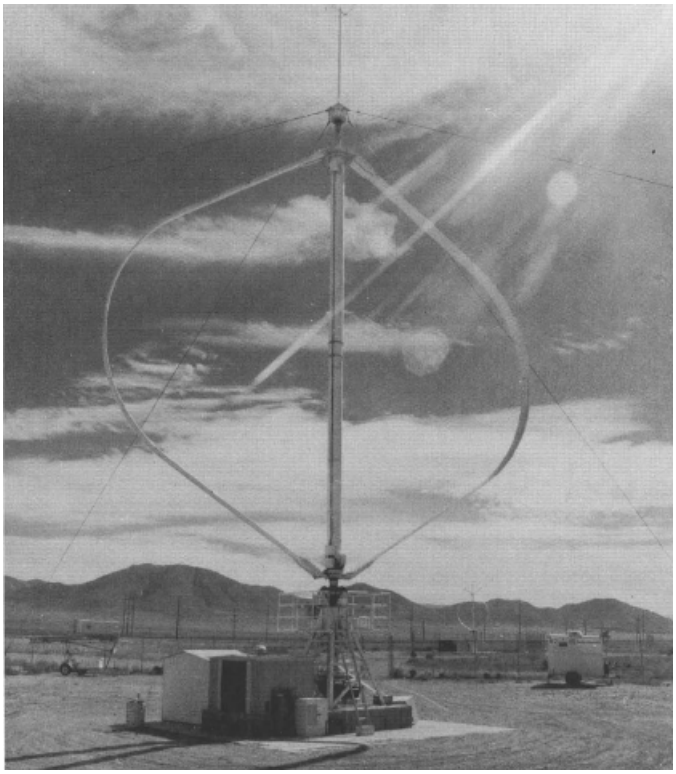

Figure 3-1: SANDIA 17m Darrieus type wind turbine (Johnston, 1982).

3.2 Domain

Once the goal of a CFD simulation is clear, the following step is to define the domain, that is to confine the analysis to a limited, significative, portion of space. For wind turbines the domain is theorically an open space, an infinite extension of air spreading from the turbine in every direction in order to avoid any boundary interference. This is clearly unacceptable for every engineer with no unlimited computational time, so the view has to be narrowed.

The optimal size of the domain is the result of a tradeoff between time saving and accuracy: not too big to reduce the number of cells, not too small to avoid boundary effects. In this study accuracy was privileged, so comparing to the previous study of Orlandi [32, 33] on the same turbine of this work and the review in Balduzzi [7], a domain 60Dx60Dx11D was chosen (figure 3-2).

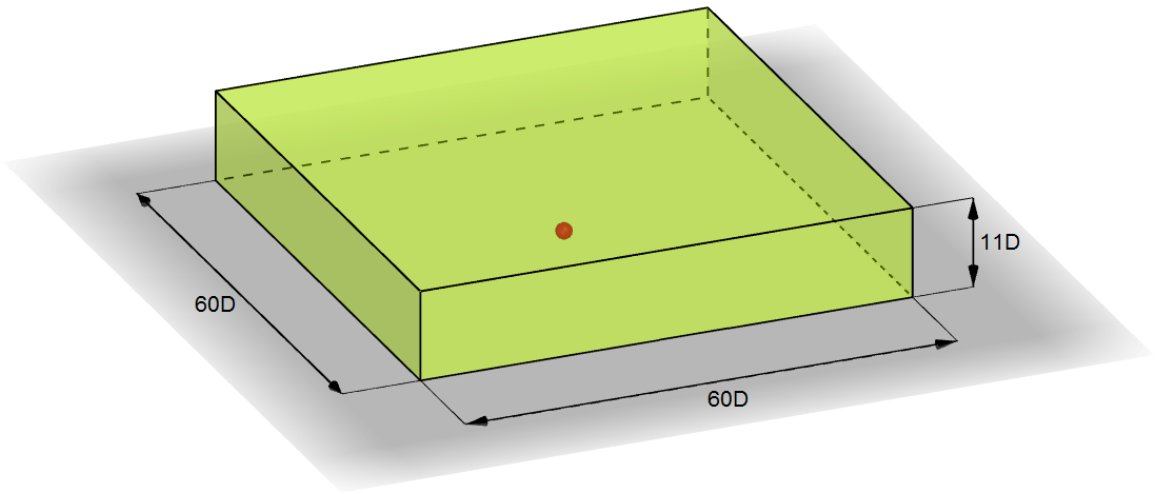

Figure 3-2: Size of the domain; the red sphere represents the location and size of the turbine.

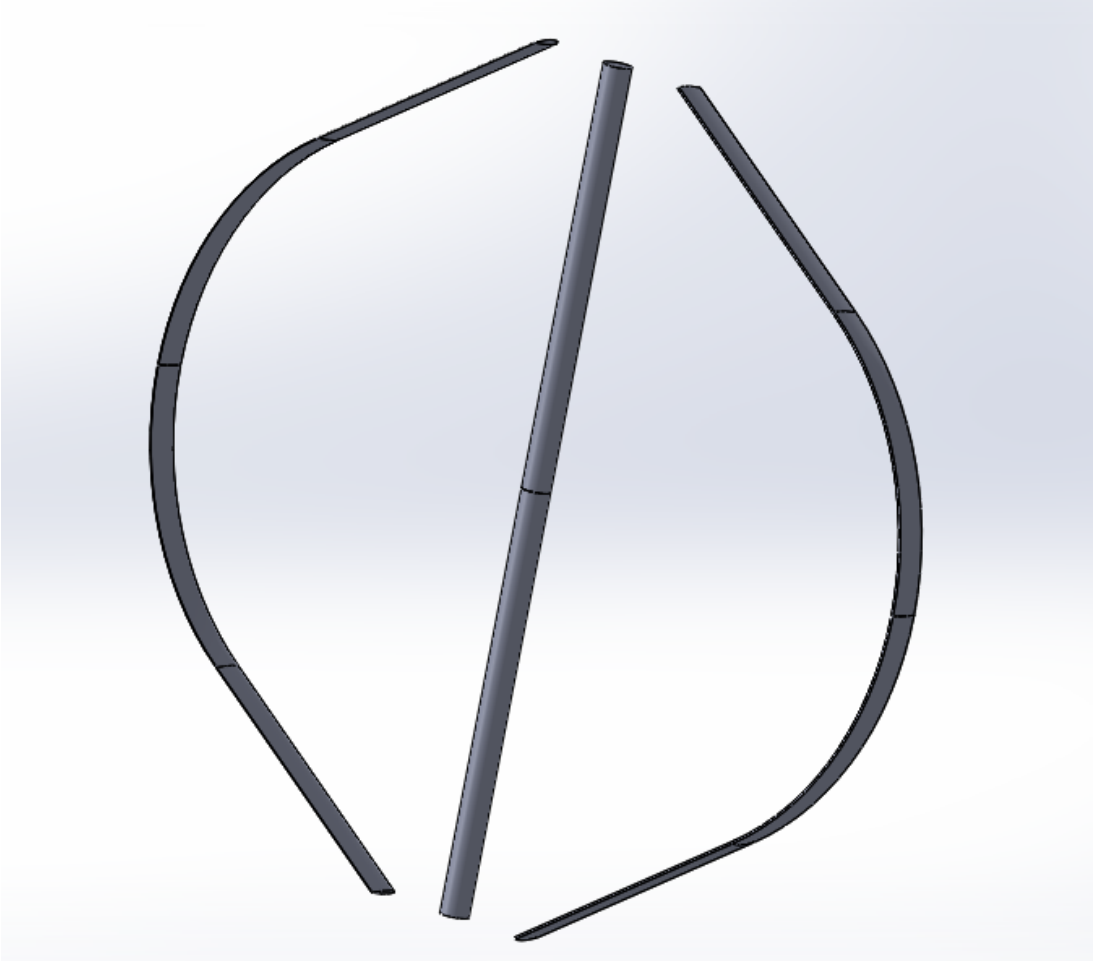

Figure 3-3: Turbine geometry for the CFD simulation.

3.3 Turbine geometry

When modelling the shape of the fluid region the geometry of the real objects involved does not have to be faithfully represented. Some details which do not affect the flow deeply, or that in general do not introduce significative errors may be ignored, especially if this can lead to some sort simplification.

This is the case of this study, in which the last 1 meter of the turbine was cut both from the top and the bottom (figure 3-3), in order to make the blocking for the mesh easier to be done. The portions of blade deleted have a small radius and a low local TSR, so the overall aerodynamic torque will be just lightly influenced.

Also the trailing edge of the blade was modified, rounding it to simplify the blocking again. Only 3.6% of the chord length was changed, so the difference with a proper NACA 0015 profile is minimal.

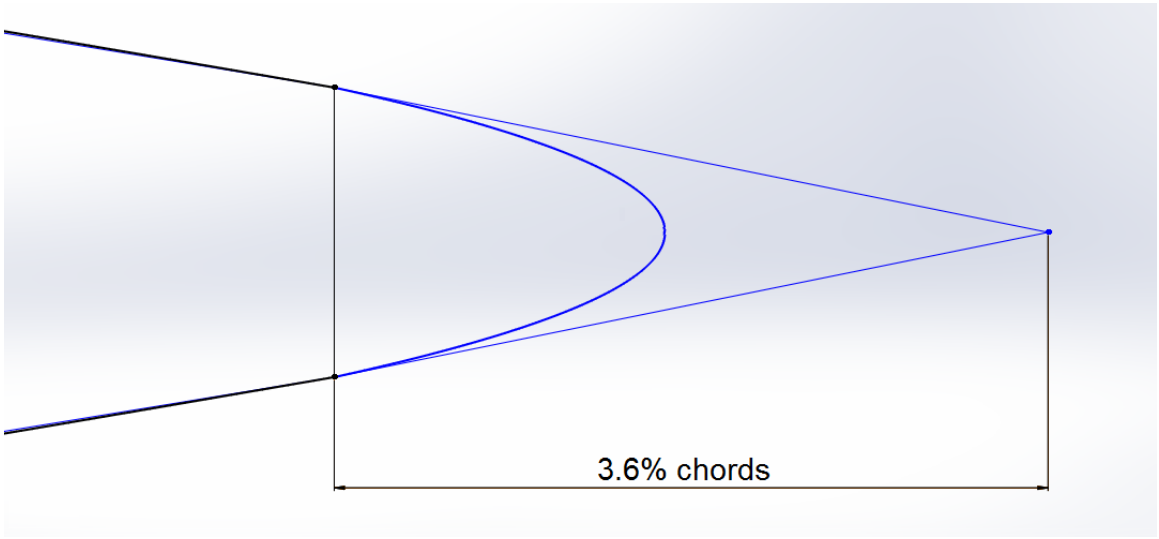

Figure 3-4: A comparison between the rounded profile and the original one.

3.4 Sliding interface

When dealing with rotating parts the sliding mesh is one of the possible approaches. It involves one region of the mesh to stand still and undeformed, while the other containing the rotating parts moves rigidly. The surface where the two regions slide

is called interface. The sliding mesh approach is not enough for the complex motion of an oscillating wind turbine though, so a dynamic mesh has to be considered, that is simply a mesh that can change shape or be remeshed over time.

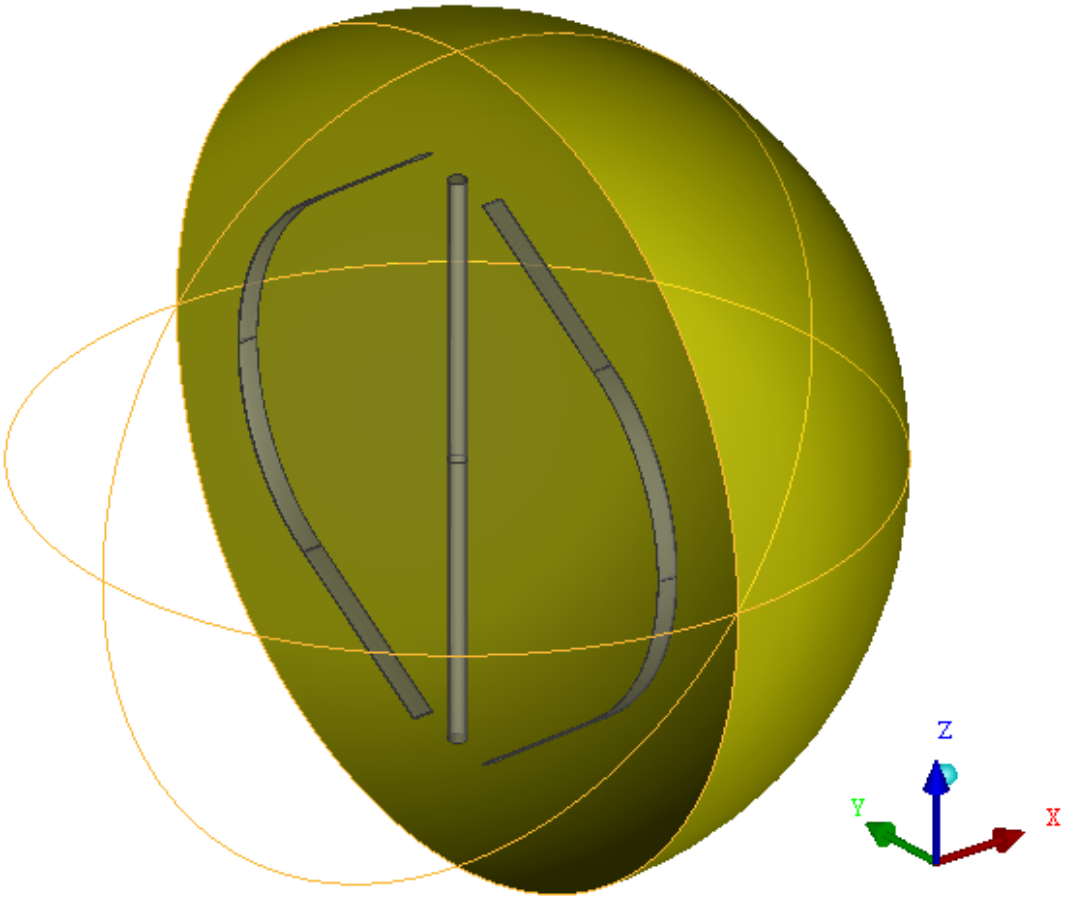

Figure 3-5: Spherical sliding interface.

Considering this the mesh was split in two volumes, one bounding the rotor and moving as a rigid body, both rotating and oscillating, and one other filling the rest of the domain, which literally deforms absorbing the motion of the of the rotor mesh. Being the turbine close to the sea surface, the shape of the rotor mesh has to be chosen carefully in order to avoid contact between them when the turbine is pitching. A sphere of 1.31D (figure 3-5) was chosen exactly for this reason, having also another really important feature. Due to numerical errors in the rigid body motion representation the rotor mesh will experience unexpected trajectories, which may cause the simulation to fail because of elements intersection around the sliding interface.

Proper settings and a spherical interface help solving the problem, as will be explained thoroughly in paragraph 5.3.1.

3.5 Mesh

A good mesh is the one that provides accurate results with a low computational cost. The two goals ask for a lot and a few cells at the same time, so again the CFD engineer has to face a compromise when choosing the number of cells the mesh will be made of. Given a rough estimate of this amount, his or her task will be placing those cells efficiently by the means of an effective blocking strategy.
The zones which require special care are:

- Blades: definitely the flow nearby the blades needs to be simulated with the greatest accuracy. First of all because this analysis is focused on obtaining the aerodynamic torque, which is strongly dependent on how the flow behaves in this region. Secondly, the flow experiences the strongest gradients exactly around the blade, both orthogonally and parallel to the walls.

- Sliding interface: as a rule of thumb, the ratio of faces touching each other from two opposite sides should not exceed 1:4. In other words, to avoid numerical errors the face of a cell should be in contact with no more than 4 other cells. Also, the same length orthogonal to the interface is desired, so the dimension of the cells over the interface should be as uniform as possible. For the present study it is vital that this condition is met, as the interface is particularly close to the rotor.

- Tower: the influence of the tower over the flow and aerodynamic torque is not crucial, but it still important to catch its major features, that are wake and vortex shedding.

- Rotor: especially at low tip-speed-ratios blades generate vortexes when they stall, which are then convected downstream and interact with the blade again.

In general the wake of the blade passing upwind is transported by the wind and interacts with the blade passing downwind, so it is important for all the rotor to have a high mesh density.

- Wake: the purpose of this study is not to represent carefully the wake of the turbine, though a higher mesh density in this region is desirable.

3.5.1 y_+ estimation

Particular attention has to be paid to the height of the first cell along the blade, as it has a great influence on how both boundary layer and aerodynamic forces are simulated. The criterion to choose it is based on the dimensionless wall distance

$$y_+ = y\frac{U_*}{\nu}\,,$$

where y is the distance from the nearest wall, U_* is the friction velocity and ν is the kinematic viscosity. The friction velocity can be defined as

$$U_* = \sqrt{\frac{\tau_w}{\rho}}\,,$$

where τ_w is the wall shear stress and ρ the density.

For near wall modelling with no wall functions a $y_+ < 1$ for the first cell is required (Maitre et al. [27]), so an estimate for this quantity has to be performed. It is possible to do it knowing the Reynolds number and the thickness of the boundary layer through the formula

$$y_+ \sim y_1\sqrt{\frac{Re}{c\ \delta}}\,,$$

where y_1 is the height of the first cell, Re is the Reynolds number, δ is the boundary layer thickness and c is the chord of the blade.
For a flat plate the order of magnitude of a turbulent boundary layer thickness is

$$\delta \sim \frac{c}{Re^{0.2}}\,,$$

so from the two previous equations we finally get

$$y_+ \sim \frac{y_1}{c} Re^{0.7} .$$

Introducing $y_1 = 2.5 \cdot 10^{-6}\ m$, $Re = 1.44 \cdot 10^6$ based on the chord and on the maximum relative wind speed, $c = 0.61\ m$, we obtain a y_+ of $0.84 < 1$, so the first cell height chosen is likely to satisfy the requirement. The highest value obtained during all the simulations was 0.2.

3.5.2 Mesh characteristics

Keeping all the previous guidelines in mind, a 6.5 million cells mesh was created meeting all the desired requirements. 5.5 million cells that is 85% of the total were located around the rotor inside the spherical interface.

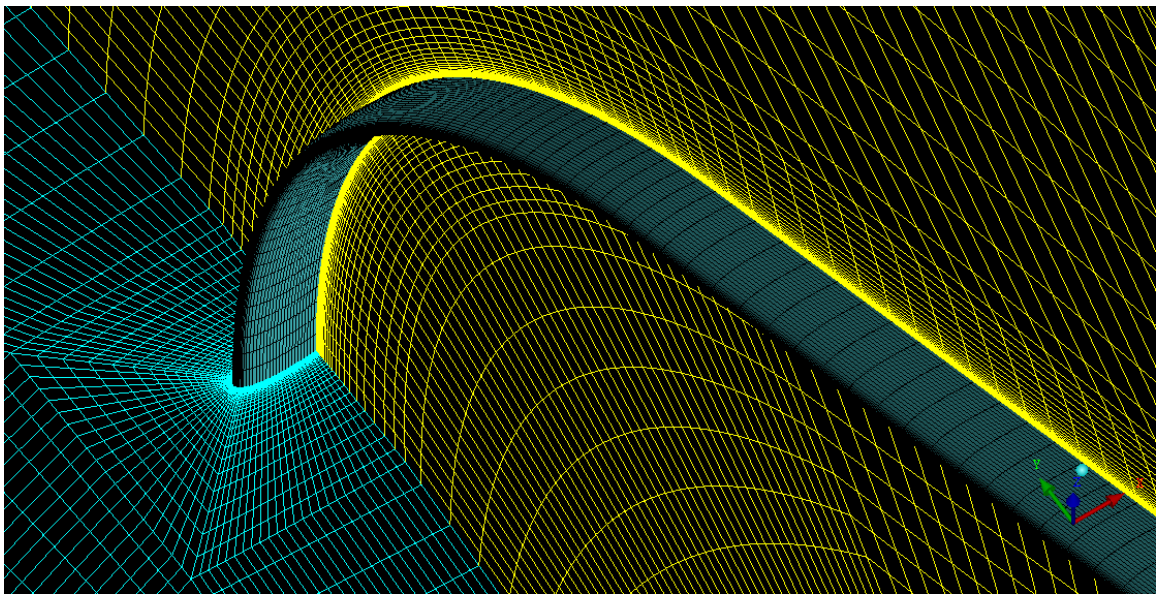

Figure 3-6: A view of the mesh around the blade.

Picture 3-6 shows the mesh refinement around the blade and some good meshing practices that were adopted: the edges coming out from the blades are orthogonal to its surface and the spanwise dimension of the elements decreases from the equatorial plane to the ends, as there is no need for high precision where the generated torque is low. On each blade there are 140 nodes in the chordwise direction and 156 nodes in

the spanwise direction. The blocking strategy which the mesh comes from is shown in picture 3-7 for the rotor and in picture 3-8 for the outer domain.

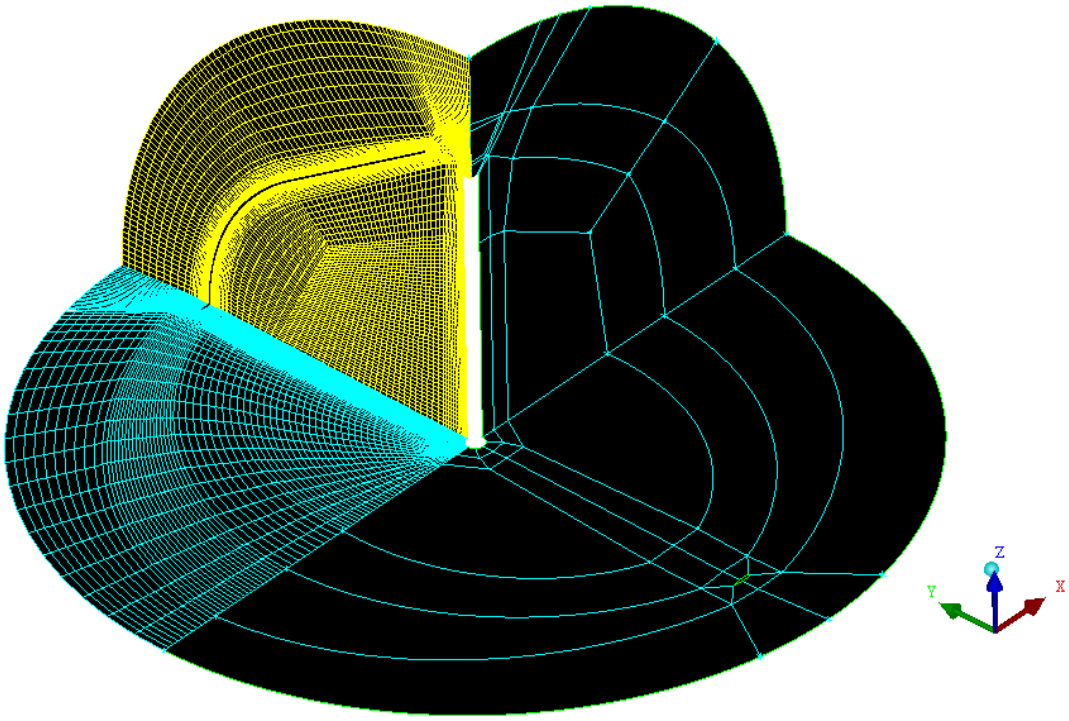

Figure 3-7: Mesh and blocking around the rotor.

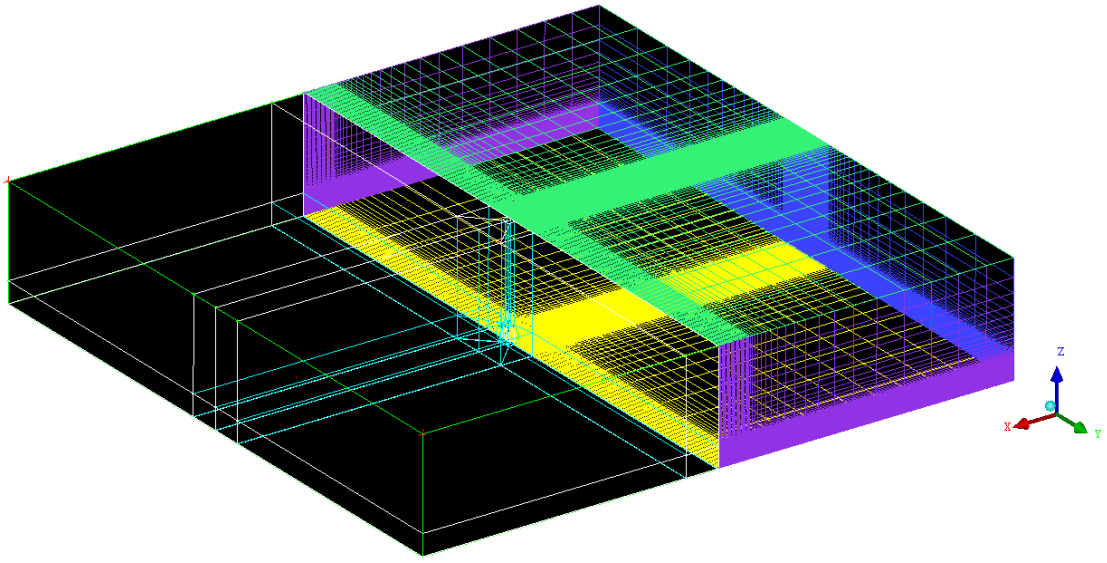

Figure 3-8: Mesh and blocking of the outer domain.

3.5.3 Mesh quality

Even though the creation of a structured mesh is more complex and takes more time than an unstructured one there are several advantages in adopting it. First of all the calculation speed, due to the indexing of elements which are given proper coordinates. To access nearby cells it sufficient to increment or decrement one of the coordinates by 1. Also, structured meshes usually require less elements as one hexahedron can be decomposed into 5 tetrahedra that share its edges. Another fundamental feature is the possibility to align the edges to the flow and to have higher aspect ratio cells, which reduces numerical diffusivity and helps representing gradients more accurately.

The present mesh was evaluated using the "angle" and "determinant 3x3x3" criteria, which show that a good quality was reached (figure 3-9).

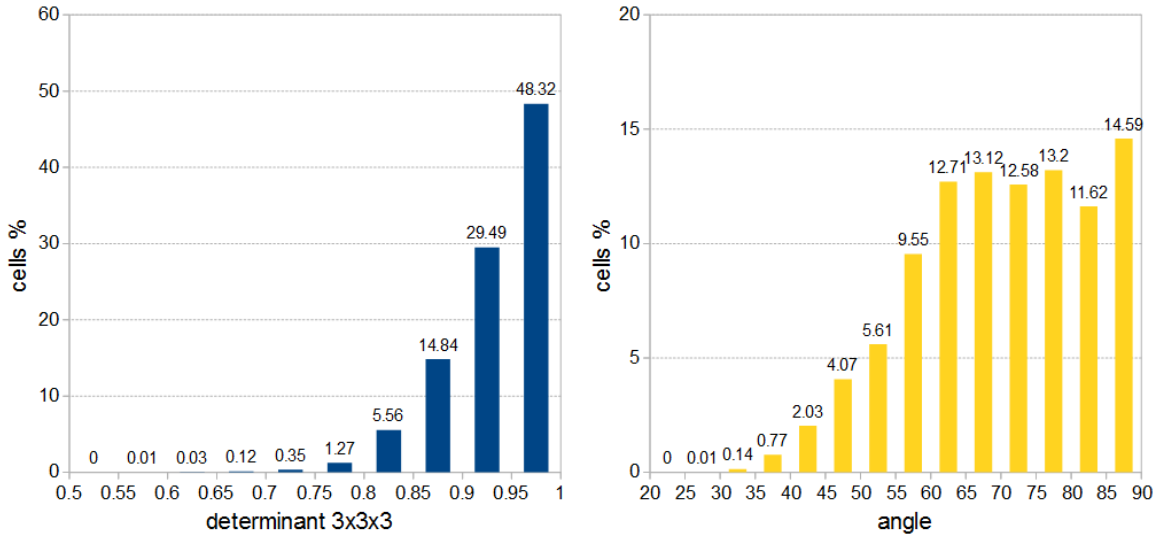

Figure 3-9: Mesh quality evaluation through the "determinant 3x3x3" and "angle" criteria.

3.6 Simulation settings

3.6.1 Turbulence model

The turbulence model has a deep influence over flow and aerodynamic forces, so its choice is all but a matter of good luck. A turbulence model has to be chosen

according to its previous results in similar applications, and if no information is present a sensitivity analysis and validation has to be performed for different models.

According to the works of Balduzzi [7], Daroczy [18], and Vernola [38] who compared different turbulence models, and of Orlandi [32,33] and Delafin [19] who studied the same turbine of this work, the $k-\omega$ SST model was chosen as it is the most broadly used for VAWTs simulations.

3.6.2 Boundary conditions

With reference to picture 3-10, the sides and the top of the outer domain were set as symmetry surfaces, the bottom which represents the ground level is a wall. On the outlet a 0 relative pressure was imposed while on the inlet a velocity normal to the surface. A turbulent intensity of 10% and a viscosity ratio of 10 were set on both of them, following the example of Daroczy [18] which proved that small values of turbulence are almost equivalent.

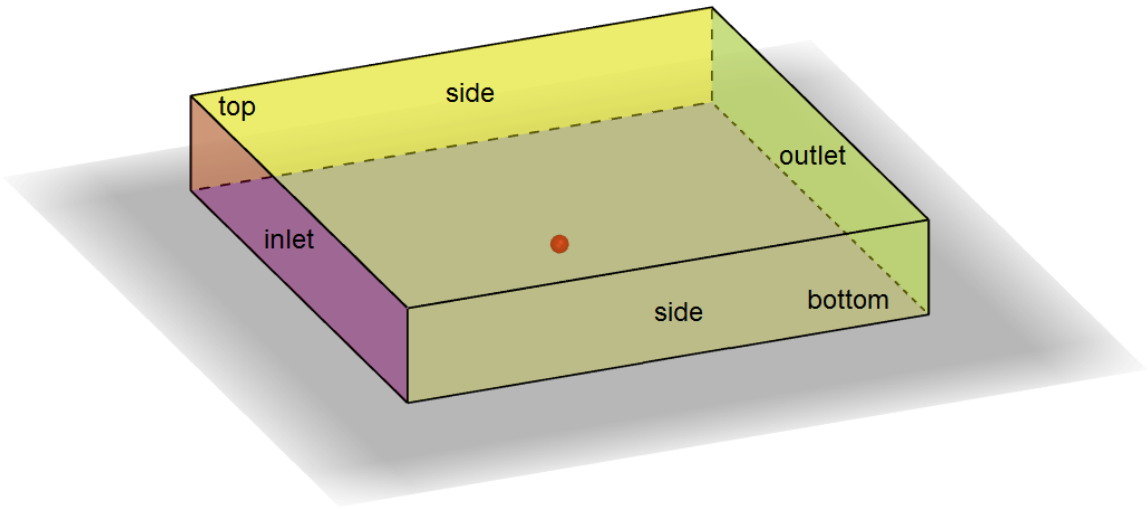

Figure 3-10: Names of the boundaries.

3.6.3 Numerical methods

For each simulation half a turn was performed using first order discretization schemes in order to avoid convergence issues, then table 3.2 settings were adopted.

Variable	Scheme
Gradients	Green-Gauss node based
Pressure	Standard
Momentum	Second order upwind
Turbulent kinetic energy	Second order upwind
Specific dissipation rate	Second order upwind
Modified turbulent viscosity	Second order upwind
Time derivatives	Second order implicit

Table 3.2: Discretization schemes adopted.

3.6.4 Convergence criteria

Since several operating conditions of the turbine were evaluated, it is important for all the simulations to have the same convergence criteria, in order to compare results with the same "degree" of convergence. This is not possible using Fluent default definition of the continuity residual, as to obtain a dimentionless parameter the absolute residual is divided by the maximum value of the residual itself in the first five iterations. In formulas:

$$Continuity\ residual\ =\ \frac{R_i}{\max(R_{1-5})}\,,$$

where R_i is the absolute value of the rate of mass generation/destruction over the domain, for iteration i. Using such a definition makes convergence dependent on the initialization, so locally scaled residuals were adopted.

A locally scaled residual is so defined:

$$Locally\ scaled\ residual\ =\ \frac{\sqrt{\frac{1}{n}\sum (R^{\phi})^2}}{\phi_{max} - \phi_{min}}\,,$$

where the numerator represents the quadratic mean of the absolute residuals over the domain.

	continuity	velocity	k	ω
convergence criterion	10^{-7}	10^{-5}	10^{-5}	10^{-5}

Table 3.3: Convergence criteria for every quantity.

The solution for a single time step is deemed to be converged when the locally

scaled residuals are smaller than the amount shown in table 3.3 for the corresponding quantity.

3.6.5 Time step

About the timestep Balduzzi [7] shows that in the majority of CFD simulations on VAWTs it corresponds to a rotation between 0.5 and 2 degrees. Moreover he performs a sensitivity analysis using angular timesteps between 0.135 and 0.405 degrees, with differences relevant only for very low tip speed ratios (=1.1). Vernola [38], Orlandi [32, 33] and Delafin [19] choose a value of 1°, so the same was adopted for this simulation.

A sensitivity analysis for the oscillating turbine simulation can be found in section 5.4.

Chapter 4

Fixed axis turbine validation

For any CFD analysis to be meaningful, a comparison against experimental, theorical or other computational data is required. Unfortunately, this request is impossible to be fullfilled in this case , since no previous analysis on floating VAWTs is available. The best it can be done, is to use the computational model created to make a prediction of the fixed axis turbine torque, which will be validated against experimental results.

In this chapter the experimental data from SANDIA laboratories [2] is presented for the working conditions chosen, paying particular attention on its accuracy. The results of the computational model are first shown and then validated against experimental data and compared with the results of independent CFD analysis from Cranfield University. Both a uniform and a power law wind profile were considered.

4.1 Experimental data

4.1.1 Accuracy

"Any measurement on an operating wind turbine represents a difficult task, mainly because of the random nature of the wind and the general unsteady nature of the entire process. This program was no exception." (Akins [2]). The report where the experimental data was taken from leaves no doubt: accuracy of the measurement and

sources of error have to be investigated and understood.

The torque of the turbine was measured using a transducer on the low-speed shaft at the base of the rotor and adjustments were made to correct the final value. These consist in adding a tare to take into account the friction and the zero drift of the transducer.

It is particularly interesting to understand how the rotor position angle (figure 4-1) was calculated, as it represents a key variable. The instrumental setting consists

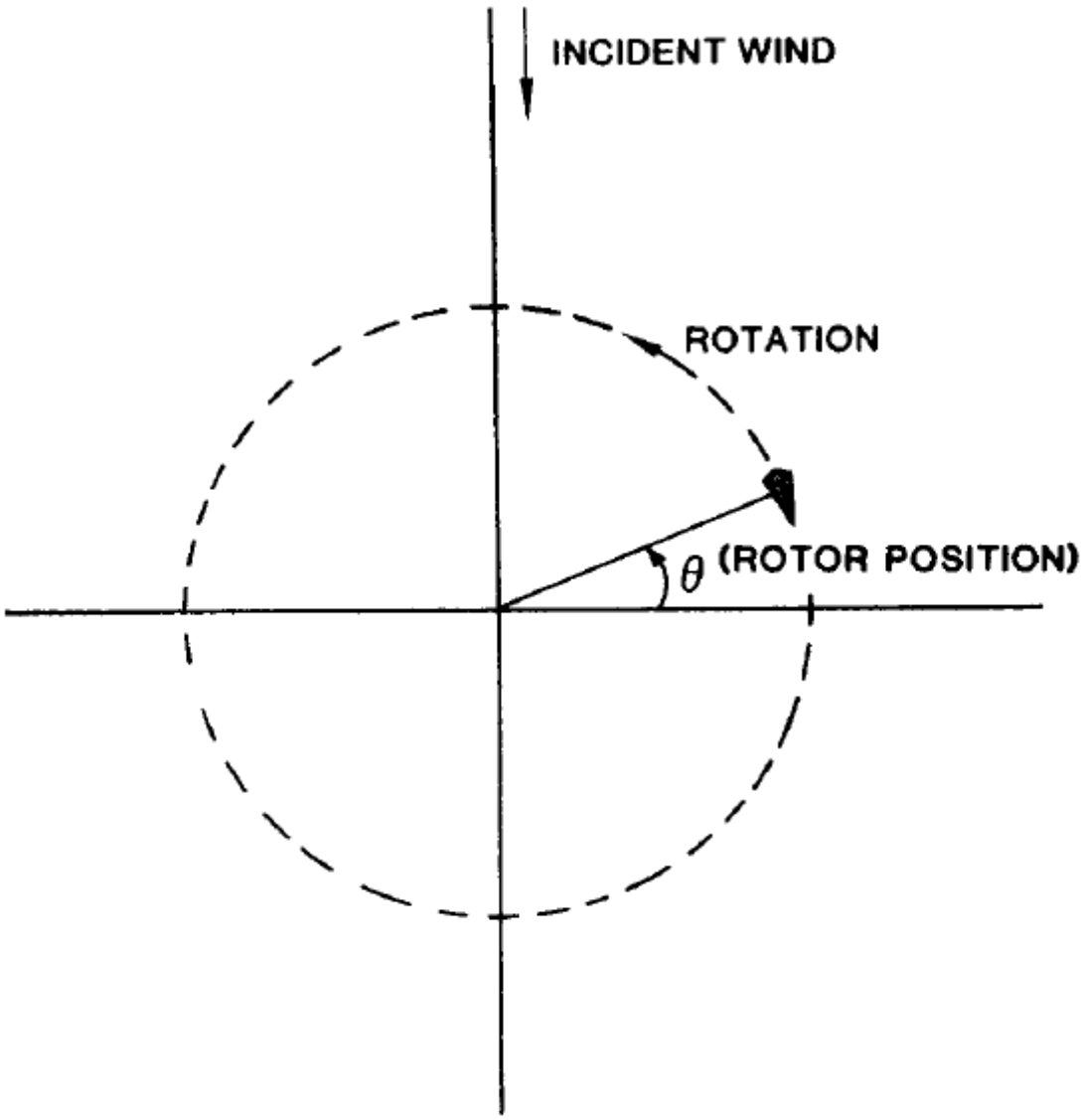

Figure 4-1: Definition of the rotor position angle θ

in an anemometer measuring the wind direction and a synchro system measuring the

absolute rotor position. As the latter was found to be affected by an offset error due to slippage relative to the rotor, a procedure was followed in order to correct it. The offset was corrected taking into account the periodic change in the angle of attack from positive to negative, which occurs when the blade velocity is tangent to the wind direction. A combination of a Pitot-static probe and yaw probe was used for the measurement. The procedure followed is claimed to cause at most an error of $\pm 6°$, so using the formula which gives the angle of attack versus the rotor angle

$$\tan \alpha \;=\; \frac{\sin \theta}{\lambda + \cos \theta}\,,$$

it is possible to estimate that the yaw probe resolution was $\pm 1°$ (considering $\lambda = 4.6$).

In order to determine the torque as a function of wind speed and rotor position the methods of bins was used. The wind speed bin is 0.447 m/s wide, while the rotor position bin is $6°$.

Finally, basing on bin standard deviation an accuracy of 10% of the reading or 5% of the peak torque is given as a reference, even though the author of the report itself admits that "it is not possible to make a definitive statement about the accuracy of the data".

4.1.2 Operating conditions

Two different tip-speed-ratios were chosen: 2.02 which is the smaller one available, and 4.6 which is the one of maximum power coefficient of the turbine. The two operating conditions are very different both for the torque curve and the phenomena which influence it. For the lower TSR dynamic stall is expected to happen, as the maximum static angle of attack predicted goes far beyond the static stall limit. For this reason, the lower TSR is the more difficult condition to be simulated between the two.

Measures have been corrected to a common arbitrary density of 1 kg/m^3. The turbine is operated at a constant rotational speed of 38.7 rpm. Reynolds number is $9.6 \cdot 10^5$ based on the chord and tip-speed of the blade at the equatorial section.

Wind speed and dynamic viscosity were derived from the given values and reported in table 4.1 with all the other parameters.

TSR	$U_\infty\ [m/s]$	$\omega\ [rad/s]$	$\mu\ [kg/m \cdot s]$	$\rho\ [kg/m^3]$	Re
2.02	16.780	4.0527	$2.1538 \cdot 10^{-5}$	1	$9.6 \cdot 10^5$
4.6	7.369				

Table 4.1: Reference values for the two operating conditions.

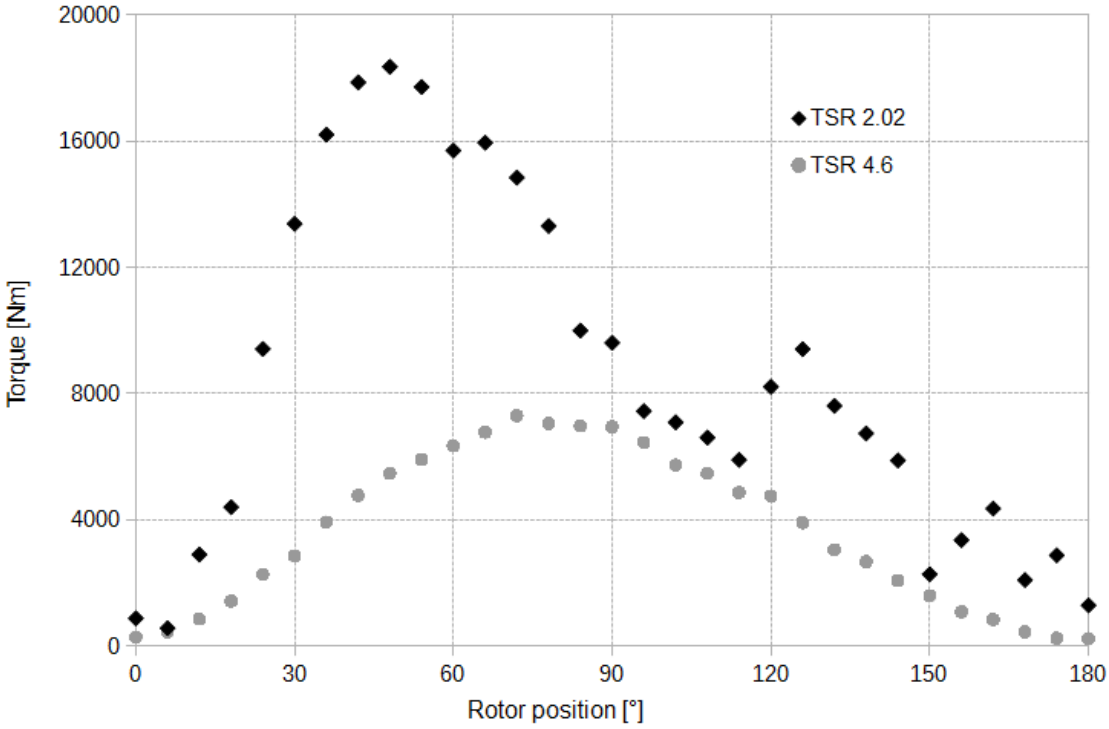

Figure 4-2: Experimental torque vs. rotor position angle.

In order to represent the atmospheric boundary layer wind profile on the site of the turbine, the SANDIA report [2] suggests the following power law:

$$U(h) \ = \ U_\infty \left(\frac{h}{13.5} \right)^{0.1} ,$$

where U represents the wind speed at a certain height h from the sea/ground level and 13.5 is the height in meters of the equatorial section of the turbine.

4.2 CFD simulations

4.2.1 Uniform wind profile

A uniform wind profile was set for the inlet boundary, whose variables were used to initialize the flow field. During the first 180° of rotation for TSR=2.02 and 270° for TSR=4.6 the solution methods were first order for every variable, then as explained in paragraph 3.6.3. The simulation was stopped when the relative difference of torque between two consecutive half-turns was less than 1%. For the TSR of 2.02 three and a half turns were needed to match the condition, while for the TSR of 4.6 four turns were performed (figure 4-3).

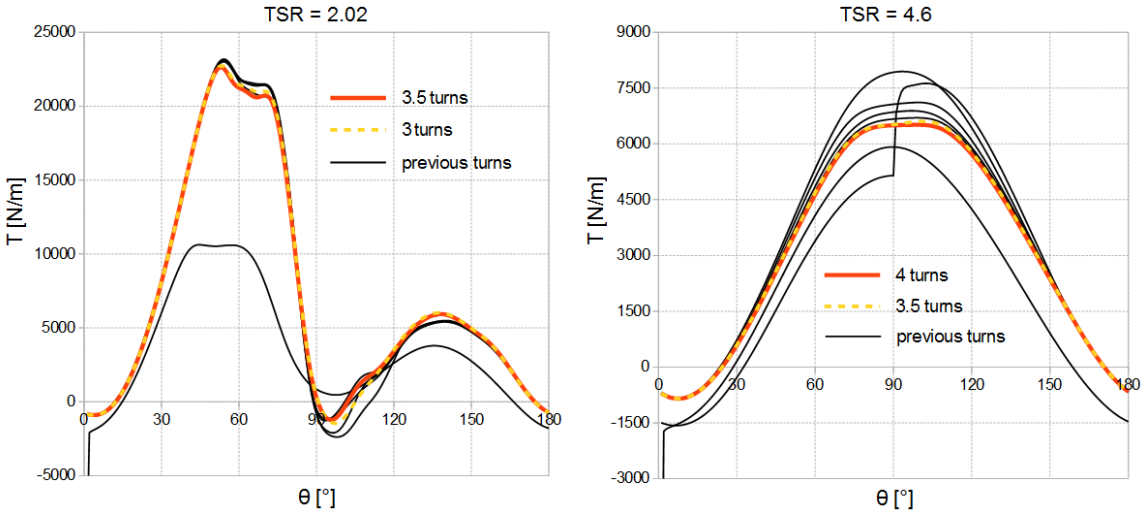

Figure 4-3: Torque versus rotor position for all the revolutions performed.

4.2.2 Power law wind profile

In order to start the simulation the wind profile had to be initialized through the whole domain by the means of a stationary simulation with the turbine fixed in the initial position, that is with blades aligned with the wind. Afterwards the same procedure was adopted, so 180° were performed with a first order discretization scheme and then second order as reported in paragraph 3.6.3. For TSR=2.02 again 3 and a half revolutions were performed which ensured the 1% difference convergence criterion.

For TSR=4.6 instead 5 revolutions were performed, one more than before, in order to increase the accuracy, so the relative difference between the last turn was 0.65%.

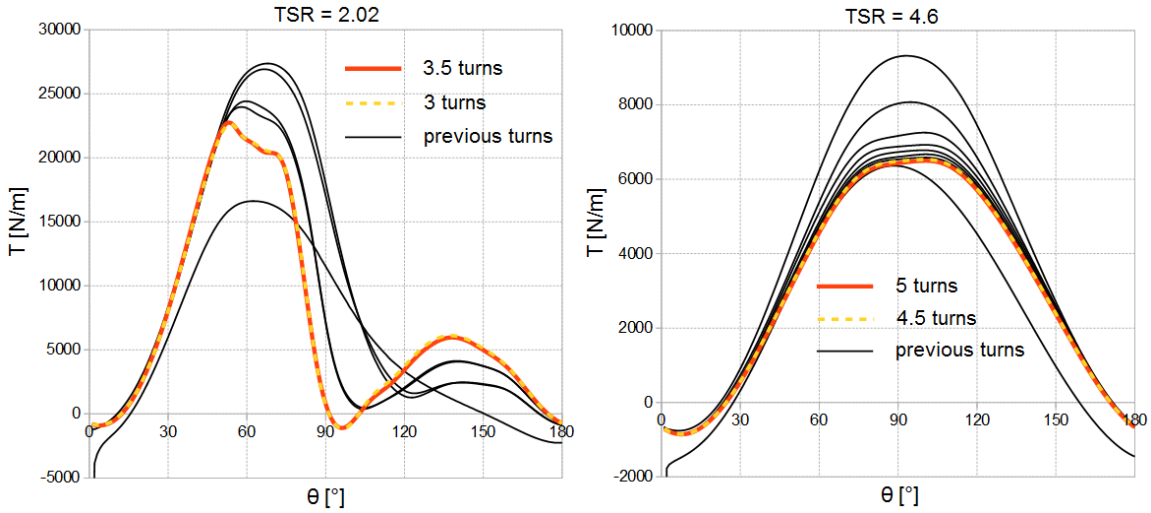

Figure 4-4: Torque versus rotor position for all the revolutions performed.

For TSR=2.02 the maximum number of iterations per time step was gradually increased from 40 in the first 3.5 revolutions, to 50 in following revolution and finally to 70 in the final one, so it is possible to see the effect of this parameter on torque. Differently from the first 2.5 revolutions in the last one the maximum limit of iterations was not reached so the solution converged according to the convergence criteria reported in paragraph 3.6.4.

The introduction of the atmospheric boundary layer through the power law wind profile left the torque almost unchanged (figure 4-5). In order to compare an equally developed flow, for TSR=4.6 the curves both show the torque during the fourth turn. The reason of such a small difference have to be searched in the the shape of the Darrieus turbine, which has a wide equatorial section which progressively shrinks as you get closer to the top and bottom. Considering the torque distribution over the hight of the the turbine we can expect to find the maximum value at the equatorial section and zero at the ends where the radius becomes small. Being the majority of the torque acting on the equatorial section there is no surprise that introducing the atmospheric boundary layer does not modify torque, as in the proximity of that plane the wind speed is close to the uniform profile value. Where the differences in the wind

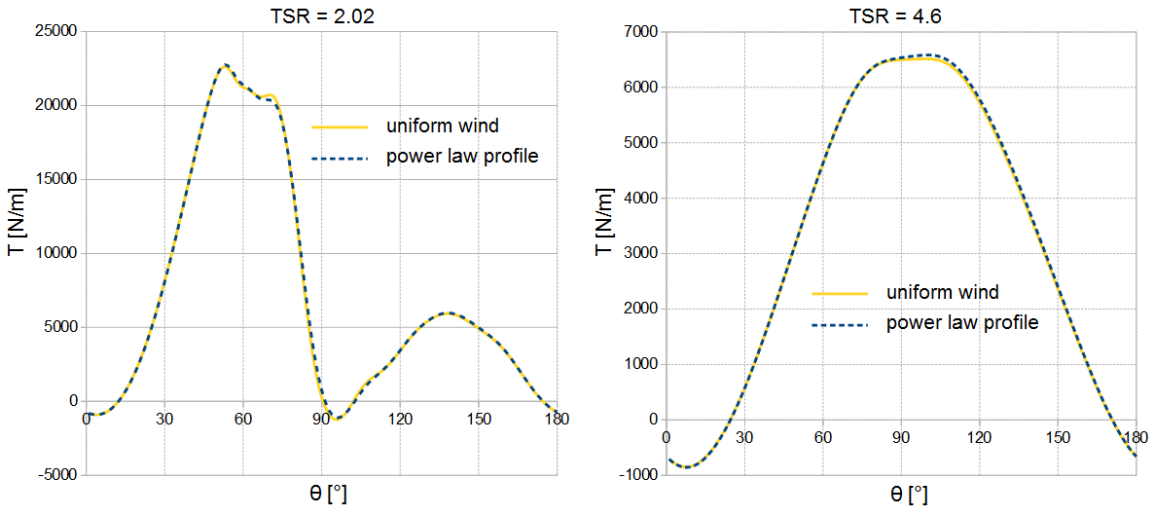

Figure 4-5: Torque comparison between the simulations with uniform and power law wind profile.

intensity are stronger, that is at the ends of the turbine, the radius of the blades is small so their contribution on the overall torque is not enough to cause significative changes.

4.3 Validation

The torque curves obtained in this work were compared against the experimental data gathered by Sandia laboratories discussed in paragraph 4.1 and the results from an independent CFD analysis available at Cranfield University. The latter is a 3D URANS analysis using a structured grid of 9 million cells, carried on using the software CFX. Data for TSR=4.6 can be found in [19] by Delafin, Nishino and others.

For TSR=2.02 (figure 4-6) the present numerical analysis gave similar results to the one performed in Cranfield with the exception of the peak torque prediction. Even though both studies overpredict it the present one is closer to experimental results. The most critical part to simulate ranges approximately from 80 to 130 degrees, in which the torque drops rapidly before reaching even a negative value and then slowly restores right before the second lower peak. As can be observed in picture 4-8 the steep torque decrease in this part coincides with the dynamic stall of the blade passing

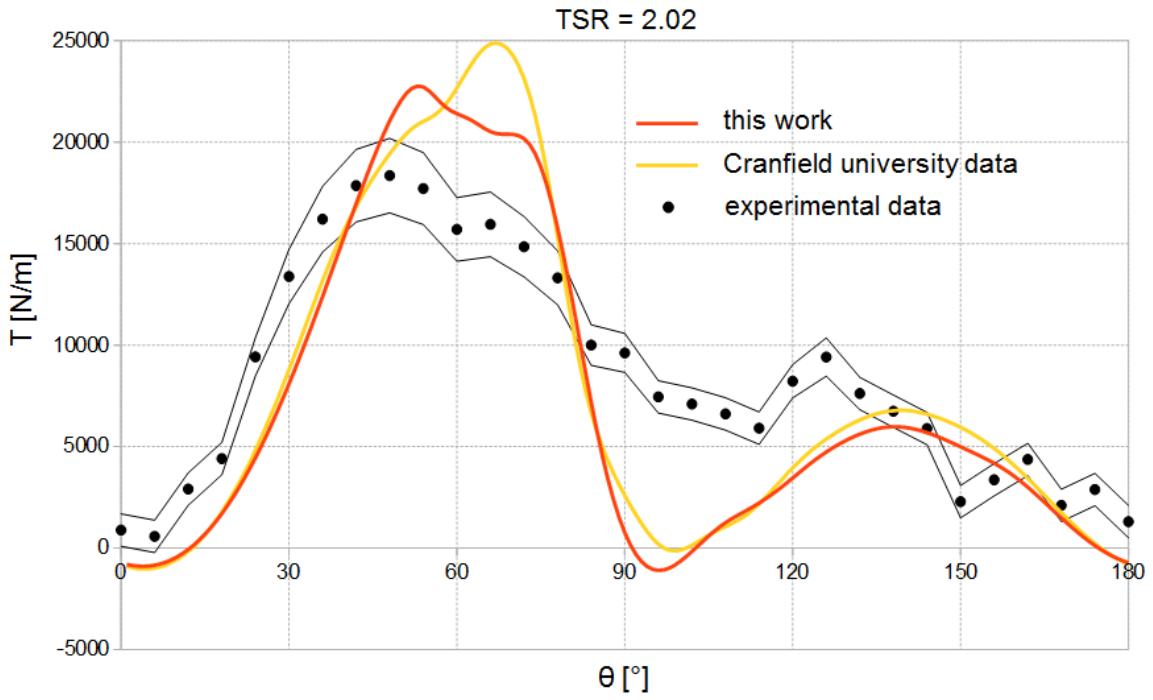

Figure 4-6: Overall torque comparison against experimental and Cranfield University data for TSR=2.02.

upwind, which Ferreira [20] proved to be a phenomenon that URANS simulations fail to represent accurately. For TSR=4.6 (figure 4-7)the maximum power coefficient is reached so the presence of dynamic stall should be limited and the simulations are expected to be closer to the experiments, which is what happens with the exception of a 10 to 20 degrees delay. Again the two numerical simulations are in good agreement with each other, apart from the zone in which the maximum torque is reached. Even though in this work the peak is lower it is still in the range of the standard deviation of the experimental data. Looking at the blade torque (figure 4-8) we clearly see that the difference between the two simulations is due to a different prediction of the upwind peak, immediately after the 90° rotor position. The last important disagreement between the numerical models and the experiments is the behaviour around 0° where drag is the leading force. A negative torque is predicted, whereas in reality its value seems to be always positive.

To conclude let us examine the previous work by Orlandi [33], a 3D URANS simulation with an unstructured mesh validated through the tangential and normal

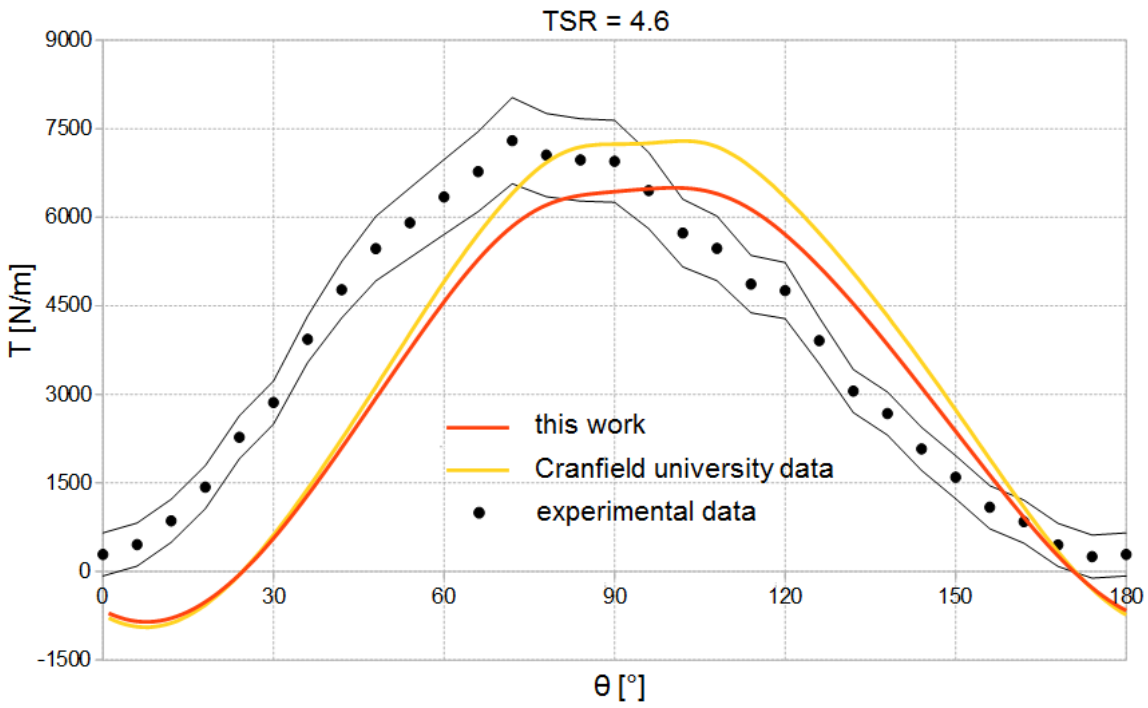

Figure 4-7: Overall torque comparison against experimental and Cranfield University data for TSR=4.6.

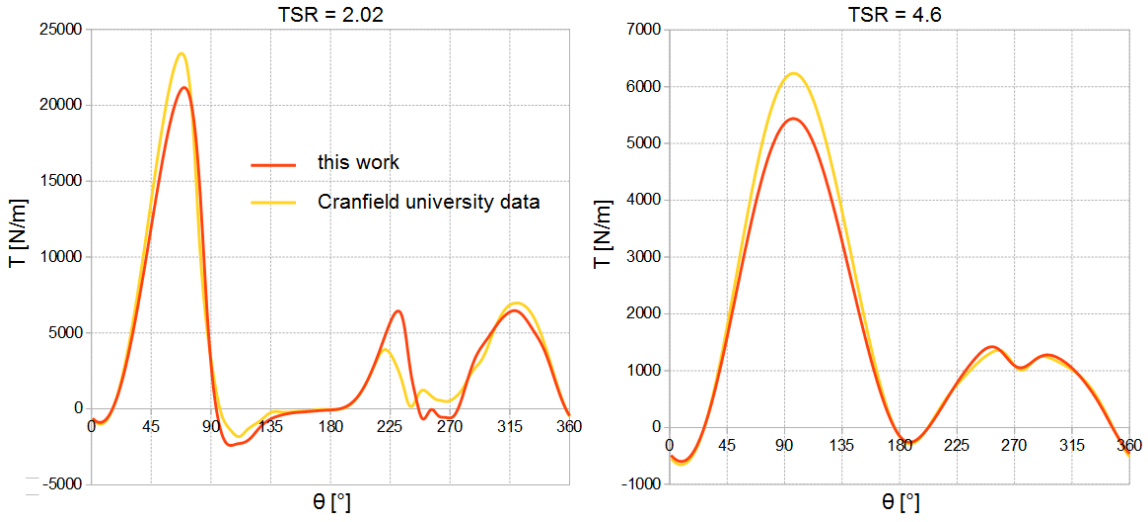

Figure 4-8: Blade torque comparison against Cranfield University data.

forces acting on the equatorial blade element. Figure 4-9 reports the coefficient of tangential force only as this is the component giving torque.

The curve for TSR=2.33 confirms that when dynamic stall is present URANS simulations cannot predict the aerodynamic tangential force accurately. Common

errors are found in all the three analysis discussed, that is the peak is overpredicted and delayed.

The results for TSR=4.6 show an underpredicted tangential force coefficient though the qualitative behaviour is well represented, angular position of all the peaks included. This is a substantial difference with the present analysis, in which an evident error right on rotor position is present, a factor which makes us question the validity of the reduction procedure on the experimental data (paragraph 4.1.1) even more.

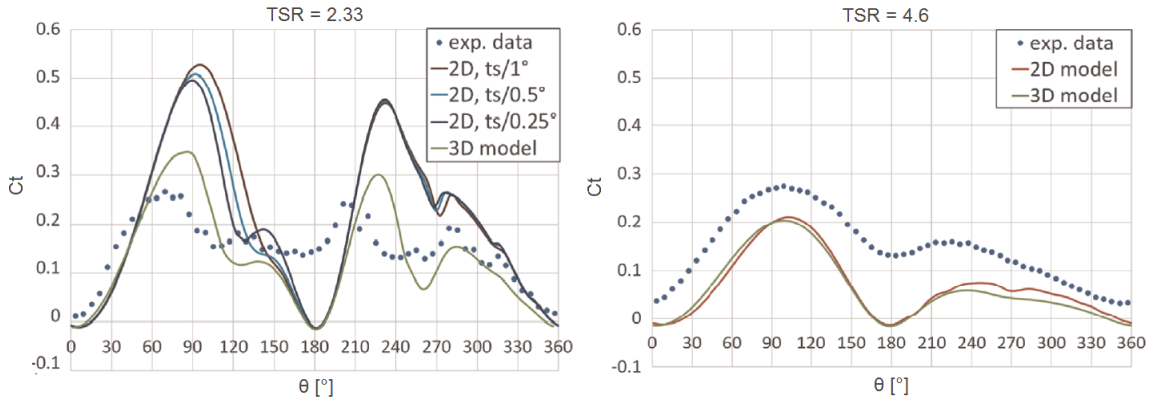

Figure 4-9: Comparison against experimental and Cranfield University data for TSR=2.02.

Chapter 5

Periodically oscillating turbine analysis

In this chapter the results of the CFD simulations on a periodically oscillating wind turbine are presented. Firstly, an overview on the dynamics of floating VAWTs is made in order to understand why the motion was restricted to just one degree of freedom and how the operating conditions were chosen. Secondly the dynamic mesh setting is explained, paying particular attention on the problems which emerge for simulations with moving interfaces and how they were overcome in this work. Finally the effects of oscillation on both blade and overall torque are clearly shown as well as the results from the sensitivity analysis on the timestep.

5.1 Dynamics of a floating VAWT

The motion of a floating wind turbine is three dimensional in both rotation and translation. Analysing it requires complex tools capable of accounting for all the forces acting on the system, that is gravitational, buoyant, inertial, aerodynamical, elastic and moorings contact forces. It is out of the scope of this analysis to provide a detailed representation of the motion of a floating structure, but since its major features have to be understood two articles will be analysed.

Borg [12] has performed a frequency-domain analysis on the 5MW DeepWind

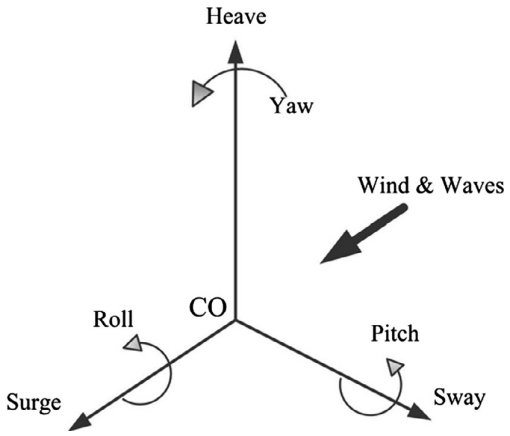

Figure 5-1: 6 DOFs.

VAWT developed by Vita [39], in which the amplitude spectral densities (ASD) for the 6 degrees of freedom (DOF, figure 5-1) were evaluated. A JONSWAP wave energy spectrum with a peak energy density at 0.6 rad/s was employed. From the ASDs (figure 5-2) we can see that the most relevant motions are pitch, surge and heave, moreover there is significative structure motion in the range between 0.3 and 1.2 rad/s with a maximum around 0.6 rad/s which corresponds to the one of the wave spectrum considered.

As regards the amplitude of oscillation, Coulling [17] provides minimum and maximum pitch angles from both experiments and FAST[1] simulations on a 1/50 scaled model of the 5MW DeepWind turbine. Results (table 5.1) show oscillation amplitudes below 5° with or without wind. In the latter case is shown that oscillation happens around an inclined axis, because of the aerodynamic thrust force caused by momentum extraction.

DOF	Conditions	Source	Mean	Max	Min
Pitch [°]	Waves	FAST	0	3.15	-3.10
		Experiments	-0.06	4.50	-4.15
	Waves and wind	FAST	3.42	6.70	-0.05
		Experiments	3.49	8.66	-1.33

Table 5.1: Coulling [17] data on pitch for a 1/50 scaled model of the 5MW DeepWind turbine.

[1]FAST is a NREL's CAE tool for simulating the coupled dynamic response of floating wind turbines.

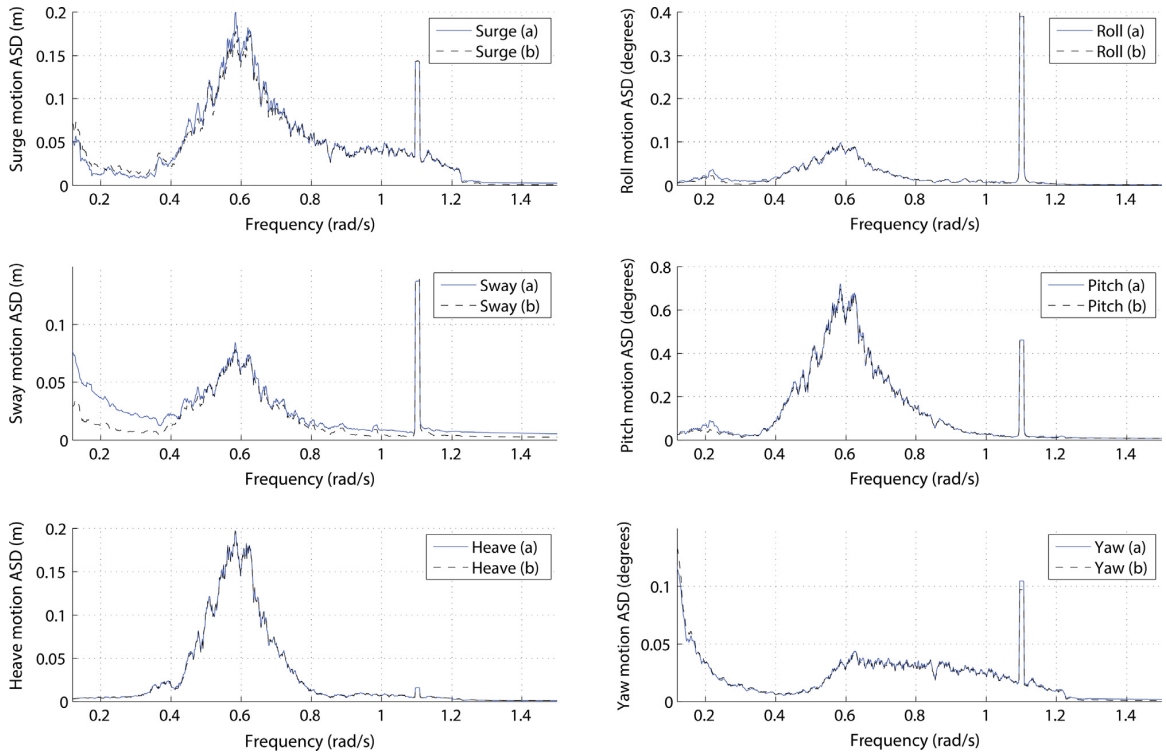

Figure 5-2: Borg [12] ASDs for the 5MW DeepWind floating VAWT.

5.2 Law of motion

Being this study an aerodynamical description of a floating VAWT there is no need to represent faithfully its real motion on a platform as long as it has little influence. In this analysis in fact only pitch was considered, in order too keep just one degree of freedom without loosing representativeness. Moreover even though a real floating turbine would pitch around an inclined axis because of the overturning moment caused by the aerodynamical thrust, an oscillation around a vertical axis was considered. Finally, steady wave conditions were considered, so oscillation has a constant frequency and amplitude and occurs in the same direction of wind. Taking into account these simplifications led to the following pitch angle law:

$$\beta \ = \beta_{max} \sin(\omega_o t)\,, \tag{5.1}$$

where β_{max} is the amplitude and ω_o the oscillation frequency in rad/s.

As regards the amplitude 10° were chosen in order to test a limit case compared

to what by Coulling [17] (table 5.1), whereas the two oscillation frequencies chosen are representative of possible conditions met during real operation (table 5.2).

Conditions	Oscillation frequency [rad/s]	Amplitude [°]
Wave peak energy	0.6	10
Extreme oscillation	1.2	

Table 5.2: Working conditions for the aerodynamic simulation.

Being the rigid body motion of the turbine fully defined, we can represent it using an absolute reference system $Oxyz$ and one integral to the turbine itself $O'x'y'z'$. In particular we can express velocities through the velocity of O' and the angular velocity vectors:

$$\boldsymbol{V}_P \;=\; \boldsymbol{V}_{O'} + \boldsymbol{\omega} \times \boldsymbol{O'P}\,. \tag{5.2}$$

Placing the relative reference system with its origin in the centre of the turbine leads to

$$\boldsymbol{V}_{O'} \;=\; \begin{pmatrix} \dot{\beta} H \cos\beta \\ 0 \\ -\dot{\beta} H \sin\beta \end{pmatrix}\,, \tag{5.3}$$

where $H = 13.5\ m$ is the distance from the centre of the turbine from the oscillation axis. The angular velocity in the absolute reference system is

$$\boldsymbol{\omega} \;=\; \begin{pmatrix} \dot{\theta} \sin\beta \\ \dot{\beta} \\ \dot{\theta} \cos\beta \end{pmatrix}\,. \tag{5.4}$$

5.3 Dynamic mesh

In order to let the turbine oscillate it is necessary for part of the mesh to deform over time. The strategy adopted to achieve the result consists in making the deforming mesh to behave like a net of springs whose stiffness depends on their length; in particular, the shorter the stiffer, in order to avoid contact between closer nodes. The method is already implemented in FLUENT named "spring-based smoothing" and it

contains three user defined tuning parameters. The first one is the spring constant factor k_{fac} which regulates the spring stiffness

$$K = \frac{k_{fac}}{\sqrt{\Delta x}}. \tag{5.5}$$

The other ones are a convergence criterion and a maximum number of iteration, which are needed since the solution of the nodes displacements is obtained iteratively. Since the time necessary to update the node position is much than the time for the flow calculations it is not vital to keep the maximum number of iterations low. On the contrary it is important to set it high enough to avoid negative volume cells and to keep mesh quality satisfactory.

Two different interface motions were tested: in the first case the interface is integral to the rotoric mesh so it translates and rotates around its centre at the same time, while in the second only translation was allowed. The latter was adopted for the simulation as it reduces the overall cell deformation especially close to the interface (figure 5-3).

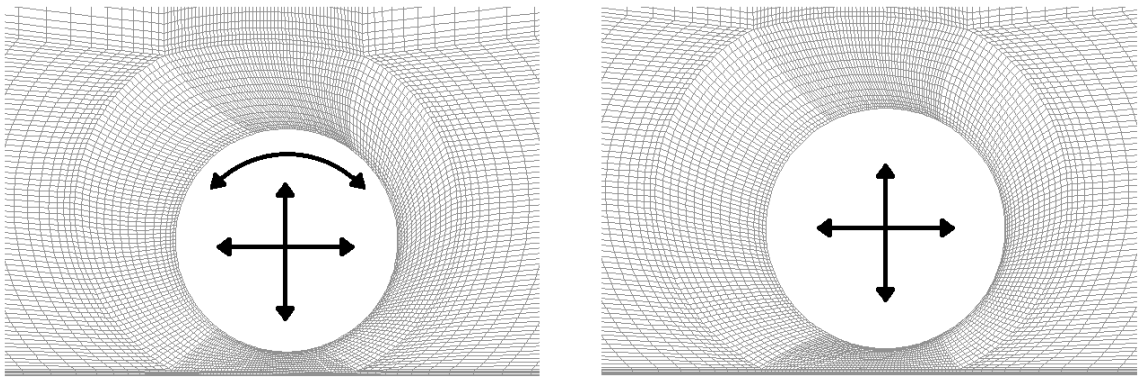

Figure 5-3: Comparison between two different interface motions: left rotation and translation, right translation only.

See appendix A for the user defined function (UDF) code which is required to implement the turbine and the interface motion in FLUENT.

5.3.1 Discretization errors

Particular care has to be given to how the simulation software obtains the trajectories of a rigid body, as unexpected errors due to time discretization may cause unwanted relative motion of elements facing the sliding interface. We will now investigate the procedure followed by FLUENT to update the position of rigidly moving parts of the mesh.

Once that linear and angular velocity of a rigid body have been defined it possible to obtain the position and the orientation of the moving frame $O'x'y'z'$ over time. In a time-discrete simulation this is done by numerical integration of $\boldsymbol{V}_{O'}$ and $\boldsymbol{\omega}$, considering them constant for the the whole timestep. Therefore the position of O' is updated using the following formula:

$$\boldsymbol{x}_{O'}^{t+\Delta t} = \boldsymbol{x}_{O'}^{t} + \boldsymbol{V}_{O'}^{t} \Delta t \,. \tag{5.6}$$

Figure 5-4 provides an example of how this procedure leads to a mismatch between the real trajectory of a point moving on a circumference at constant speed and the numerically integrated one.

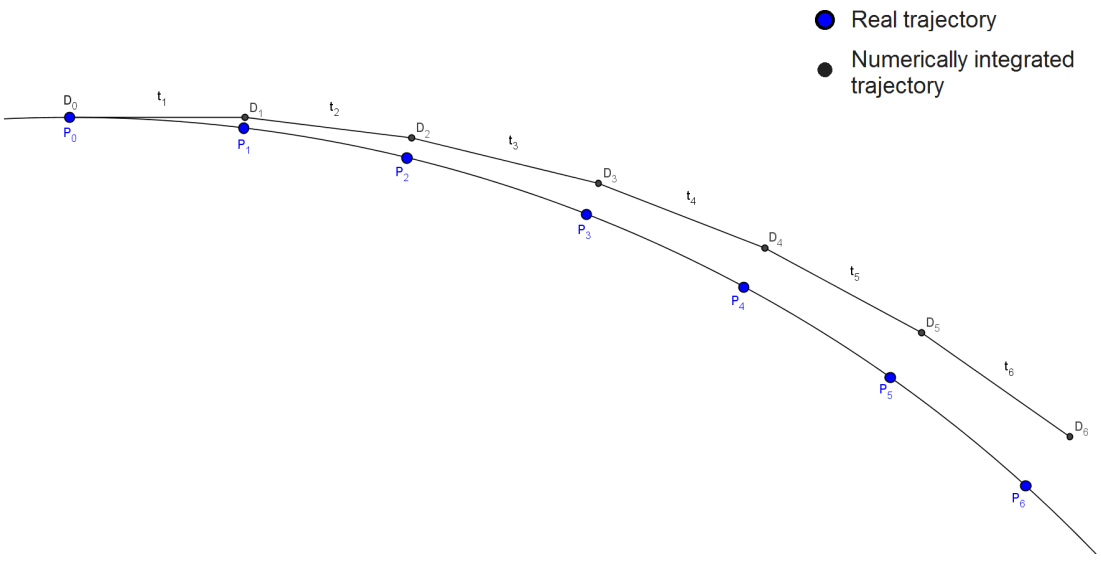

Figure 5-4: Discretization error on the position of a point moving of uniform circular motion.

As regards the orientation of the moving reference FLUENT updates the rotation angles following the order z-y-x, which being rotations around different axes not commutative introduces further numerical error. However infinitesimal rotations are commutative, so this error plus the one resulting from a piecewise constant $\boldsymbol{\omega}$ would decrease as the timestep becomes smaller. The formula to update the rotation around one of the axis, say z, is:

$$\phi_z^{t+\Delta t} \;=\; \phi_z^t + \omega_z^t \Delta t \,. \tag{5.7}$$

The practical effect of such a discretization error on an oscillating turbine simulation is that the motion stops being a pure precession and that nutations appear. In other words the rotation axis is expected to lay only in the z-x plane when actually this constraint is not respected, which could cause the elements facing the sliding interface to penetrate each other making the simulation crash.

To solve the problem the moving reference frame of the rotor mesh and of the interface were both set coincident to the centre of the turbine at the beginning of the simulation. Having the same velocity their origins would be coincident at any timestep, as the error on the angular velocity cannot influence their position. Even though the nutations are still present they can cause no damage, as with a spherical interface every rotation is allowed and luckily the timestep sensitivity analysis (paragraph 5.4) proves they are small enough not to influence the torque.

5.4 Sensitivity analysis on the timestep

To evidence the results dependency on the timestep a sensitivity analysis was performed, halving it from 1° to 0.5°. In this simulation there are three sources of error which depend on the timestep and whose effect is going to be evaluated through this analysis:

- the discretization error in the fluid zone, given by the representation of time derivatives
- the discretization error regarding the motion of the turbine, which in paragraph

5.3.1 was shown to perform nutations

- the error on the torque reading.

As regards the last point, the moments in the z and x direction acting on the blades were measured with respect to the axis of oscillation, which lays on the water level in the direction of the y axis. Obtaining the torque on the turbine axis is a matter of projecting vectors:

$$T = M_x \sin\beta + M_z \cos\beta \,. \tag{5.8}$$

These considerations are true only if the turbine follows the real trajectory, so it is important to asses whether the mismatch is influential or not.

The results for the lower oscillation frequency (figure 5-5) show that the overall torque is practically timestep independent, so the analysis on the other oscillation frequency was deemed to be redundant.

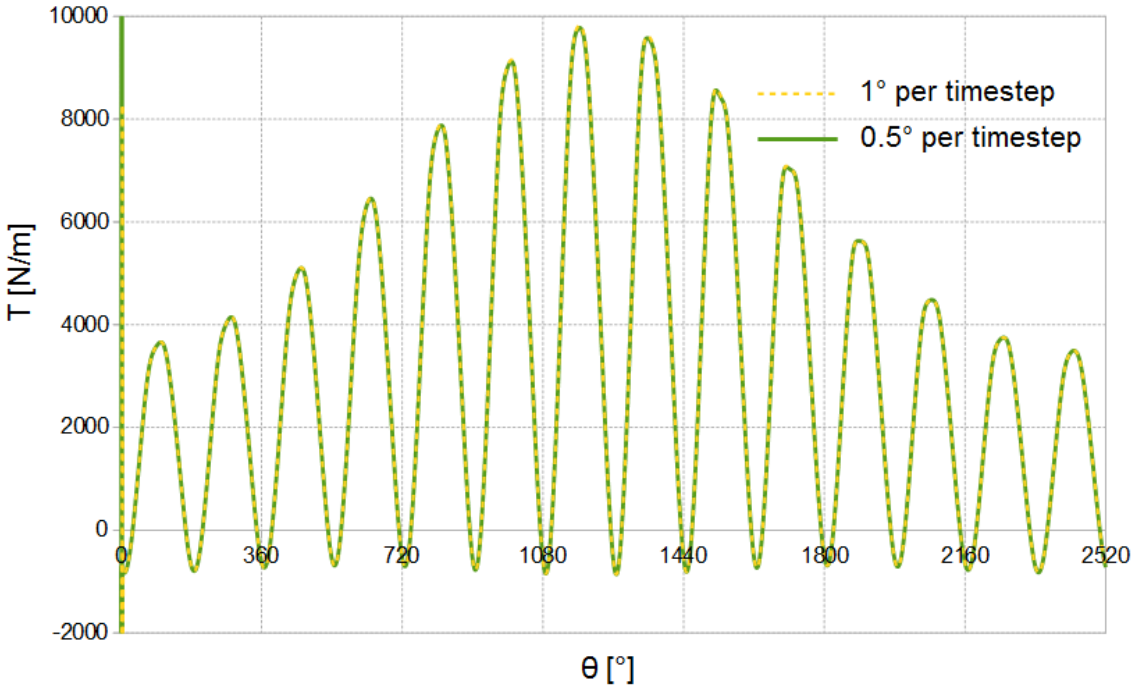

Figure 5-5: Sensitivity analysis on the timestep for $\omega_o = 0.6\ rad/s$.

5.5 Results

Two simulations corresponding to the two different motions pointed out in table 5.2 were performed. As regards the wind and the rotational velocity the values from the fixed axis turbine simulation for TSR=4.6 were preserved, as the validation gave better results for this condition. Another reason for this choice is practical: the solution was initialized using the flow field resulting from the fixed axis simulation, making convergence easier to be reached because the wake had already started to develop.

Four complete oscillation periods were performed, which correspond approximately to 27 revolutions for $\omega_o = 0.6\ rad/s$ and to 13.5 for $\omega_o = 1.2\ rad/s$. Considering that to complete 27 revolutions using 32 CPUs 13 days were needed, it means that each second of flow simulated required almost 240 hours of CPU time, that is about 7 hours and 45 minutes of real time.

The overall and blade torque are deeply affected by the motion of the turbine (figure 5-6 and 5-7) which introduces an harmonic with the same period of oscillation. Plotting the oscillation angular velocity $\dot{\beta}$ together with the torque leaves no doubt

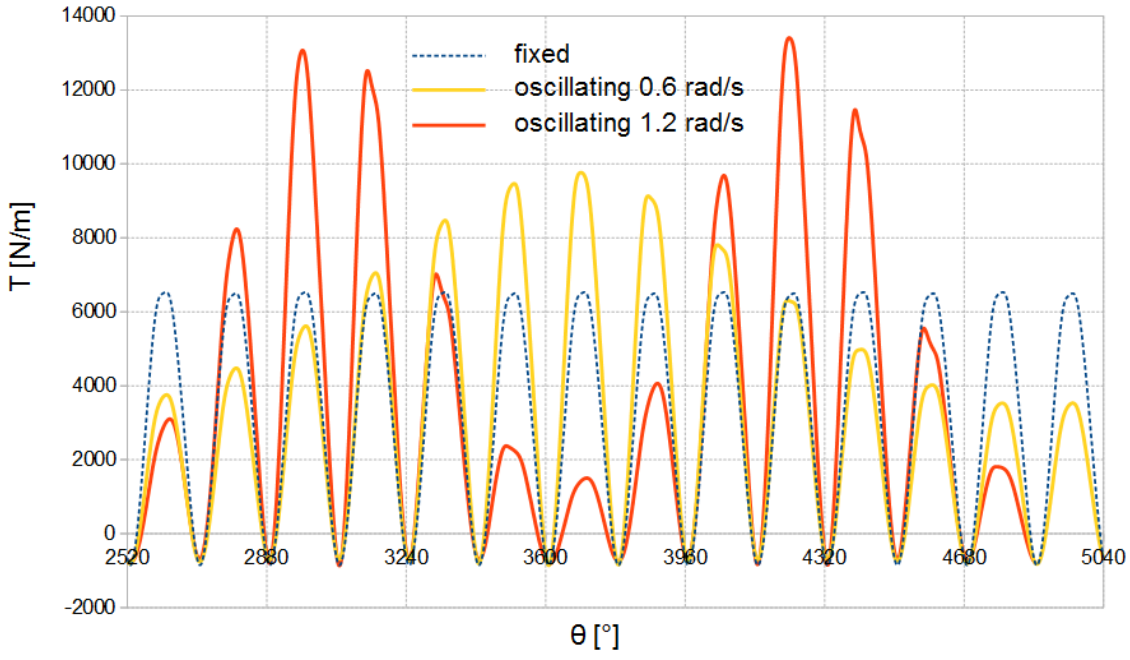

Figure 5-6: Overall torque of the oscillating and fixed turbine.

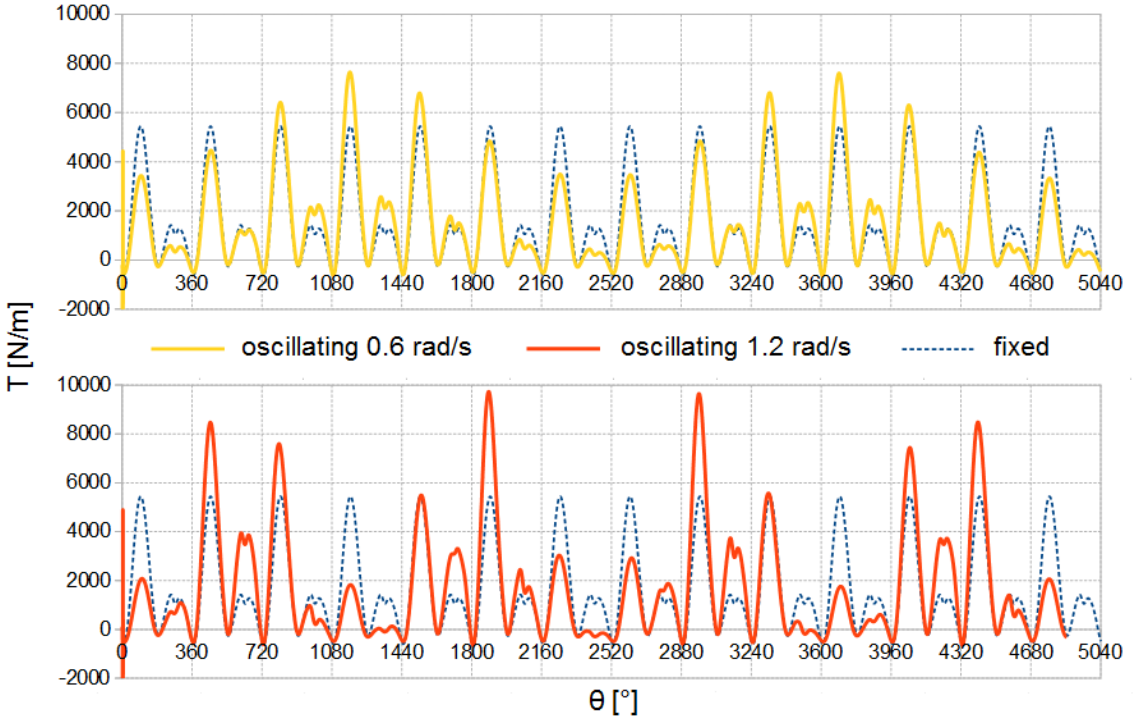

Figure 5-7: Blade torque of the fixed and oscillating turbine

on the correlation existing between them (figure 5-8). In particular when the turbine pitches in the same direction of the wind ($\dot{\beta} > 0$) the torque decreases as the effective wind intensity is diminished, while when pitching occurs in the opposite direction ($\dot{\beta} < 0$) the increased relative wind speed generates to more torque.

This modified relative wind speed have little influence on the negative peaks of torque, which is perfectly explained considering that when torque is negative the angle of attack is almost 0. The leading force on an airfoil in that condition is drag, which is not very sensitive to changes in the wind intensity. Lift caused torque instead is deeply affected by oscillation induced velocities, in fact the maximum peak of the overall torque can be as much as double the value of the fixed axis turbine. The topic will be further discussed in chapter 6 since the theorical model developed will give a precise explanation of the phenomenon.

A key factor for evaluating the performance of a wind turbine is its mean torque, but defining it for an oscillating turbine and understanding if initial time effect have disappeared can be a tricky task, which will be discussed in the following paragraph.

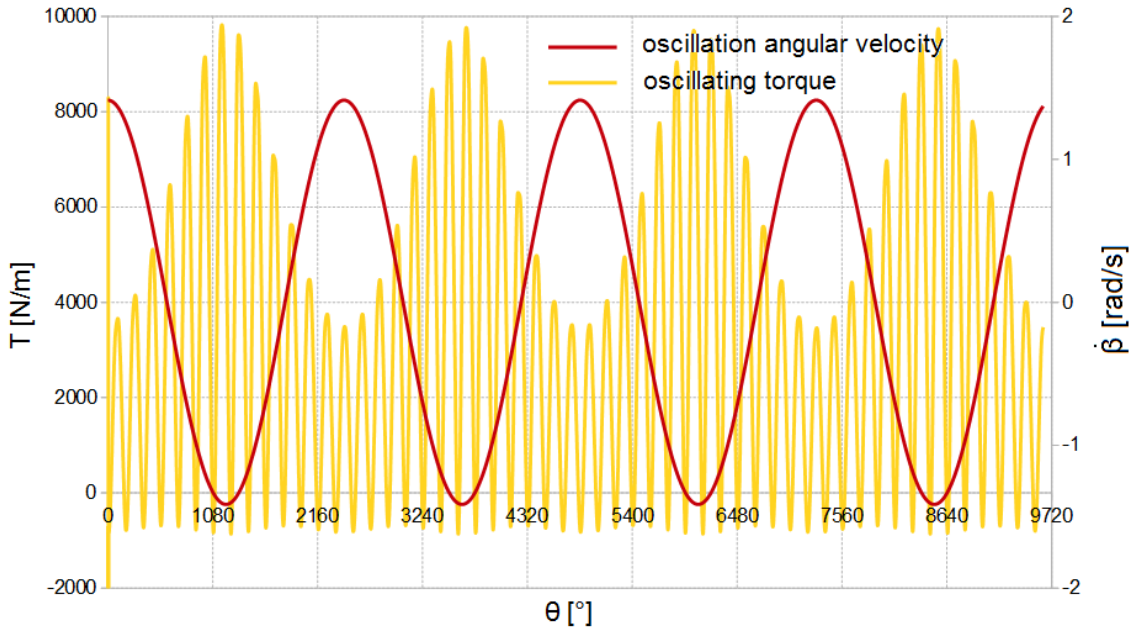

Figure 5-8: Overall torque and oscillation angular velocity for $\omega_o = 0.6\ rad/s$.

In order to overcome the problem in an easy way the mean was calculated using just the last three oscillations out of four. The effect of oscillation on mean torque and so on energetic performance seems to be positive for the higher frequency and slightly negative for the lower one (table 5.3), but the accuracy of the analysis performed is not enough to let us conclude that the higher the oscillation the more energy is gathered.

Certainly it is possible to conclude that oscillating Darrieus turbines have almost the same energetic performance as if they were fixed, but unfortunately such a positive feature for floating applications comes at the price of greatly increased maximum torque and energy production fluctuation.

Axis	ω_o [rad/s]	Max torque [N/m]	Mean torque [N/m]
Fixed	-	6530	3175
Oscillating	0.6	9767 (+49.6%)	3121 (-1.7%)
Oscillating	1.2	13412 (+105.4%)	3311 (+4.3%)

Table 5.3: Maximum and mean torque for fixed and oscillating axis simulations.

5.6 Mean torque convergence

Understanding whether the mean torque has reached convergence or not cannot be done simply by comparing the mean value of a full oscillation with the following one, that is using the same procedure adopted for the fixed axis turbine. In fact there is not an integer number of revolutions in an oscillation, so the mean of two consecutive oscillations is intrinsically varying. However the old procedure could be used considering the period of the overall motion, as made up of a combination of rotation and oscillation. Calling the oscillating turbine period t_g, the revolution period t_r and the oscillation period t_o we have

$$t_t \;=\; Nt_r \;=\; Mt_o\,, \tag{5.9}$$

where N and M are two mutually prime natural number which represent respectively the number of rotation and oscillation in a global period, thus the necessary condition for the turbine motion to be periodic is that the ratio t_r/t_o is a rational number. If it looks like the problem is solved consider that for every rational number there is an infinity of irrationals arbitrarily close to it, which means that the slightest change in t_r or t_o can lead to periodicity or not. To understand the practical effect of this consider what happens to N and M as ω_r is given more digits given $\omega_o = 0.6\ rad/s$ (table 5.4).

ω_r	4	4.1	4.05	4.052	4.0527	...
N	20	41	27	1013	13509	...
M	3	6	4	150	2000	...

Table 5.4: The effect of the rotational angular speed roundoff on N and M.

Since trying to define the torque period creates too many problems a different approach was followed for the purpose of evaluating the mean torque convergence, that is using a moving mean:

$$\overline{T}_{\Delta t}(t) \;=\; \frac{1}{\Delta t}\int_t^{t+\Delta t} T(\tau)d\tau,\,. \tag{5.10}$$

In order to filter the two characteristic periods of the turbine motion a double moving mean was used:

$$\overline{T}_{t_r,t_o} = \frac{1}{t_r t_o} \int_{t}^{t+t_o} \int_{\tau}^{\tau+t_r} T(\tilde{\tau}) d\tilde{\tau} d\tau \,. \tag{5.11}$$

Even though we can clearly see the decreasing tendency and the flattening of the double mean (figure 5-9) the curve is still not smooth enough to judge its slope. To cope with the problem the last part of the function was approximated with a line through a regression, using a number of points which fit an oscillation period. For both oscillation frequencies the slope of the regression line is less than 0.4%, so the mean torque is deemed to be converged.

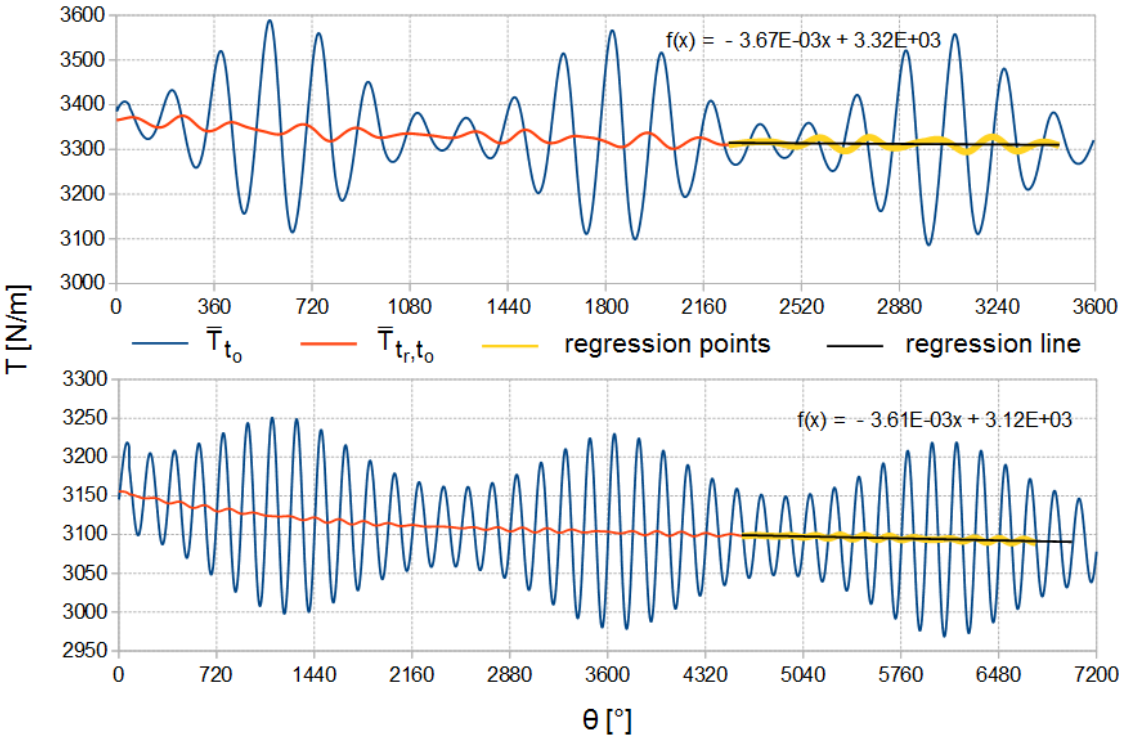

Figure 5-9: Torque moving means for $\omega_o = 1.2\ rad/s$ (up) and $\omega_o = 0.6\ rad/s$ (down).

Chapter 6

Theorical analysis

CFD is a valuable instrument for analysing the aerodynamics of a floating wind turbine, though it is all but a fast mean to obtain results. To overcome this issue a different, simpler approach needs to be developed, and this is what will be shown in the following chapter. First the general idea is explained, than the method is refined step by step.

6.1 General idea

The point of the method is to develop a theory to predict both the instant torque of the oscillating and the fixed turbine. Their ratio is then used to correct the torque of the fixed turbine T_f, known by experimental measures or CFD analysis:

$$T_o \; = T_f \; \frac{T_o^{th}}{T_f^{th}} \; = \; T_f \; C_{th} \, ,$$

where "o" stands for "oscillating", "f" for "fixed", and "th" stands for "theorical", predicted using some kind of model. C_{th} instead is the corrective function representing the ratio between T_o and T_f. To make it clear using an example, we may use a BEM model to predict both T_o^{th} and T_f^{th}, then use their ratio as a corrective function for a turbine whose torque has been experimentally measured. Any theorical prediction is fine though, even a not very accurate one as long as the ratio T_o/T_f is well represented.

This work in particular focused on developing a model which privileges simplicity and rapidity, so a blade element model was used.

6.2 Aerodynamical torque model

The aerodynamical force on the blades generating torque is conventionally split into two components: lift, acting perpendicular to the direction of flow, and drag, acting in the same direction. The torque these two forces create is opposite, lift making the turbine spin while drag trying to stop it. The profiles used for blades or wings have a high lift to drag ratio, so this leads to the first assumption of the model:

Assumption 1. *The drag force can be neglected.*

This hypothesis fails in those cases where drag becomes the predominant force, that is when stall happens and when the angle of attack is zero.
For airfoils in stationary conditions the lift force can be calculated using dimentionless force coefficients:

$$L \;=\; C_L \,\frac{1}{2}\,\rho\; c\; l\; W^2\,, \tag{6.1}$$

where ρ is density, c is the chord, l is the length of the wing and W is the relative flow speed. In a VAWT the flow over the blade is intrinsically unsteady, so the lift coefficient C_L should take into account the dynamic effects due to rotation, first of all the dynamic stall and flow curvature effect (paragraph 2.1). Predicting these phenomena can be hard and it is out of the scope of this model to reach such a precision, so:

Assumption 2. *Dynamic flow effects on lift can be neglected.*

This means that stationary lift coefficient for straight flow are going to be used to calculate lift. Moreover, this assumption regards rotation as well as oscillation; none of the dynamic effect they cause are taken into account in this model. Even though such an hypothesis may sound too strong, it would be certainly acceptable in the

case of no dynamic stall and for a turbine pitching with amplitude and speed small enough.

After assumption 2 the parameters affecting the lift coefficient are just three: the shape of the blade, the angles of attack and the Reynolds number. To simplify the picture even more another assumption is made:

Assumption 3. *The lift coefficient can be calculated using Glauert's thin airfoil theory.*

The theory states that for any symmetrical airfoil

$$C_L \;=\; 2\pi \sin\alpha\,, \tag{6.2}$$

where α is the angle of attack, making the lift coefficient dependent only on this parameter. The assumption made is valid only for a lifting airfoil, so as soon as stall begins to happen the hypothesis falls short of significance. Also, no lift loss caused by finite length blades are taken into account, nor any three dimensional effect due to non-straight blades. Moreover if flow curvature was considered the profile would behave as if it had some camber, which would require to modify the formula.

All the assumptions made so far certainly limit the range of applicability of the model, but make lift to be calculated with a really simple formula:

$$L \;=\; \pi\ \rho\ c\ l\ W^2\ \sin\alpha\,. \tag{6.3}$$

It is now important to understand how torque and lift are connected. According to the cross-flow principle mentioned in Jones [24] and followed by Bianchini [9] and Mertens [29], the lift force acting on a wing in skew does not depend on the spanwise component of the flow. Having lift itself no spanwise component, calculating torque is a matter of simple trigonometry (figure 6-1):

$$T \;=\; L\ r \sin\alpha \;=\; \pi\ \rho\ c\ l\ r\ W^2\ \sin^2\alpha\,, \tag{6.4}$$

where r is the radius of the turbine, the distance from the axis to the blade.

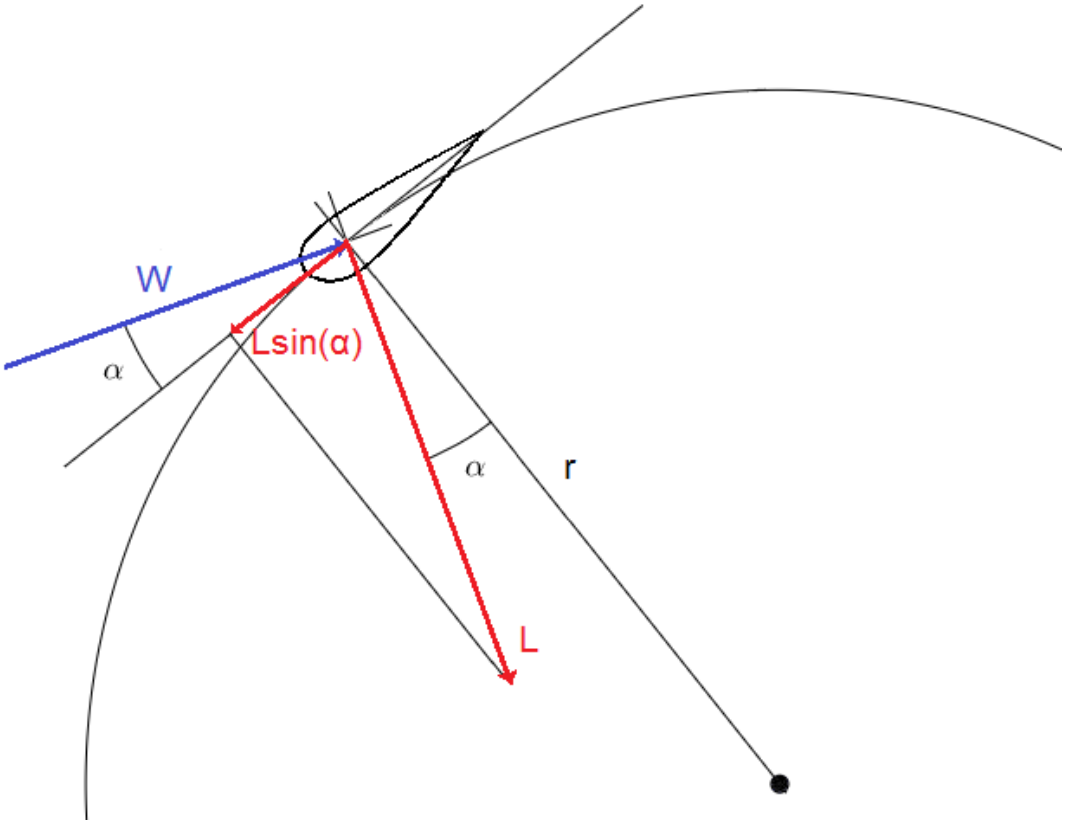

Figure 6-1: Lift component generating torque.

According to equation (6.4)

$$T \propto W^2 \sin^2 \alpha \,, \tag{6.5}$$

which shows that the most important flow parameters affecting the torque are the relative wind speed seen by the blade and the angle of attack. Understanding the difference between them for an oscillating and fixed turbine will lead to the corrective functions we are looking for.

6.3 Relative wind speed and angle of attack

The relative wind velocity $\boldsymbol{W}$ depends on both the absolute wind velocity nearby the blade and the velocity of the blade itself:

$$\boldsymbol{W} \;=\; \boldsymbol{U}_{wind} \;-\; \boldsymbol{U}_{blade}\,. \tag{6.6}$$

In the finest BEM models such as double-multiple streamtube ones, $\boldsymbol{U}_{wind}$ is a function of the position of the blade, obtained by solving iteratively momentum equations for a set of discrete blade positions. Such a precision comes with a certain computational cost, moreover there is no trace in literature of BEM models for oscillating VAWTs . For this reason and for the sake of simplicity the following assumption is made:

Assumption 4. *The absolute wind velocity across the whole rotor is equal to the freestream velocity.*

Following this hypothesis it is possible to obtain the relative wind speed for an oscillating turbine, in a reference system integral to the blade-element having its axes in the tangential, radial and axial direction (figure 6-2):

$$\boldsymbol{W}_o \;=\; \begin{pmatrix} W_t \\ W_r \\ W_a \end{pmatrix} \;=\; \begin{pmatrix} (U_\infty \cos\beta - \dot{\beta} h)\cos\theta + \dot{\theta} r \\ (U_\infty \cos\beta - \dot{\beta} h)\sin\theta \\ U_\infty \sin\beta - \dot{\beta} r \sin\theta \end{pmatrix}, \tag{6.7}$$

where θ is the rotation angle, β the oscillation angle, r is the radius of the section of the turbine perpendicular to the axis, and h its distance from the oscillation axis (figure 6-2). For full demonstration see appendix B. The relative wind velocity for a fixed turbine can be easily derived from equation (6.7) introducing $\beta = 0$ and $\dot{\beta} = 0$:

$$\boldsymbol{W}_f \;=\; \begin{pmatrix} U_\infty \cos\theta + \dot{\theta} r \\ U_\infty \sin\theta \\ 0 \end{pmatrix}, \tag{6.8}$$

According to the cross-flow principle the components of $\boldsymbol{W}$ which generate lift are the ones perpendicular to the spanwise direction. Since this would require to take into account both the axis inclination and the geometry of the curved blades, a simpler version of the principle is adopted:

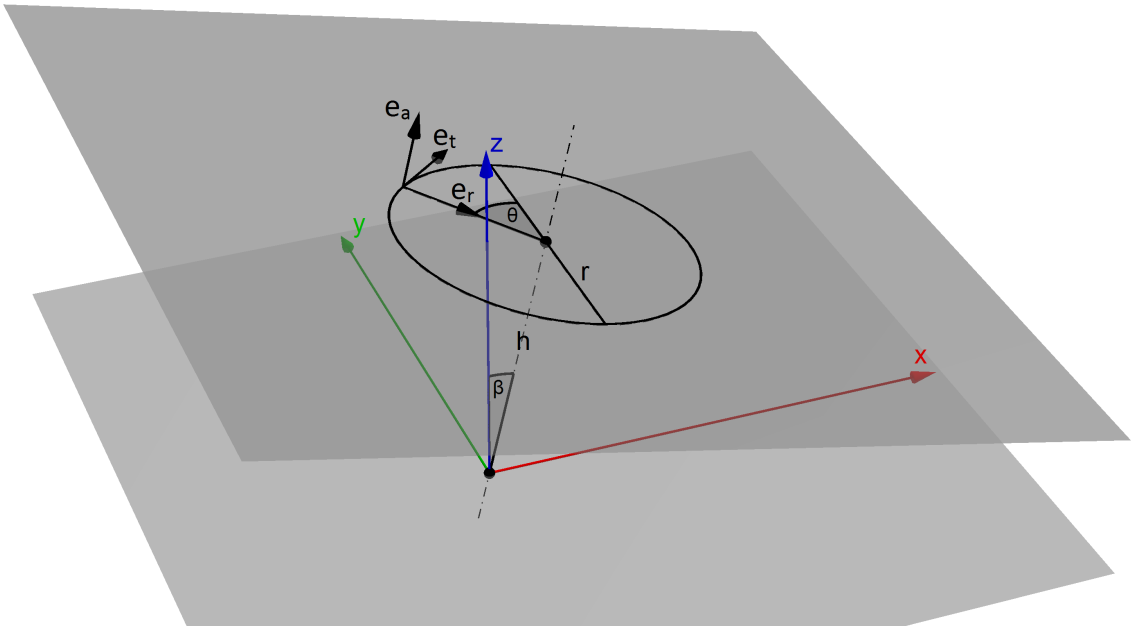

Figure 6-2: Reference system for the relative wind velocity.

Assumption 5. *Lift depends only on the components of the flow perpendicular to the axis of rotation.*

For a turbine with straight blades this is equivalent to the cross-flow principle, whereas for a Darrieus rotor it means that the blades inclination is not considered.

Thanks to assumption 5 the relative wind speed and the angle of attack can be easily expressed, both for the oscillating and fixed turbine:

$$W = |\boldsymbol{W}| = \sqrt{W_t^2 + W_r^2} \tag{6.9}$$

$$\tan\alpha = \frac{W_r}{W_t}\,. \tag{6.10}$$

Finally using equations (6.7 - 6.10):

$$\frac{W_f}{U_\infty} = \sqrt{1+\lambda^2+2\lambda\cos\theta} \qquad \frac{W_o}{U_\infty} = (1-\mu)\sqrt{1+\lambda_o^2+2\lambda_o\cos\theta}\,, \tag{6.11}$$

$$\tan\alpha_f = \frac{\sin\theta}{\lambda+\cos\theta} \qquad \tan\alpha_o = \frac{\sin\theta}{\lambda_o+\cos\theta}\,. \tag{6.12}$$

The time-dependent parameter

$$\mu(t) = \frac{\dot{\beta}(t)h}{U_\infty} \tag{6.13}$$

represents the ratio between the instant oscillation speed of a point on the axis of the turbine and the freestream speed, so from now on it will be referred as *oscillation speed ratio* or OSR. The quantity

$$\lambda_o(t) = \frac{\lambda}{1-\mu(t)} \tag{6.14}$$

instead is an equivalent tip speed ratio for the oscillating turbine.

The angle of attack and the relative wind speed were plotted for $\beta_{max} = 10°$ and $\omega = 0.6\ rad/s$ in order to show the effect of oscillation on these two parameters (figures 6-3 and 6-4).

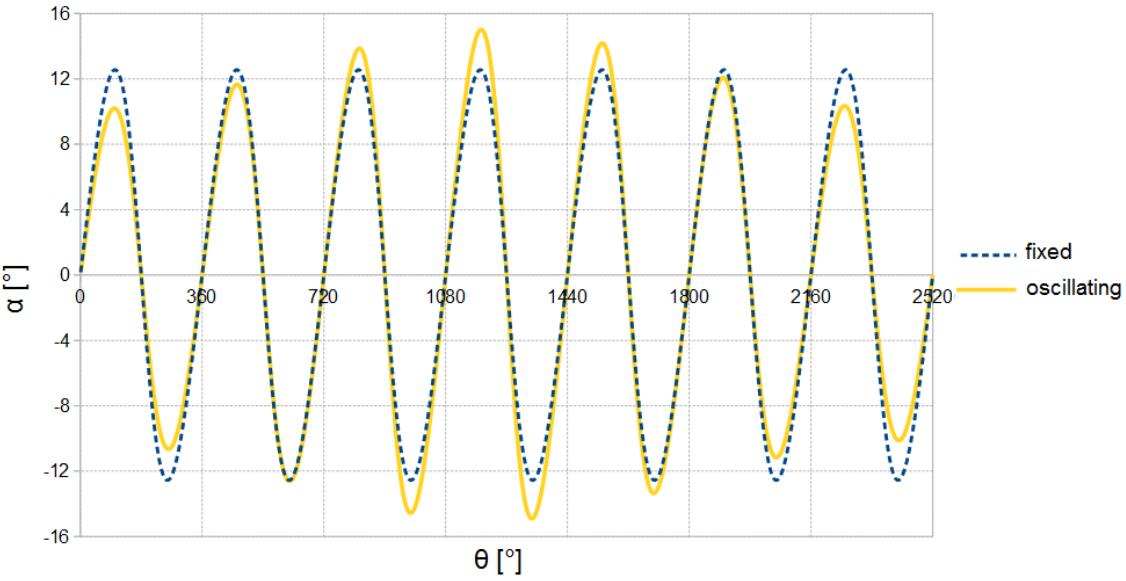

Figure 6-3: A comparison between the angle of attack of a fixed and an oscillating turbine.

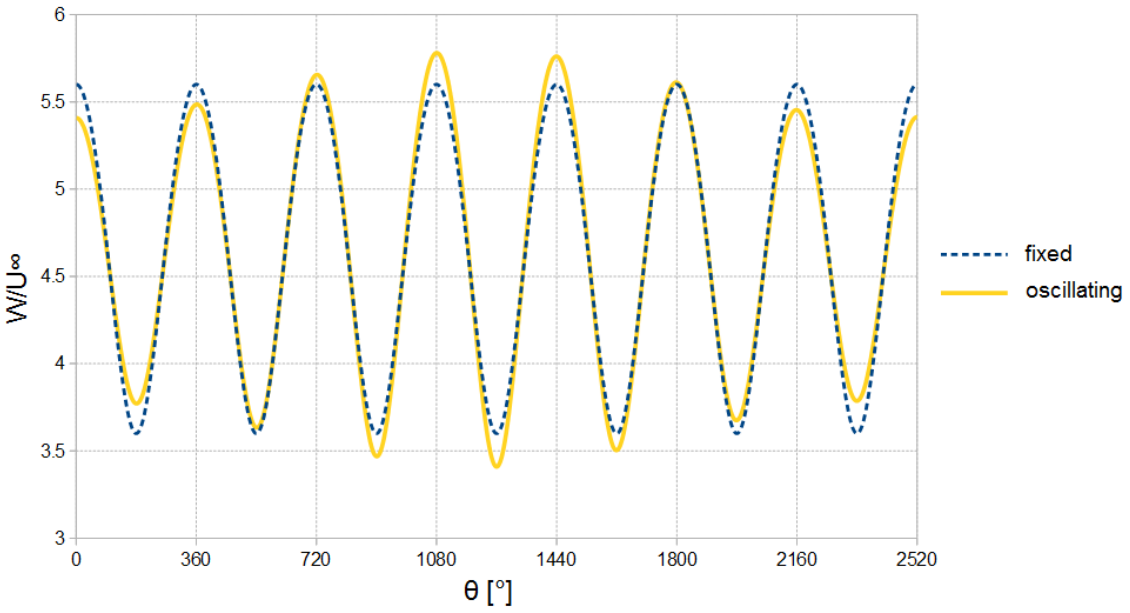

Figure 6-4: A comparison between the relative wind speed of a fixed and an oscillating turbine.

6.4 Relative wind speed correction

Relation (6.5) shows that torque is proportional to the square of the relative wind speed, thus the corrective function taking into account this quantity alone is

$$C_W = \left(\frac{W_o}{W_f}\right)^2 = \frac{1+\lambda_o^2+2\lambda_o\cos\theta}{1+\lambda^2+2\lambda\cos\theta}(1-\mu)^2\,. \tag{6.15}$$

The correction written is based on the torque of a single blade element, so the equatorial section of the turbine is chosen as representative for the whole turbine. To obtain the overall torque C_W have to be applied to the one of the single blades:

$$T_o = T_f^{b1}C_W(\theta) + T_f^{b2}C_W(\theta \pm 180°) \tag{6.16}$$

It is clear that the change in the relative wind speed cannot explain the different behaviour of an oscillating VAWT (figure 6.4).

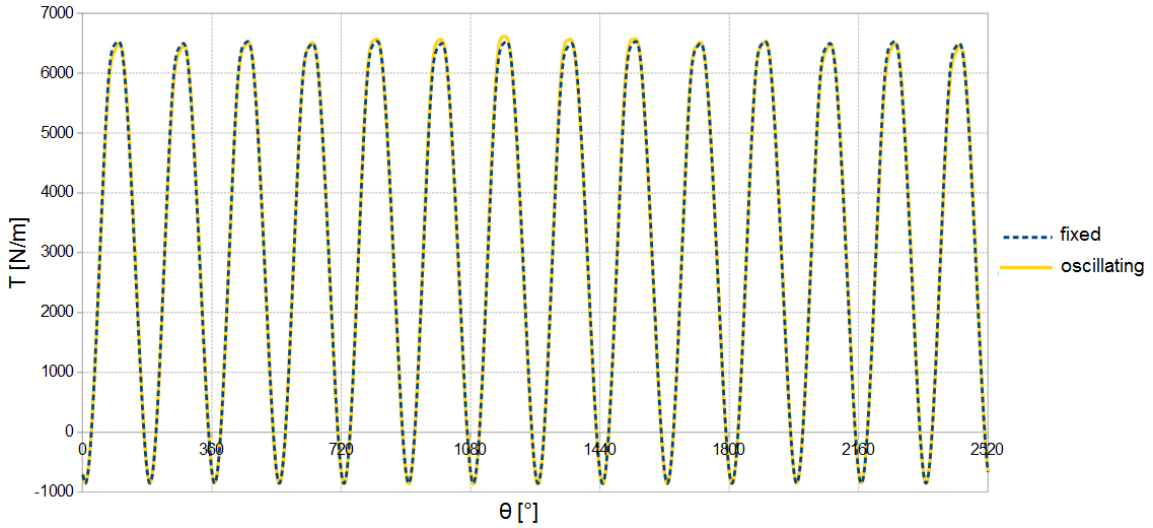

Figure 6-5: The effect of the correction based on the relative wind speed for $\beta_{max} = 10°$ and $\omega = 0.6\ rad/s$.

6.5 Angle of attack correction

Being torque proportional to $\sin^2 \alpha$ the corrective function relative to this parameter is

$$C_\alpha \;=\; \left(\frac{\sin \alpha_o}{\sin \alpha_f}\right)^2 .$$

Applying the trigonometric relation

$$\sin^2 x \;=\; \frac{\tan^2 x}{1+\tan^2 x}$$

to equations (6.12) we obtain

$$\sin^2 \alpha_f \;=\; \frac{\sin^2 \theta}{1+\lambda^2+2\lambda\cos\theta} \qquad \sin^2 \alpha_0 \;=\; \frac{\sin^2 \theta}{1+\lambda_o^2+2\lambda_o\cos\theta}\,, \tag{6.17}$$

so the corrective function becomes

$$C_\alpha \;=\; \frac{1+\lambda^2+2\lambda\cos\theta}{1+\lambda_o^2+2\lambda_o\cos\theta}\,. \tag{6.18}$$

Again the equatorial section is chosen to calculate the corrective function for the whole turbine. As before C_α is applied to the single blades:

$$T_o \;=\; T_f^{b1} C_\alpha(\theta) \;+\; T_f^{b2} C_\alpha(\theta \pm 180°)\,. \tag{6.19}$$

This correction shows with no doubt that the change in the angles of attack is the key factor which influences the torque of an oscillating turbine (figure 6-6).

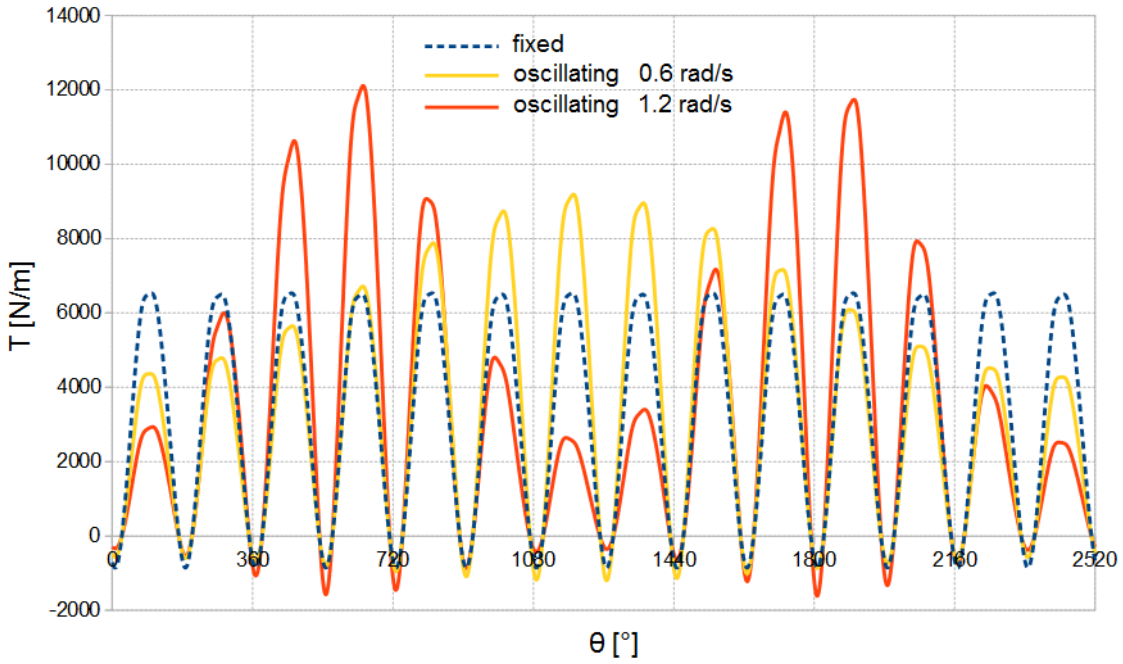

Figure 6-6: Torque prediction based on the angle of attack correction for $\beta_{max} = 10°$ and two different oscillation frequencies.

6.6 Combined correction

Applying the correction based on the angle of attack and the relative wind speed together, a really simple corrective function is obtained:

$$C_c \;=\; \left(\frac{W_o}{W_f}\frac{\sin\alpha_o}{\sin\alpha_f}\right)^2 \;=\; (1-\mu)^2 \;=\; \left(1-\frac{\dot{\beta}h}{U_\infty}\right)^2 . \tag{6.20}$$

Moreover the correction does not depend on θ, so it can be applied either to the blade or to the overall torque:

$$T_o^b = T_f^b C_c \qquad\qquad T_o = T_f C_c \tag{6.21}$$

Considering that the blade torque is difficult to be measured experimentally, this result extends considerably the applicability of the model.

As expected the final result does not differ much from the angle of attack correction alone, in fact ripple, peak torque increase and general oscillating behaviour are correctly represented, at least qualitatively (figure 6-7). In particular all these effects become more evident as the oscillation grows in frequency and amplitude.

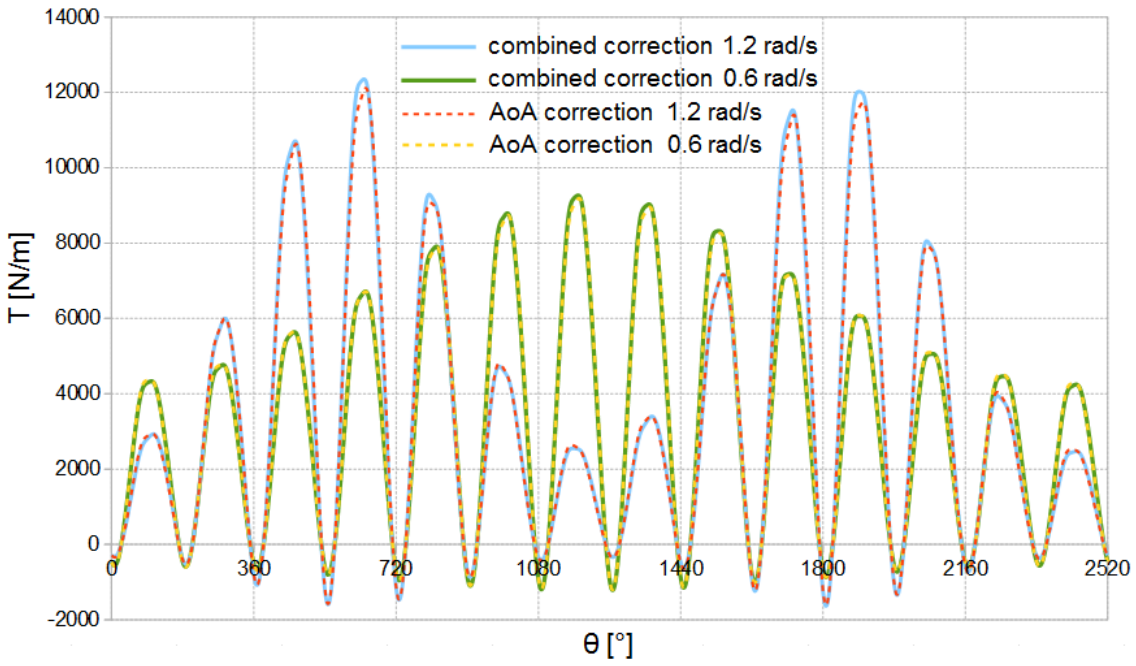

Figure 6-7: A comparison between the angle of attack and the combined correction for $\beta_{max} = 10°$ and two different oscillation frequency.

6.7 Freestream velocity correction

Looking at the torque of the oscillating turbine, it is clear that when the turbine is pitching in the opposite direction of the wind an increase is seen, and that the opposite

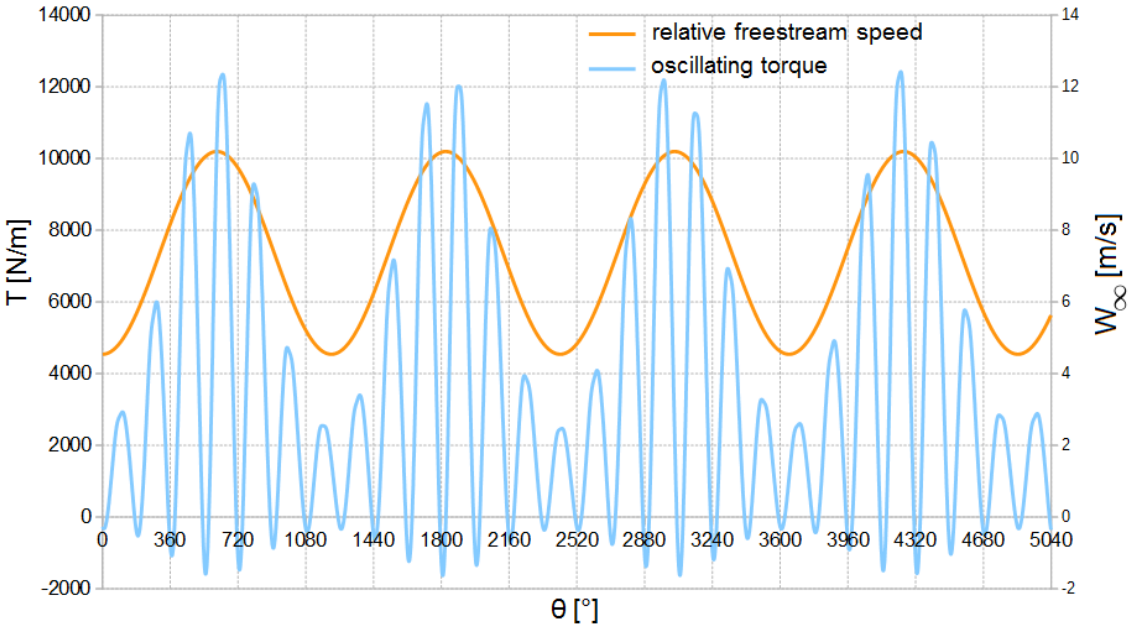

Figure 6-8: Correlation between the predicted torque of the oscillating turbine and the relative freestream speed.

happens when pitching is in the same direction. In order to explain this phenomenon in an intuitive way, let us consider a fixed axis turbine and a wind whose speed is changing with time:

$$W_\infty(t) \;=\; U_\infty - U_o(t)\,, \tag{6.22}$$

Such a wind would cause the following relative wind speed on the blade:

$$\boldsymbol{W}_o \;=\; \begin{pmatrix} (U_\infty \cos\beta - U_o(t))\cos\theta + \dot{\theta} r \\ (U_\infty \cos\beta - U_o(t))\sin\theta \\ 0 \end{pmatrix}. \tag{6.23}$$

Let $U_o(t) = \dot{\beta} h$ and thanks to assumption 5 this relative wind speed will lead to the same corrective functions developed so far, which means that *an oscillating turbine can be seen as a fixed one in a oscillating wind*. From this point of view it is possible to interpret C_c under a new light:

$$C_\infty \;=\; C_c \;=\; \left(\frac{W_\infty}{U_\infty}\right)^2. \tag{6.24}$$

Going backwards, this means that the torque is proportional to the square of the relative freestream speed.

6.8 Multiple sections correction

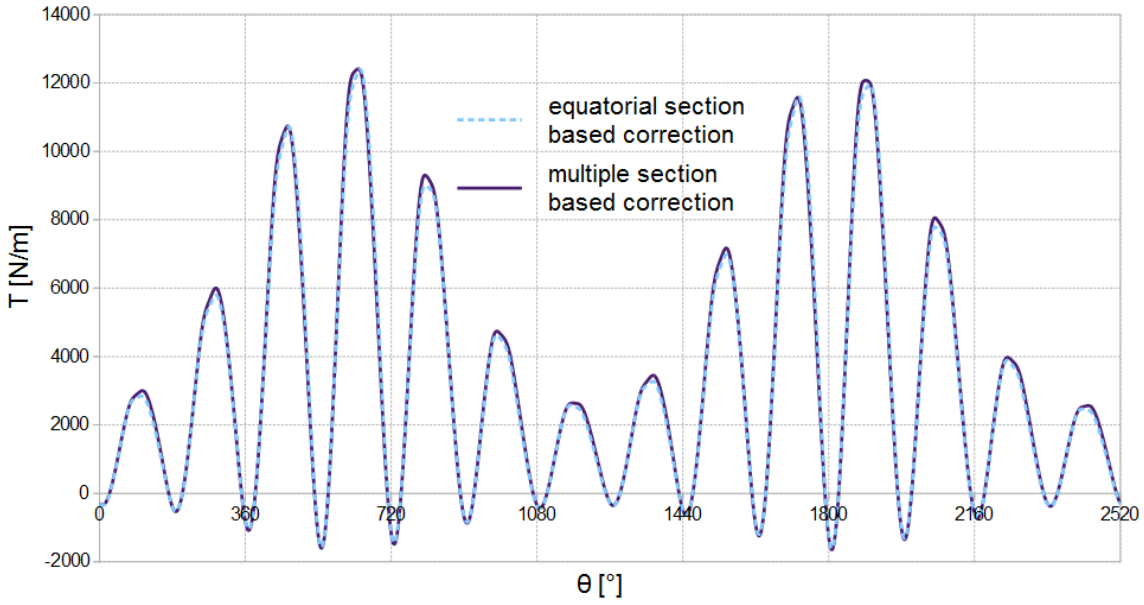

Figure 6-9: Predicted torque based on the multiple section correction versus the equatorial section one for $\beta_{max} = 10°$ and $\omega = 1.2\ rad/s$.

All the corrective functions seen so far are based on the equatorial section only, but by the means of an integration it is possible to consider all the sections of the turbine. Calling dT the infinitesimal torque of a small disk of the turbine, the correction is

$$C_m = \frac{\int dT_o}{\int dT_f}.$$

After some calculations that can be found in appendix C:

$$C_m = \frac{\int_{h_{min}}^{h_{max}} C_\infty\, r\, \sqrt{1+\left(\frac{dr}{dh}\right)^2}\, dh}{\int_{h_{min}}^{h_{max}} r\, \sqrt{1+\left(\frac{dr}{dh}\right)^2}\, dh}, \tag{6.25}$$

so the multiple sections correction is a weighted mean of the local correction using

$r\sqrt{1+\left(\frac{dr}{dh}\right)^2}$ as a weight.

For the Darrieus-type Sandia turbine an analytical solution for equation (6.25) can be found, though it is tedious to obtain and would add no further meaning to the corrective function. For this reason C_m was calculated through numerical integration using 31 uniformly spaced values of h.

The energies spent in trying to increase the precision of the model are not worth the results (figure 6-9), as the torque change is so little it can be hardly observed.

6.9 Comparison against CFD data

In order to assess the validity of the model proposed its predictions were compared against the previous CFD analysis. A good correlation between the results will not just corroborate the model, but will also strengthen the computational analysis which lacks of validation against experimental data. The only correction chosen for the comparison is the combined one (equation (6.20)), being this complete and simple at the same time. Section 6.8 already showed that complicating the model does not improve the predictions.

In order to quantify the matching a relative error was defined:

$$e \;=\; \frac{\left|T_o^{th} - T_o^{CFD}\right|}{\max T_f^{CFD}}\,, \tag{6.26}$$

where $\left|T_o^{th} - T_o^{CFD}\right|$ represents the absolute error, divided by the maximum torque of the fixed turbine. The theorical model was able to reproduce the behaviour of the overall torque with satisfactory accuracy (table 6.1, figure 6-10). As we could expect

$\omega_o\ [rad/s]$	mean e [%]	max e [%]
0.6	5.3	13.8
1.2	9.1	29.0

Table 6.1: Mean and maximum relative error of the model for the overall torque.

precision decreases for the higher oscillation frequency, as the hypotheses which the model is based on become less valid as this parameter grows.

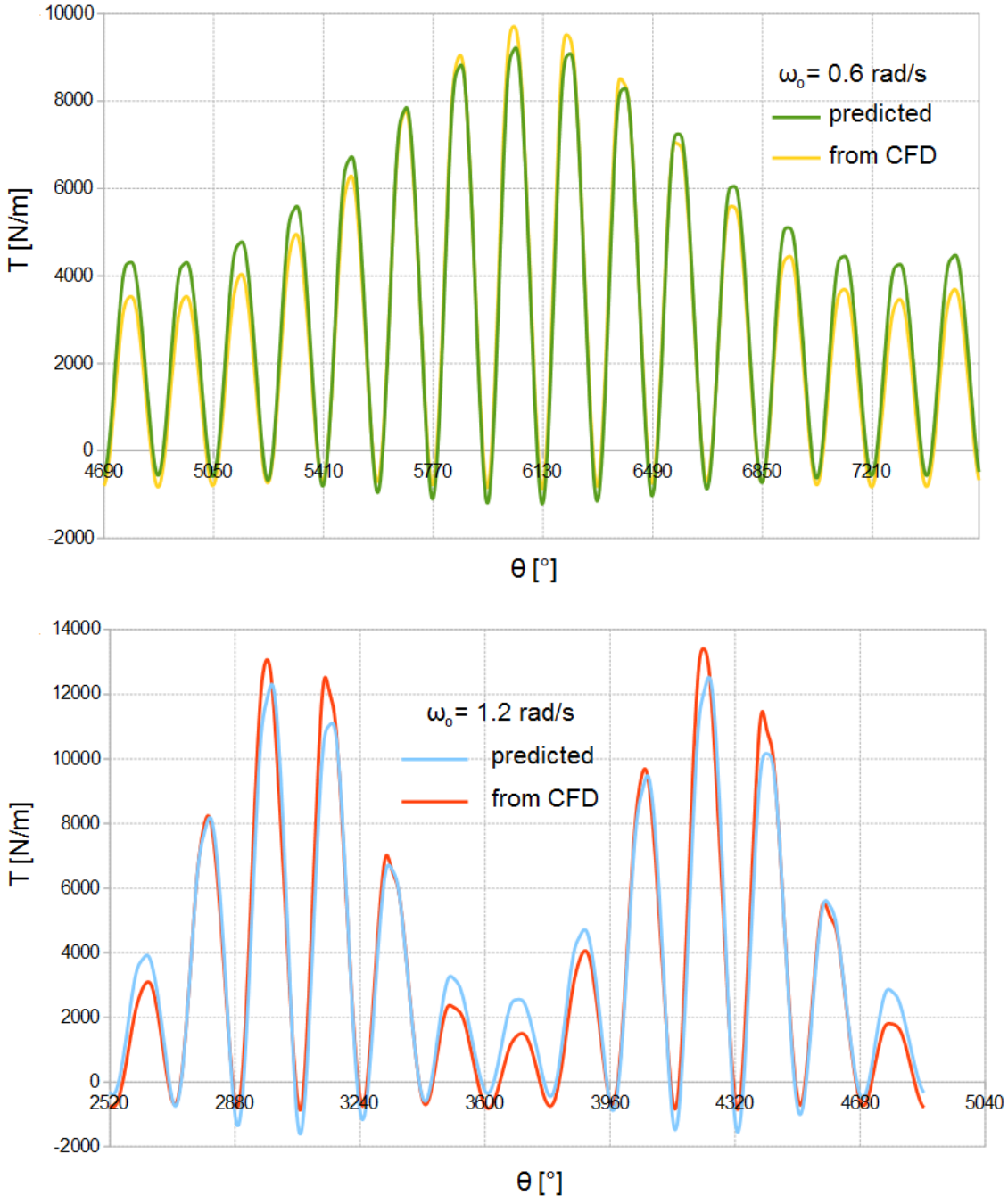

Figure 6-10: Comparison between the predicted overall torque and the one obtained from the CFD analysis.

Particularly interesting are the differences between the two curves of the blade torque (figure 6-11), since these details can reveal the weaknesses of the model. The most important discrepancies are three:

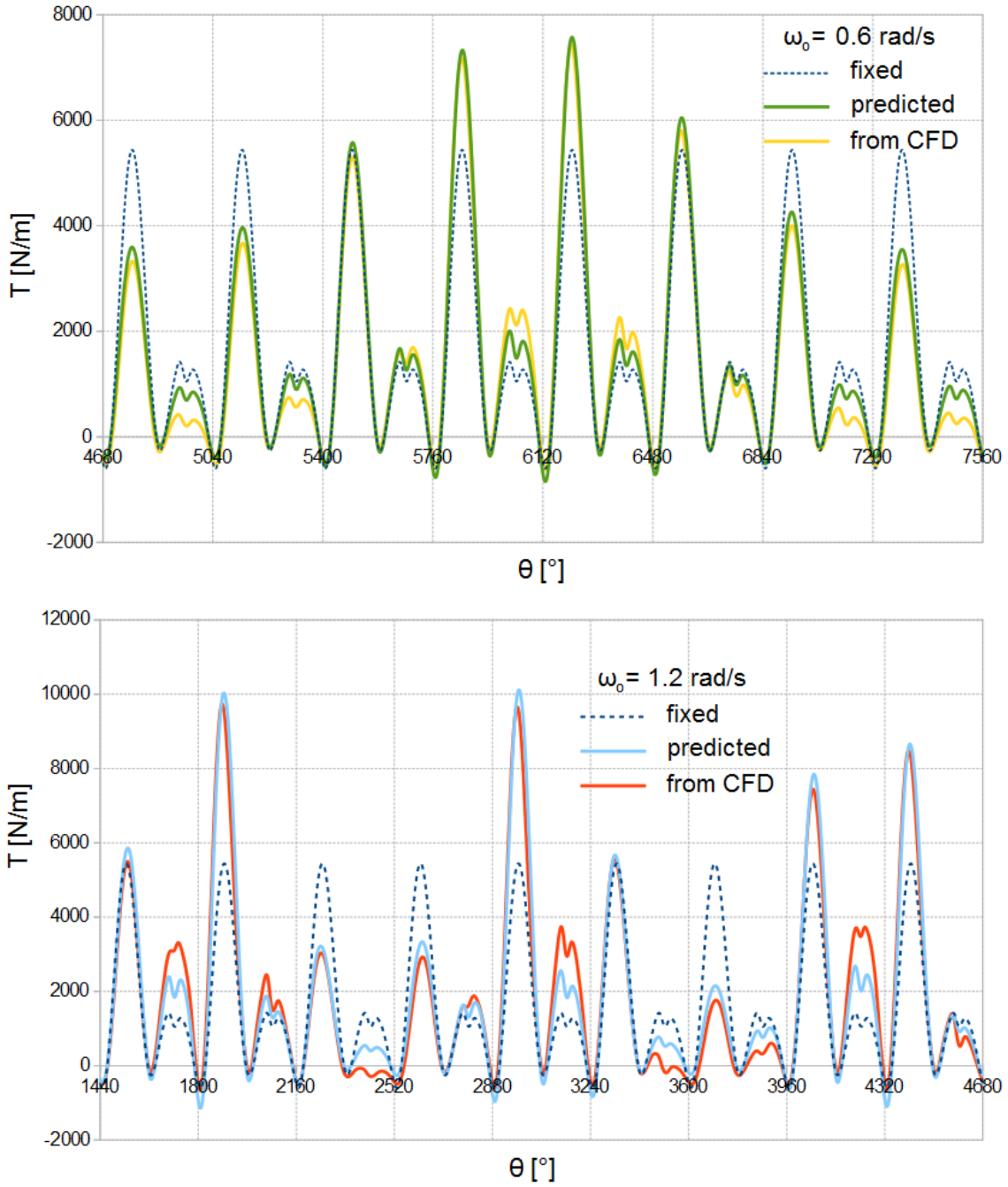

Figure 6-11: Comparison between the predicted blade torque and the one obtained from the CFD analysis.

- the torque peak in the upwind half of the rotor is overestimated,
- the negative peak is alternatively over or underestimated,
- the torque in the downwind half of the rotor is alternatively over or underesti-

mated.

6.10 Discussion

Notwithstanding all the assumptions made and the exclusion of momentum equations, the predicted model could reproduce with satisfactory accuracy the behaviour of an oscillating Darrieus-type turbine.

The TSR of 4.6, which corresponds to the one of maximum power coefficient, was fundamental in this, as in this condition no stall is observed. Therefore dynamic effects seem to be less relevant and C_L seems to be well represented by thin airfoil theory. In order to broaden the applicability of the model to lower TSRs dynamic stall should to be included.

Introducing drag in the model could help reaching a higher precision, in particular around the negative torque peak where the low angle of attack make it the dominating force. The fluctuating error around the negative torque peak pointed out in paragraph 6.9 should be solved, as drag is expected to be less affected by oscillation making the corrective function closer to 1. The reason why this is is expected to happen, is that drag depends mainly on the relative wind speed, which in paragraph 6.4 was found to be slightly changed by oscillation. Precision around the positive peak may also be increased; for finite length wings in fact a certain amount of drag is induced by lift, which according to the lifting line theory is

$$C_{D_i} \propto C_L^2 . \tag{6.27}$$

Therefore as the lift force grows drag becomes more and more relevant, which makes the peak torque a critical part for our lift-dependant model. In any case, without further analysis is not possible to conclude whether considering drag would solve this problem or not.

At last, let us discuss about the most important assumption of the model: the exclusion of the momentum equations. The most important consequence of this is

that the absolute wind speed over the rotor is uniform, but let us assume that we have a model capable of considering different wind speeds depending on the position of the blade. To simplify the picture consider

$$\boldsymbol{U}_{wind} \;=\; (1-a)\,\boldsymbol{U}_{\infty}\,, \tag{6.28}$$

where a is the induction factor depending on the position of the blade. Such a formulation would lead to the following corrective function for the single blade:

$$C_c \;=\; \left(1-\frac{\dot{\beta}h}{(1-a_o)U_{\infty}}\right)^2\left(\frac{1-a_o}{1-a_f}\right)^2\,. \tag{6.29}$$

Looking at how well the present model performs in the upwind half of the rotor (figure 6-11) we can say that the new formula (6.29) should be similar to the old (6.20) in this region. This is possible if the induction factors a_o and a_f have similar values and if a_o is close to 0, which under a physical point of view means that *oscillation slightly affects the induction factors* and that *induction effect is low.*

Completely different is the situation in the downwind half of the rotor, where the present model alternatively over and underestimates the torque. A mechanism which is deemed to explain reason why it happens will follow shortly. Imagine the turbine as divided in two halves representing the upwind and downwind part of the rotor, extracting energy from the wind sequentially (figure 6-12). The upwind half would slow down the wind, which transported downstream would reach the second half after while. In an oscillating VAWT the energy extracted upwind has an harmonic with a period corresponding to oscillation, so according to the picture drew the stream reaching the blade passing downwind should have the same harmonic too, delayed by a certain time due to convection. Looking at figure 6-11 we realize that the downwind torque and so wind speed are higher than expected right after the zone of minimum peak torque; the opposite is observed after the maximum peak is reached, where the less energy available make the real downwind torque smaller than the value predicted. Moreover, it is clear especially from the lower oscillation frequency (figure 6-11) that

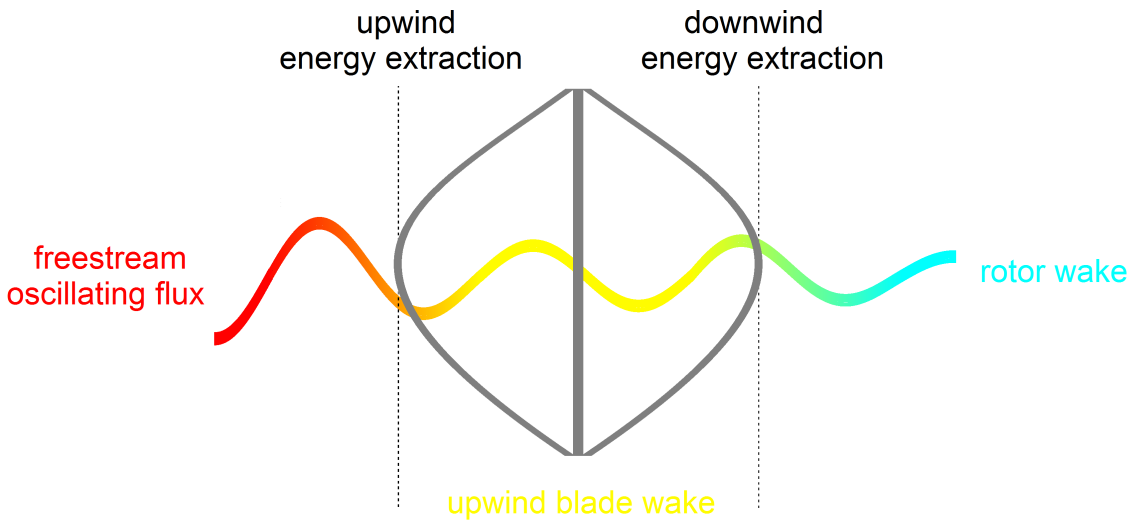

Figure 6-12: The mechanism of energy extraction in a periodically oscillating wind turbine

the difference between the predicted downwind torque and the real one have some kind of a sinusoidal behaviour, a fact well explained by the mechanism proposed.

Accordingly to what has been said so far, a BEM model for oscillating VAWTs should rethink how the induction factors are defined, in particular for the downwind blade positions which are dynamically affected by the wake left by the the blade passing upwind.

Chapter 7

Conclusions

7.1 Overview

For the development of offshore wind technology it is fundamental to improve our understanding of the aerodynamic forces acting on the blades of floating turbines. The aerodynamic performance in fact has a strong influence on many design aspects of these machines, such as energetic productivity, mechanical-structural resistance, stability and electricity production.

At the time of writing no computational or experimental studies investigate the topic, nor analytical models tailored for floating applications are present, so this work tries to fill this gap.

The aerodynamic performance of a periodically oscillating VAWT was then studied through numerical and theorical means, in particular to highlight the effect on the torque of the rotor pitching motion .

7.2 Computational analysis

An unsteady 3D CFD model was developed for the 17m SANDIA Darrieus-type VAWT, which for the fixed axis case was validated against experimental and other computational data from an independent analysis. The TSRs evaluated are two, one corresponding to the maximum power coefficient and no stall condition, and the other

to stalled condition. The present model reproduces the experimental torque in the former condition with acceptable accuracy, while in the other a significative mismatch is observed. A comparison between the effects of a uniform and a power law wind profile was also performed, showing that they are negligible for this kind of turbine.

The analysis was then extended to a periodically pitching turbine, whose aerodynamics is deeply influenced by the oscillation motion. The torque was found to fluctuate with a frequency equal to the one of oscillation. As intuition suggests, it increases when pitching occurs in the direction opposite to the wind and decreases when the direction is the same. A significative growth of the maximum peak torque is observed, which for the higher oscillation frequency considered is more than double the fixed axis turbine value. The mean torque instead is just slightly affected, negatively for the lower frequency and positively for the higher one.

7.3 Theorical analysis

An analytical model based on the blade element theory was developed to predict the aerodynamic torque of an oscillating turbine. The method consist in applying a corrective function to the torque of the same fixed axis turbine, which has to be known previously from CFD simulations or experiments. Several corrective functions were tested, in order to consider separately the effect on the torque of the angles of attack, of the relative wind speed and of the turbine equatorial section.

The combined correction based on the angles of attack, on the relative wind speed and on the equatorial section only proved to be simple yet accurate.

The model also establishes a better understanding of the most influential factors for the torque. First of all the angle of attack change due to the oscillation motion have the greater effect, while the influence of the relative wind speed is very limited. Secondly what happens to the equatorial section is representative for the whole turbine and finally, analysing the parts in which the model lacks accuracy it was possible to understand the mechanisms which affect the torque in the downwind part of the rotor. Considering the velocity induced by oscillation is not enough in fact,

as the wake generated by the upwind blade and its convection downstream play an important role on the local wind velocity.

7.4 The Darrieus turbine for floating applications

The results achieved let us draw some conclusions on the positive and negative aspects of using Darrieus turbines for floating applications.

A highly desirable characteristic is the fact that the mean torque is just slightly affected by oscillation, so in theory almost the same energetic performance of a fixed axis turbine is expected. This also means that already existing designs for onshore applications could be used for floating ones with no great changes, at least until specific optimized designs are not present.

Such a positive feature is counterbalanced by a sensibly increased torque and ripple, which is already a weakness of VAWTs in general. Greater and highly variable loads add more problems under many points of view, which could drive the cost of this technology higher.

7.5 Suggestions for future work

The analysis carried on in this work is a first step towards a better understanding of the aerodynamics of floating VAWTs, but much more has to be done for the topic.

First of all there are no experiments on the aerodynamics of floating or moving axis wind turbines, so models cannot be validated properly.

Then, the present computational and analytical models were limited to just one degree of freedom so a more complex and realistic motion should be considered, a thing that could be done just by slightly modifying the current approach.

Finally the theorical model is suitable for being implemented inside computer aided engineering tools for coupled analyses, thanks to its simplicity and absolutely low computational resources needed.

Appendix A

FLUENT UDFs code

The three UDFs follow, written to implement the power-law wind profile, the turbine and the interface motion for the dynamic mesh.

```
include "udf.h"
define vang 4.052655 /* rotational angular velocity rad/s */
define beta 0.1745329252 /* amplitude of oscillation rad */
define omega 0.6 /* oscillation frequency rad/s */
define R 13.5 /* radius of oscillation*/
define V 7.369 /* wind speed at equatorial plane */

/* Wind shear profile */
DEFINE_PROFILE(wind_shear, t, i) {
      real x[ND_ND], z;
      face_t f;
      begin_f_loop(f,t) {
           F_CENTROID(x, f, t);
           z=x[2];
           F_PROFILE(f, t, i) = V*pow((z+R)/R,0.1);
      } end_f_loop(f, t)
}
```

```
/* Turbine motion */
DEFINE_CG_MOTION(turbine, dthread, v, w, t, dt) {
      /* Centre of gravity velocity */
      v[0]=beta*omega*R*cos(beta*sin(omega*t))*cos(omega*t);
      v[1]=0;
      v[2]=-beta*omega*R*sin(beta*sin(omega*t))*cos(omega*t);

      /* Angular velocity */
      w[0]=vang*sin(beta*sin(omega*t));
      w[1]=beta*omega*cos(omega*t);
      w[2]=vang*cos(beta*sin(omega*t));
}

/* Interface motion */
DEFINE_CG_MOTION(interface, dthread, v, w, t, dt) {
      /* Centre of gravity velocity */
      v[0]=beta*omega*R*cos(beta*sin(omega*t))*cos(omega*t);
      v[1]=0;
      v[2]=-beta*omega*R*sin(beta*sin(omega*t))*cos(omega*t);

      /* Angular velocity */
      w[0]=0;
      w[1]=0;
      w[2]=0;
}
```

Appendix B

Relative wind speed

In the following lines the formulation of the relative wind speed for a pitching turbine presented in paragraph 6.3 is given. The first step is to sum the absolute wind speed and the speed of the blade together:

$$\boldsymbol{W}_o \;=\; \boldsymbol{U}_{wind} - \boldsymbol{U}_{blade}\,. \tag{B.1}$$

According the assumptions made $\boldsymbol{U}_{wind} = \boldsymbol{U}_\infty$; $\boldsymbol{U}_{blade}$ can be divided into two contributes:

$$\boldsymbol{U}_{blade} \;=\; \boldsymbol{U}_{\dot{\beta}} + \boldsymbol{U}_{\dot{\theta}}\,, \tag{B.2}$$

where $\boldsymbol{U}_{\dot{\beta}}$ is the blade velocity due to oscillation and $\boldsymbol{U}_{\dot{\theta}}$ is the one due to rotation. A cylindrical coordinates reference system integral to the turbine was chosen, so the components will be tangential, radial and axial (figure 6-2).

First let us concentrate on $\boldsymbol{U}_\infty$, dividing it in an axial component and in one perpendicular to the axis (figure B):

$$\boldsymbol{U}_\infty \;=\; \begin{pmatrix} U_\perp \\ U_a \end{pmatrix} \;=\; U_\infty \begin{pmatrix} \cos\beta \\ \sin\beta \end{pmatrix}\,. \tag{B.3}$$

The $U_\perp$ component can now be easily divided into a tangential and a radial component

(figure B):

$$\boldsymbol{U}_\infty \;=\; \begin{pmatrix} U_t \\ U_r \\ U_a \end{pmatrix} \;=\; U_\infty \begin{pmatrix} \cos\beta\cos\theta \\ \cos\beta\sin\theta \\ \sin\beta \end{pmatrix} \tag{B.4}$$

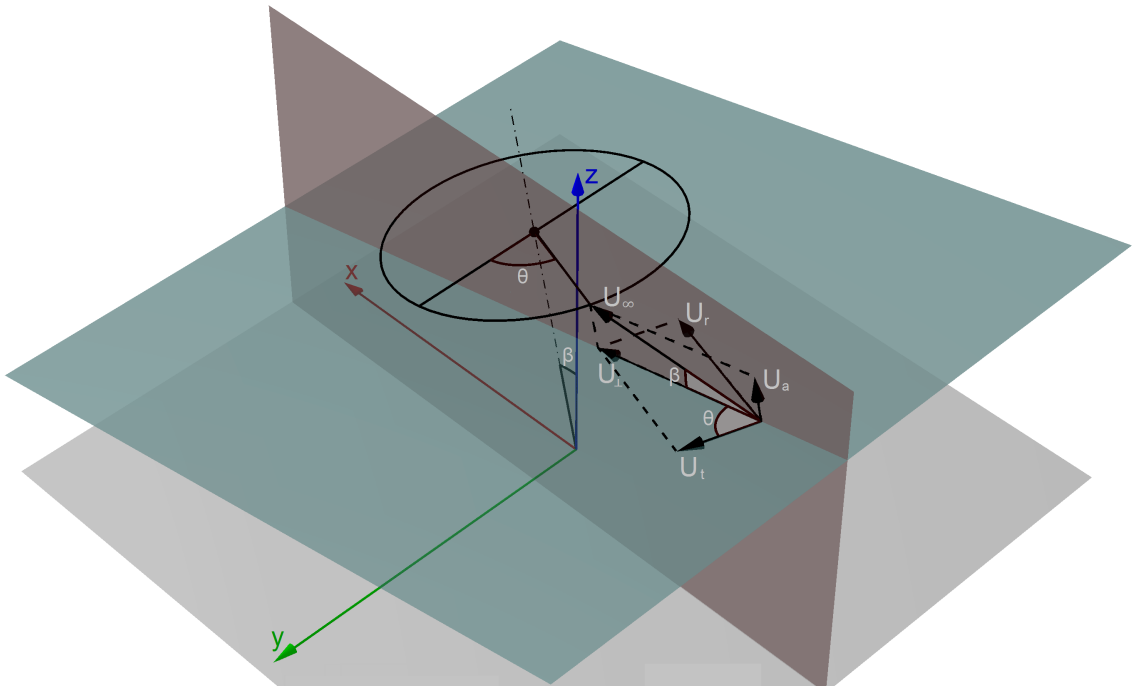

Figure B-1: Freestream velocity decomposition.

The speed caused by oscillation depends on the oscillation angular velocity $\dot{\beta}$ and the distance from the oscillation axis d (figure B-2):

$$U_{\dot{\beta}} \;=\; \dot{\beta}d \;=\; \dot{\beta}\sqrt{h^2 + r^2\sin^2\theta} \tag{B.5}$$

About the direction of $\boldsymbol{U}_{\dot{\beta}}$ we can say that it lays on a plane perpendicular to the axis of oscillation (figure B-2), so we can apply a decomposition similar to what we did with U_∞:

$$\boldsymbol{U}_{\dot{\beta}} \;=\; \begin{pmatrix} U_\perp \\ U_a \end{pmatrix} \;=\; \dot{\beta}d \begin{pmatrix} \cos\xi \\ \sin\xi \end{pmatrix}, \tag{B.6}$$

where the trigonometric functions of ξ are:

$$\cos\xi \;=\; \frac{h}{d} \qquad\qquad \sin\xi \;=\; \frac{r\ sin\theta}{d}\,. \tag{B.7}$$

The $U_\perp$ component can be divided in a tangential and in a radial one like done before:

$$\boldsymbol{U}_{\dot\beta} \;=\; \begin{pmatrix} U_t \\ U_r \\ U_a \end{pmatrix} \;=\; \dot\beta \begin{pmatrix} h\cos\theta \\ h\sin\theta \\ r\sin\theta \end{pmatrix} \tag{B.8}$$

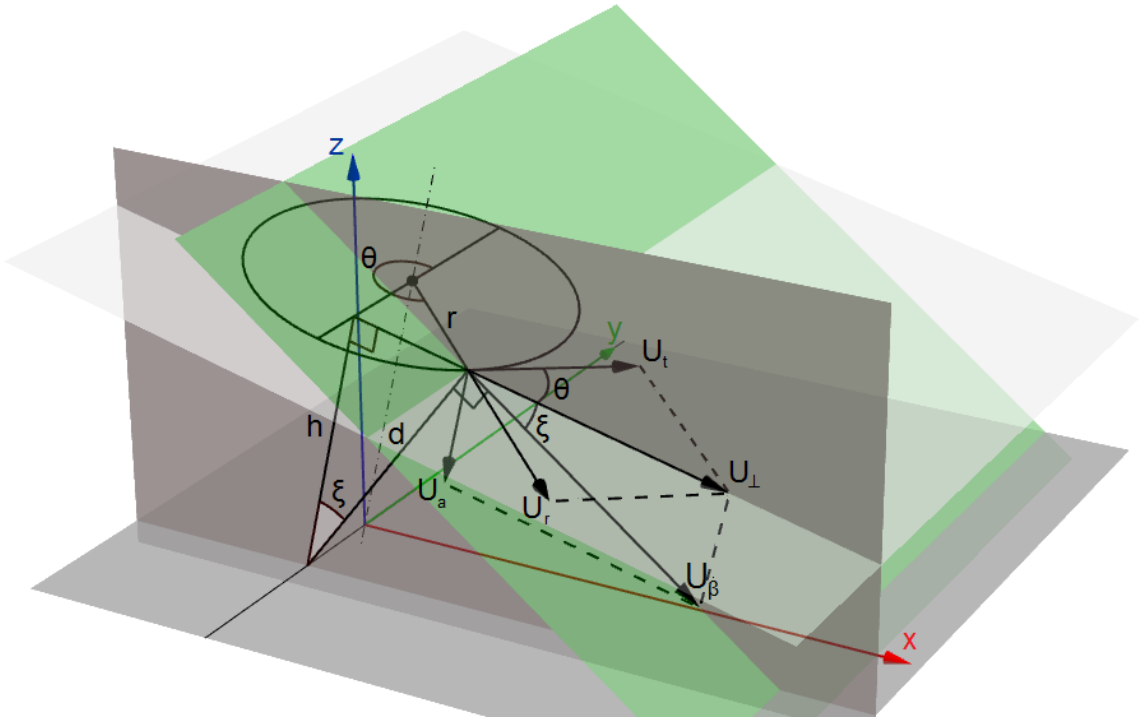

Figure B-2: Velocity due to oscillation decomposition.

$\boldsymbol{U}_{\dot\theta}$ is really easy to write as it only has a tangential component:

$$\boldsymbol{U}_{\dot\theta} \;=\; \begin{pmatrix} -\dot\theta r \\ 0 \\ 0 \end{pmatrix} \tag{B.9}$$

Combining $\boldsymbol{U}_\infty$, $\boldsymbol{U}_{\dot{\beta}}$ and $\boldsymbol{U}_{\dot{\theta}}$ according to equation (B.1) we obtain

$$\boldsymbol{W}_o = \begin{pmatrix} (U_\infty \cos\beta - \dot{\beta}h)\cos\theta + \dot{\theta}r \\ (U_\infty \cos\beta - \dot{\beta}h)\sin\theta \\ U_\infty \sin\beta - \dot{\beta}r\cos\theta \end{pmatrix}. \tag{B.10}$$

Appendix C

Multiple sections correction

The purpose of this part is to obtain the C_m correction seen in paragraph 6.8 using its definition:

$$C_m \;=\; \frac{\int dT_o}{\int dT_f}\,. \tag{C.1}$$

Following equation (6.4) the torque on an infinitesimal section is

$$dT \;=\; \pi\;\rho\;c\;r\;W^2\;\sin^2\alpha\;dl\,, \tag{C.2}$$

Instead of using the local length of the blade as the integration variable, the distance from the oscillation axis h is chosen. Their relation depends on the shape of the turbine through the slope:

$$dl \;=\; dh\,\sqrt{1+\left(\frac{dr}{dh}\right)^2} \tag{C.3}$$

Substitution of equations (C.3) and (C.2) into (C.1) leads to

$$C_m \;=\; \frac{\int dT_o}{\int dT_f} \;=\; \frac{\int W_o^2\;\sin^2\alpha_o\;r\;\sqrt{1+\left(\frac{dr}{dh}\right)^2}\;dh}{\int W_f^2\;\sin^2\alpha_f\;r\;\sqrt{1+\left(\frac{dr}{dh}\right)^2}\;dh}\,. \tag{C.4}$$

Finally the relative wind speeds (equations (6.11)) and the angles of attack (equations (6.17)) are introduced in the expression, so equation (6.25) is achieved:

$$C_m = \frac{\int_{h_{min}}^{h_{max}} C_\infty \, r \, \sqrt{1 + \left(\frac{dr}{dh}\right)^2} \, dh}{\int_{h_{min}}^{h_{max}} r \, \sqrt{1 + \left(\frac{dr}{dh}\right)^2} \, dh} \, . \tag{C.5}$$

Bibliography

[1] A. Mbistrova A. Ho and G. Corbetta. The European offshore wind industry - key trends and statistics 2015. Technical report, European Wind Energy Agency, 02 2016.

[2] R. E. Akins, D. E. Berg, and W. T. Cyrus. *Measurements and calculations of aerodynamic torques for a vertical-axis wind turbine*. Sandia National Laboratories, 1987.

[3] R.E. Akins. *Measurement of Surface Pressures on an Operating Vertical-axis Wind Turbine*. Sandia National Laboratories Albuquerque, NM, USA, 1989.

[4] S. Alberici et al. Subsidies and costs of EU energy. Technical report, Ecofys, 11 2014.

[5] ANSYS In. *Fluent theory guide and UDF manual*, 2015. Release 16.2.

[6] F. Balduzzi, A. Bianchini, G. Ferrara, and L. Ferrari. Dimensionless numbers for the assessment of mesh and timestep requirements in CFD simulations of Darrieus wind turbines. *Energy*, 97:246–261, 2016.

[7] F. Balduzzi, A. Bianchini, R. Maleci, G. Ferrara, and L. Ferrari. Critical issues in the CFD simulation of Darrieus wind turbines. *Renewable Energy*, 85:419–435, 2016.

[8] T.S. Beddoes. A qualitative discussion of dynamic stall. *AGARD Special Course on Unsteady Aerodynamics, AGARD Report*, 679, 1979.

[9] A. Bianchini, G. Ferrara, L. Ferrari, and S. Magnani. An improved model for the performance estimation of an H-Darrieus wind turbine in skewed flow. *Wind Engineering*, 36(6):667–686, 2012.

[10] Alessandro Bianchini, Ennio Carnevale, and Lorenzo Ferrari. A model to account for the virtual camber effect in the performance prediction of an h-darrieus vawt using the momentum models. *Wind Engineering*, 35(4):465–482, 2011.

[11] M. Borg and M. Collu. A comparison between the dynamics of horizontal and vertical axis offshore floating wind turbines. *Philosophical Transactions of the Royal Society of London A: Mathematical, Physical and Engineering Sciences*, 373(2035):20140076, 2015.

[12] M. Borg and M. Collu. Frequency-domain characteristics of aerodynamic loads of offshore floating vertical axis wind turbines. *Applied Energy*, 155:629–636, 2015.

[13] M. Borg, M. Collu, and F.P. Brennan. Offshore floating vertical axis wind turbines: advantages, disadvantages, and dynamics modelling state of the art. In *The International Conference on Marine & Offshore Renewable Energy (MORE 2012)*, pages 26–27, 2012.

[14] M. Cahay, E. Luquiau, C. Smadja, F. Silvert, et al. Use of a vertical wind turbine in an offshore floating wind farm. In *Offshore technology conference*. Offshore Technology Conference, 2011.

[15] A.M. Chowdhury, H.I. Akimoto, and Y. Hara. Comparative CFD analysis of vertical axis wind turbine in upright and tilted configuration. *Renewable Energy*, 85:327–337, 2016.

[16] M. Collu, M. Borg, A. Shires, F.N. Rizzo, and E. Lupi. FloVAWT: Further progresses on the development of a coupled model of dynamics for floating offshore VAWTs. In *ASME 2014 33rd International Conference on Ocean, Offshore and*

Arctic Engineering, pages V09BT09A044–V09BT09A044. American Society of Mechanical Engineers, 2014.

[17] A.J. Coulling, A. J Goupee, A.N. Robertson, J.M. Jonkman, and H.J. Dagher. Validation of a FAST semi-submersible floating wind turbine numerical model with DeepCwind test data. *Journal of Renewable and Sustainable Energy*, 5(2):023116, 2013.

[18] L. Daróczy, G. Janiga, K. Petrasch, M. Webner, and D. Thévenin. Comparative analysis of turbulence models for the aerodynamic simulation of H-Darrieus rotors. *Energy*, 90:680–690, 2015.

[19] P. Delafin, T. Nishino, L. Wang, A. Kolios, and T. Bird. Comparison of RANS CFD and lower-order aerodynamic models for 3D vertical axis wind turbines. 2015.

[20] S. Ferreira, A. Van Zuijlen, H. Bijl, G. Van Bussel, and G. Van Kuik. Simulating dynamic stall in a two-dimensional vertical-axis wind turbine: verification and validation with particle image velocimetry data. *Wind Energy*, 13(1):1–17, 2010.

[21] A. Ho G. Corbetta and I. Pineda. Wind energy scenarios for 2030. Technical report, European Wind Energy Agency, 08 2015.

[22] M. Islam, D.S-K. Ting, and A. Fartaj. Aerodynamic models for Darrieus-type straight-bladed vertical axis wind turbines. *Renewable and Sustainable Energy Reviews*, 12(4):1087–1109, 2008.

[23] R. James and M. Costa Ros. Floating offshore wind: Market and technology review. Technical report, Carbon Trust, 06 2015.

[24] R. T. Jones and D. Cohen. Aerodynamics of wings at high speeds, aerodynamic components of aircraft at high speeds, high speed aerodynamics and jet propulsion. *Vol. VII, AF Donovan, HR Lawrence eds, Princeton University Press, Princeton, NJ*, 1957.

[25] Moti Keinan. A modified streamtube model for vertical axis wind turbines. *Wind Engineering*, 36(2):145–180, 2012.

[26] J.G. Leishman and T.S. Beddoes. A semi-empirical model for dynamic stall. *Journal of the American Helicopter society*, 34(3):3–17, 1989.

[27] T. Maître, E. Amet, and C. Pellone. Modeling of the flow in a Darrieus water turbine: Wall grid refinement analysis and comparison with experiments. *Renewable Energy*, 51:497–512, 2013.

[28] W.J. McCroskey. The phenomenon of dynamic stall. Technical report, DTIC Document, 1981.

[29] S. Mertens, G. van Kuik, and G. van Bussel. Performance of an H-Darrieus in the skewed flow on a roof. *Journal of Solar Energy Engineering*, 125(4):433–440, 2003.

[30] P.G. Migliore, W.P. Wolfe, and J.B. Fanucci. Flow curvature effects on Darrieus turbine blade aerodynamics. *Journal of Energy*, 4(2):49–55, 1980.

[31] A. Myhr, C. Bjerkseter, A. Ågotnes, and T.A. Nygaard. Levelised cost of energy for offshore floating wind turbines in a life cycle perspective. *Renewable Energy*, 66:714–728, 2014.

[32] A. Orlandi. CFD analysis of darrieus-type wind turbine in skewed flows. Master's thesis, Università di Pisa, Academic year 2013-2014.

[33] A. Orlandi, M. Collu, S. Zanforlin, and A. Shires. 3D URANS analysis of a vertical axis wind turbine in skewed flows. *Journal of Wind Engineering and Industrial Aerodynamics*, 147:77–84, 2015.

[34] A.N. Robertson, J. M Jonkman, A. J Goupee, A.J. Coulling, I. Prowell, J. Browning, M. D Masciola, and P. Molta. Summary of conclusions and recommendations drawn from the DeepCwind scaled floating offshore wind system test campaign. In *ASME 2013 32nd International Conference on Ocean, Offshore and Arctic*

Engineering, pages V008T09A053–V008T09A053. American Society of Mechanical Engineers, 2013.

[35] F. M. Yonesugi T. Wakui and R. Yokoyama. Performance analytical model of vertical axis wind turbines for floating offshore applications. In *EWEA 2015 conference*. EWEA, 2015.

[36] F.Z. Tai, K.W Kang, M.H Jang, Y.J Woo, and J.H. Lee. Study on the analysis method for the vertical-axis wind turbines having darrieus blades. *Renewable energy*, 54:26–31, 2013.

[37] G. Tescione, D. Ragni, C. He, S. Ferreira, and G.J. van Bussel. PIV-based analysis of 2D and 3D flow phenomena of vertical axis wind turbine aerodynamics. In *32nd ASME Wind Energy Symposium*, page 1080, 2014.

[38] A. Vernola. Analisi CFD degli effetti del moto ondoso sulle prestazioni di una turbina eolica ad asse verticale su piattaforma galleggiante. Master's thesis, Università di Pisa, Academic year 2014-2015.

[39] L. Vita. *Offshore floating vertical axis wind turbines with rotating platform*. PhD thesis, Danmarks Tekniske Universitet, 2011.